Table of Contents

1.0 Introduction

The Eos Simultaneity Study has been funded since June 1987 under grant NAGW-1101 from the University Applications Program at NASA Headquarters. Over the three years of this project, institutional participation in the project has included the University of Michigan, the Jet Propulsion Laboratory, George Washington University, the University of Nebraska, University of California at Davis, the University of Wisconsin, ERIM, NASA/AMES Research Center, Duke University and Aster Consulting; and subcontracts have generally been administered through the University of Michigan (with the exceptions of JPL and Duke). This executive summary is drawn from Technical Progress Reports provided by each institution in December 1989 which document accomplishments and plans for the remainder of the third year of funding and will also include results of a meeting of the investigator team held at the University of Michigan on February 14, 1990.

The study has yielded a number of technical results related both to the fundamental objectives of this program and to remote sensing science in general. For example, it has been found that while the signal from Eos SAR can be expected to be diurnally variant in response to changes in leaf-angle distribution and changes in canopy and substrate moisture condition, this variation is expected to be relatively continuous in the absence of certain impulses of a meteorologic (i.e., rain) or anthropogenic (i.e., harvest or tillage) nature. Consequently, no case can be made for simultaneous observation of vegetated terrain by Eos SAR and HIRIS. The requirements for specific relative offsets in the timing of SAR and HIRIS are driven by the extent to which the data from the two instrument packages can be analyzed synergistically to provide estimates of specific biophysical attributes. This issue cannot be fully addressed at this time since robust inversion approaches for either SAR or HIRIS have not been developed and tested to date. However, great progress has been made in development and validation of direct models to predict observed radar

backscatter and optical reflectance on the basis of biophysical attributes. Much of the work in this study to date has focused upon these models.

Finally, the experimental efforts of this study have significantly enhanced our capability to conduct field studies through improvement of procedures and techniques. Advances include new techniques for in situ observation of microwave dielectric properties and direct field comparisons of various methods for estimation of leaf area and the angular distributions of canopy elements.

This study has provided partial support to 16 faculty and primary researchers, 16 graduate students, 16 undergraduate students, and 9 members of administrative and technical support staffs. These efforts have resulted in 18 technical presentations at workshops and symposia and 10 technical publications.

The following sections present the technical progress reports for each of the participating institutions.

TECHNICAL PROGRESS REPORT

on

Eos Synergism Study

University of Michigan

M. Craig Dobson

January 1990

1.0 Objectives

The general objective of this study is to examine the relative timing requirements of the Eos SAR and HIRIS for observation of terrain and particularly vegetated terrain. To a large extent, this issue is determined by the time stability of the expected signal or, in other words, how quickly do backscatter (for SAR) and reflectance (for HIRIS) decorrelate in the absence of some impulse such as rain or harvest. If both signals (HIRIS and SAR) are expected to be time constant, then relative timing becomes a non-issue. On the other hand, if one or more of the signals is time variant and significant with respect to expected calibration, then what are the optimal observation times for retrieval of specific biophysical quantities and can SAR and HIRIS data be used synergistically in such retrievals.

Hence, a specific objective of this study is to define the temporal variance of σ^o and reflectance for natural vegetation canopies over the periods of minutes, hours and days. A second objective is to develop retrieval algorithms for SAR and HIRIS (individually and combined in a synergistic fashion). These algorithms are to be developed via first validating direct models of reflectance and backscatter, then conducting sensitivity studies of the validated models to specific biophysical variates, and finally inverting these models, as appropriate, for use in retrieval algorithms to be tested against data.

The specific objectives of the University of Michigan as part of the overall study have been to: (1) coordinate the activities of the various members of the investigator team, (2) generate experimental data sets to show the time variation of reflectance and backscatter from vegetation over the appropriate time scales using ground-based and airborne sensors, and (3) validate radar scattering models in conjunction with these data sets for use in sensitivity studies and development of retrieval algorithms applicable to Eos SAR and HIRIS.

2.0 Major Accomplishments

2.1 Specific Accomplishments

(1) Under a precursor to the existent program, a truck-based experiment was conducted in summer 1986 to examine the diurnal variation in σ^o and reflectance from a phototropic canopy (soybeans).

(2) An experiment was planned and successfully executed in summer 1987 at a Walnut orchard at the Kearney Agricultural Research Center using boom-mounted instrumentation to investigate the diurnal variation of σ^o and reflectance due to moisture related properties of the canopy.

(3) A radar scattering model, MIMICS, has been modified for the walnut orchard data and validated for that canopy at L-band.

(4) Initial sensitivity studies have been performed at L-band for various biophysical attributes of the walnut orchard.

(5) Preparations were made for an airborne experiment at the Duke University Research Forest in summer 1989. The field experiment was conducted (SAR only) and the field data has been partly processed and edited.

2.2 Detail Statement

The precursor experiment in 1986 involved participants from the University of Michigan, JPL (Paris, Cimino, Cook and Smith), NASA/Ames (Vanderbilt), and George Washington University (Lang). This experiment was the first attempt to obtain intensive simultaneous field observations with both radar scatterometers and visible/infrared radiometers, and established protocols for measurement strategy. Important issues defined by this experiment were (1) the need for

adequate time calibration of the sensors to account for thermal and solar conditions, (2) appropriate sampling strategies to account for both the temporal and spatial variation in canopy attributes as regards both the sensing systems and also the "ground truth" data, and (3) procedures for data acquisition and subsequent processing. Due to the problems encountered during the experiment (both procedural and related to intermittent cloud cover), the data and results were not suitable for publication. However, it was determined that changes in leaf-angle orientation are (1) very difficult to characterize with statistical satisfaction and (2) significant determinants of radar backscatter at higher frequencies (C- and X-bands). These results of this experiment contributed to a significantly improved experiment plan for the Kearney experiment in 1987.

An integrated field experiment was planned and conducted in summer 1987 at the walnut orchard and included numerous individuals from the University of Michigan, JPL, UC/Davis, NASA/Ames, George Washington University, and the University of Nebraska. The University of Michigan was primarily responsible for (1) overall experiment design, (2) acquisition of radar scatterometer data, (3) acquisition of moisture related ancillary data (i.e., soil and canopy gravimetric moisture, leaf water potential, and soil and canopy dielectric properties), and (4) editing and processing of these data. The experiment was quite successful and produced a very comprehensive data set summarized in Cimino, et al. (1988). This data was also presented at various workshops and symposia (Weber and Ustin (1988), Dobson, et al. (1988), Cimino, et al. (1988), Dobson (1988), and Ulaby, et al. (1988)).

Using the field data obtained at the walnut orchard (i.e., moisture related quantities obtained by the University of Michigan and canopy architectural quantities obtained by UC/Davis) the MIMICS model was modified and used to

successfully predict the observed variation of $\sigma^0_P(\theta)$ at L-band and also the diurnal variation of σ^0_P over a three-day period. The variations in the dielectric properties of the woody components of the trees and the soil substrate are found to account for the observed variation in σ^0 which ranged from 1 to 3 dB. These results have been presented at symposia McDonald, et al. (1989) and submitted for publication McDonald, et al. (1989) and Way, et al. (1990).

The validated MIMICS model has also been tested for other forest stands such as the frozen and thawed winter-time conditions for white spruce, black spruce, balsam poplar and alder. In general, excellent agreement is obtained with both the canopy propagation loss and backscatter derived from SAR observations at L-, C-, and X-bands. These results have been presented at symposia Dobson, et al. (1989) and Dobson, et al. (1990) and have also been submitted for publication Dobson, et al. (1990). Importantly, it was found that MIMICS-I (which assumes a continuous and closed canopy) cannot account properly for the observed σ^0 from sparse black spruce stands. As a consequence, MIMICS-II (for discontinuous tree canopies) has been developed and will be presented at IGARSS '90 (McDonald and Ulaby, 1990).

The highly encouraging MIMICS model validation results have given credence to preliminary model sensitivity studies of L-band backscatter response to variations in the dielectric constants of trunks, branches and the soil substrate. These results have been presented at IGARSS (McDonald, et al. 1988 and McDonald, et al. 89) and submitted for publication (McDonald, et al. 1990).

In an effort to extend the boom-mounted experimentation conducted at Kearney to a larger and more "natural" ecosystem, an airborne experiment was planned for loblolly pine stands at the Duke University Research Forest in summer

1989. This experiment was to involve truck-mounted scatterometry, ariborne SAR, AVIRIS and ASAS. Extensive preparatory work for the scatterometer was aborted by problems with the airborne SAR schedules and also strong theoretical indications that low altitude scatterometry (i.e., truck, platform, and helicopter mounted systems) were not suited to observing the net expected σ^0 (for a SAR). Although SAR observations in July 1989 were aborted, an extensive set of dielectric observations were made for loblolly pines and included sampling to identify (1) depth profile of trunk dielectric, (2) within-stand variance in ε^*, (3) between-stand variance in ε^*, (4) variation in ε^* of trunks as a function of vertical location, (5) diurnal variation of ε^*, and (6) seasonal variation of ε^*. In addition, detailed observations of moisture related quantities were made in association with airborne SAR data sets obtained at Duke at the end of August and beginning of September 1989. These data are presently being edited for use by MIMICS in prediction of the SAR response to selected test stands of variable age and density. Of note is that the diurnal variations of ε^* in the trunks of loblolly pines is not as strong as that found for the walnuts; and also that there is a variation in ε^* with vertical height up the trunk and this variation is not monotoric which indicates that two or more competing forces are controlling water distribution in the xylem.

3.0 Planned Activities

During the 1989-1990 time period the University of Michigan plans to conduct the following analyses:

(1) complete editing and processing of the dielectric data obtained at Duke in 1989,

(2) use the dielectric data in conjunction with stand architecture data obtained by Duke to initialize MIMICS for selected continuous stands of loblolly pine,

(3) test MIMICS-II for discontinuous stands of black spruce (from Alaska) and/or for stands of young loblolly pines (Duke) and compare to SAR and heloscat observations of σ^o, and

(4) conduct more thorough sensitivity analyses of σ^o, as predicted by MIMICS to (a) leaf angle orientation, (b) leaf moisture, (c) trunk and branch dielectrics, and (d) substrate conditions including moisture, roughness and the presence of intervening layers of snow and organic litter.

4.0 Personnel Supported

The following personnel have been supported by this project:

Name	Status	Responsibility
Fawwaz Ulaby	PI	overall direction of program
Craig Dobson	Co-I	direction of field measurements
Tom Senior	Faculty	advisor on certain aspects of model development
Jim Weber	Res. Scientist	canopy water relations meas.
Tom Haddock	Res. Scientist	scatterometter development & operation
Val Liepa	Faculty	scatterometer calibration
Kamal Sarabandi	Res. Scientist	Scatterometers and modeling
Kyle McDonald	GSRA	MIMICS and field experiments
Michael Whitt	GSRA	MIMICS and field experiments
M. Ali Tassoudji	GSRA	scatterometer support
Walid Ali Ahmad	GSRA	Radar calibration
Roger De Roo	GSRA	dielectric probe calibration
Ron Hatikka	Sr. Technician	scatterometer support
Parag Mody	Technician	scatterometer support
Jeanette Vechio	Secretary	secretarial support
Beth Olson	Secretary	secretarial support
Bonnie Kidd	Secretary	secretarial support
Timarie Wilkins	hourly	secretarial support
Martin Kuttner	hourly	technical lab support
Mike De Liso	hourly	technical lab support
Sebastian Lauer	hourly	lab and field support
Ron Oliver	hourly	lab support
Jorge Hernandez	hourly	lab support
Alan Klingelhafer	hourly	lab support
Roberto Mitrevski	hourly	lab support
Andrew Isztwan	hourly	lab support
Darelyn Crochran	hourly	lab support
G. Eleftheriades	GSRA	lab support

variously hourly help at Kearney Agricultural Res. Center

The following students have received degrees or are expected to do so over the next year with significant support from this program.

M. Ali Tassoudji -	Masters	June 1989
Kamal Sarabandi -	PhD	Sept. 1989
Kyle McDonald -	PhD	1991 expected
Michael Whitt -	PhD	1991 expected

5.0 Publications List

1. Cimino, JoBea, et al. "Eos Synergism Study: 1987 Field Experiment Data Report", JPL Tech. Rep. March 1988.
2. Cimino, J.B., C. Bruegge, D. Diner, J. Paris, C. Dobson, D. Gates, F. Ulaby, N. Goel, E. Kasischke, D. Kimes, r. Lang, J. NOrman, and V. Vanderbilt, "Synergism Requirements and Concepts for SAR and HIRIS on Eos," *International Geoscience and Remote Sensing Symposium* (IGARSS '87) *Digest,* Ann Arbor, Michigan, Vol. 2, pp. 955-966, May 18-21, 1987.
3. Cimino, J.B., J. Paris, M.C. Dobson, D. Gates, J.A. Weber, F.T. Ulaby, S.L. Ustin, V. Vanderbilt, J. Norman, R. Lang, and E. Kasischke, "Eos Synergism Study: Overview and Objectives," *International Geoscience and Remote Sensing Symposium* (IGARSS '88) Edinburgh, Scotland, September 1988.
4. Cimino, J.B., J. Paris, C. Dobson, F. Ulaby, J. Waber, V. Vanderbilt, S. Ustin, J. Norman, R. Lang, E. Kasischke, and Ray Hunt, "Synergism Study: Implications of Diurnal Change in Vegetation Canopies on Eos Orbit Selection," *1989 International Geoscience and Remote Sensing Symposium* (IGARSS '89), July 10-14, 1989, Vancouver, B.C., Canada.
5. Cimino, J.B., J. Paris, D. Casey, F. Ahern, N. Christensen, M.C. Dobson, F.T. Ulaby, J. Weber, R. Hoffer, M. Imhoff, E. Kasischke, A. Milne, J. Richards, A. Sieber, P. Churchill, D. Simonett, C. Slaughter, L. Viereck, E. Mougin, and T. LeToan, "The Effect of Changing Environmental Conditions on Microwave Signatures of Forest Ecosystems," submitted to *International Journal of Remote Sensing*, special issue on Microwave Signatures of Forests Workshops.
6. Dobson, M.C., F.T. Ulaby, and J. Paris, "Radar Backscatter from Tree Canopies", *Forest Signatures Workshop*, JPC, Ispra, Italy, September 1988.

7. Dobson, M.C., K. McDonald, F.T. Ulaby, and J.F. Paris, "Diurnal Patterns in Multifrequency, Multipolarization Backscattering by a Walnut Orchard," *International Geoscience and Remote Sensing Symposium* (IGARSS '88), Edinburgh, Scotland, September 1988.

8. Dobson, M.C., "Diurnal and Seasonal Variations in the Microwave Dielectric Constant of Selected Trees," *International Geoscience and Remote Sensing Symposium* (IGARSS '88). Edinburgh, Scotland, September, 1988 and in preparation for submission to *International Journal of Remote Sensing*.

9. Dobson, M.C. and E.S. Kasischke, "Microwave Attenuation by Boreal Forest Canopies in Winter," submitted to *1989 International Geoscience and Remote Sensing Symposium* (IGARSS '89), July 10-14, 1989, Vancouver, Canada.

10. Dobson, M., K. McDonald, F.T. Ulaby and J. Cimino, "Effects of Temperature on Radar Backscatter from Boreal Forests," IGARSS '90.

11. Dobson, M.C., K. McDonald, E. Kasischke, J. Way, and F.T. Ulaby, "Effects of Temperature on Microwave Attenuation and Backscatter from Boreal Forest Stands, to be submitted to *IEEE Trans. Geoscience and Remote Sensing 1990.*

12. McDonald, K., M.C. Dobson, and F.T. Ulaby, "Determination of Soil Moisture Beneath a Stalk or Trunk Dominated Canopy by Radar," I*nternational Geoscience and Remote Sensing Symposium* (IGARSS '88), Edinburgh, Scotland, September 1988.

13. McDonald, K.C., M.C. Dobson, and F.T. Ulaby, "Using MIMICS to Model Microwave Backscatter from Tree Canopies," *1989 International Geoscience and Remote Sensing Symposium* (IGARSS '89), July 10-14, 1989, Vancouver, B.C., Canada.

14. McDonald, K. and F.T. Ulaby, "MIMICS II: Radiative Transfer Modeling of Discontinuous Tree Canopies at Microwave Frequencies," IGARSS '90.

15. McDonald, K., M.C. Dobson, and F.T. Ulaby, "Using MIMICS to Model L-Band Multi-angle and Multi-temporal Backscatter from a Walnut Orchard," submitted to *IEEE Transactions on Geoscience and Remote Sensing*, November 1990.

16. Sieber, A.J., J.B. Cimino, R. Brown, J. Cihlar, C. Dobson, J. Ford, D. Gates, P. Hartl, G. Hildebrandt, R. Hoffer, M. Imhoff, E. Kasischke, J.P. Malingreau, J. Megier, T. Milne, J. Paris, J. Richards, F. Rocca, B. Rock, M. Sami, D. Simonett, T. LeToan, and F.T. Ulaby, "The Global Forest Ecosystem as Viewed by ERS-1, SIR-C and Eos," *International Geoscience and Remote Sensing Symposium* (IGARSS '87) Digest, Ann Arbor, Michigan, Vol. 2, pp. 967-974, May 18-21, 1987.

17. Tassoudji, A., K. Sarabandi, and F.T. Ulaby," Design Consideration and Implementation of the LCX Polarimetric Scatterometer (POLARSCAT), Radiation Laboratory Tech. Rep. 022486-T-A, EECS Dept., Univ. of Michigan, Ann Arbor, Michigan, June 1989.

18. Ustin, S.L., V.C. Vanderbilt, J. Way, F. Ulaby, C. Dobson, and D.M. Gates, "Opportunities for Eos Instrument Synergism in Monitoring of Forest Ecosystems," IGARSS '90 *Geoscience and Remote Sensing Symposium*, University of Maryland, College Park, Maryland, May 20-24, 1990.

19. Way, J., M. Schier, N. Christensen, C. Dobson, D. Gates, F. Ulaby, E. Kasischke, R. Lang, J. Norman, J. Paris, S.L. Ustin, V.C. Vanderbilt, and J. Weber, "Eos Synergism Study: Diurnal Change in Trees as Observed by Optical and Microwave Sensors," to be submitted to *Transactions Geoscience and Remote Sensing*, 1990.

20. Weber, J.A. and S.L. Ustin, "Water Relations of a Walnut Orchard: Simultaneous Measurements with Remote Sensing," IGARSS '88, Edinburgh, Scotland, September 13-16, 1988, ESA-SP284, Vol. III:1749-1752, 1988.

EFFECTS OF TEMPERATURE ON RADAR BACKSCATTER FROM BOREAL FORESTS

M.C. Dobson, K. McDonald, F.T. Ulaby and J. Cimino

Abstract:

An airborne SAR campaign during March 1988 acquired P-, L-, C- and X-band data for repeated overflights of the Bonanza Creek Experimental Forest located along the Ianana River near Fairbanks, Alaska. The experimental forest included many stands characteristic of the boreal forest of interior Alaska: white spruce (Picea glauca), black spruce (Picea mariana), and balsam poplar (Populus balsamifera). The airborne SAR data was complemented by extensive characterizations of forest stand parameters and microwave dielectric conditions. These scene properties are used as inputs to the Michigan Microwave Canopy Scattering (MIMICS) Model, which uses a first-order radiative transfer approach to predict radar backscatter as functions of the radar wave parameters of frequency, polarization and angle of incidence.

During the airborne campaign, an early spring thaw with air temperatures of 9°C was followed by more typic winter conditions with air temperatures of -15°C. SAR data were obtained for both the frozen and thawed conditions by the P-, L- and C-band polarimetric SAR operated by the Jet Propulsion Laboratory. These data sets are calibrated with respect to arrays of external calibration point targets. The image data is segmented by forest stand and the resultant average values of the radar backscattering coefficient are shown to compare favorably with the values predicted by MIMICS.

USING MIMICS TO MODEL MICROWAVE BACKSCATTER FROM TREE CANOPIES

K. C. McDonald, M. C. Dobson and F. T. Ulaby

The Radiation Laboratory
Department of Electrical Engineering and Computer Science
The University of Michigan
Ann Arbor, MI 48109-2122, U.S.A.
Phone: (313) 764-0500
FAX: 313/936-3492
Telex: 432-0815 UOFM-UI

ABSTRACT

The Michigan Microwave Canopy Scattering Model (MIMICS) is used to model microwave scatterometer data that were obtained during the August 1987 EOS Simultaneity Experiment. During this experiment, L-, C- and X-band truck-based scatterometers were used to measure radar backscatter from a walnut orchard in Fresno County, California. Multi-polarization data were recorded for orchard plots of varying irrigation levels.

MIMICS, a scattering model based on radiative transfer theory, is applied to model various data sets recorded during the experiment. Groundtruth data are used as inputs to MIMICS and the resulting modeled data are compared to the measured backscatter.

Data examined in this study include a series of diurnal measurments in which a single orchard plot was observed continuously over several 24 hour periods, a multi-angle data set for which this same plot was observed at varying incidence angles, and a series of data recorded on two plots of different irrigation levels.

In modeling the canopy backscatter, MIMICS accounts for scattering contributions directly from the trees themselves, direct backscatter contributions from the underlying ground surface, and contributions resulting from interactions between the trees and the ground. The model is shown to account for variations in canopy backscatter that are driven by diurnal processes as well as by the differing irrigation levels. The distribution of branch sizes and orientations within the tree crowns is shown to be an important parameter for modeling canopy backscatter.

MICROWAVE ATTENUATION BY BOREAL FOREST CANOPIES IN WINTER

M. C. Dobson
The Radiation Laboratory
Department of Electrical Engineering and Computer Science
The University of Michigan
Ann Arbor, MI 48109-2122
Telephone: (313) 764-0500
FAX: 313/936-3492
TELEX: 432-0815 UOFM-UI

E. S. Kasischke
Environmental Research Institute of Michigan
P.O. Box 8618
Ann Arbor, MI 48107
Telephone: (313) 994-1200
FAX: 313/994-0944
TELEX: 494-0991 ERIMARB

ABSTRACT

In March of 1988, a series of overflights were conducted by two airborne SARs over the Bonanza Creek Experimental Forest near Fairbanks, Alaska. The SARs included the Jet Propulsion Laboratory Airborne Imaging Polarimeter operating at P-, L-, and C-bands aboard a NASA/Ames DC-8 and the ERIM/Naval Air Development Center SAR operating at C- and X-bands aboard a NADC P-3. Although an early thaw had melted much of the water in the vegetation and produced wet surface conditions in the snow pack, the majority of the overflights occurred after an ensuing freeze.

The test site consisted of numerous stands of white spruce, black spruce, balsam poplar, and alder on islands along the Tanana River. A number of these stands were instrumented with arrays of corner reflectors (both trihedral and dihedral) and L-band active radar calibrators. The trihedrals ranged in size from 30 cm to 120 cm and were boresighted in the expected direction of the SARs. Each stand was carefully mapped with respect to tree type, location, diameter and height.

Statistics of the canopy derived from these measurements and allimetric relationships were input into the Michigan Microwave Canopy Scattering (MIMICS) Model along with pertinent dielectric information and used to estimate the two-way attenuation by the canopies. These estimates are found to compare favorably to remotely sensed estimates of the attenuation as determined by comparing the backscatter from the arrays of point targets to the backscatter from adjacent portions of each stand.

Technical Progress Report

Optical Model Application in Vegetation Remote Sensing

John M. Norman
Department of Soil Science
1525 Observatory Drive
University of Wisconsin
Madison, WI 53705

December 10, 1989

1) Objectives

This research activity has two objectives: 1) Comparison of predictions from the Cupid model with remotely-sensed observations from several vegetation canopies approximating full cover, and 2) inverting the Cupid model to estimate several canopy biophysical characteristics from the remote observations.

A major goal of the main proposal, which is entitled "Extended Ecosystem Signatures With Application to EOS Synergism Requirements", is to conduct field experiments to measure optical, radar and thermal signatures of forest, prairie and agricultural scenes. The work being done under this subcontract uses results from these field studies to test the model, Cupid. Inputs for Cupid would be provided by those directly involved in the field experiments. Predictions of the canopy bidirectional reflectance distribution functions (BRDF) from Cupid will be compared with BRDF measurements from the field experiments. If the model performs adequately, or can be made to perform adequately in the forward direction, then we intended to invert the model to produce estimates of canopy biophysical characteristics from the measured BRDF's or directional radiances. Although the major emphasis of this research is in the optical wavelength band, we had planned to coordinate our work with Fawwaz Ulaby and Roger Lang who are developing Radar models.

2) Major Accomplishments

2.1 Specific Accomplishments:

Field measurements of Walnut leaf reflectance and transmittance with the leaves attached to the trees and comparison with laboratory measurements on excised leaves.

Development of a stem water flow model for comparison with the stem dielectric constant measurements.

Inversion of fish-eye photographs taken by Susan Ustin to obtain leaf area index of the Walnut stand.

Modification of the Cupid model to include leaf angle distributions that are asymmetric about the azimuth.

Comparison of one-dimensional Cupid model predictions of nadir reflectance with nadir measurements made by Vern Vanderbilt.

2.2 Detailed Statement:

Leaf reflection and transmission measurements (400nm to 1000nm wavelength band) of Walnut leaves at various locations in the canopy were made in the morning and afternoon to determine whether the laboratory measurements made on excised tissue were representative, and to determine whether the leaf properties varied during the day. The insitu field measurements and lab measurements of spectral properties were comparable in the 400 to 1000 nm wavelength band considering typical spatial variability and effects of age and dust. Therefore the lab measurements were considered reasonable in the 1000nm to 2400 nm wavelength band because the insitu measurements did not cover this wavelength band. The Spectron SE-590 failed at midday so the afternoon measurements that were taken were useless. The following table is a summary of our best estimate of the Walnut leaf spectral properties for old and young leaves in the 100% and 33% ET treatments including sun and shade leaves.

TABLE 1. Walnut leaf reflectance and transmittance from 1987 measurements at the end of the field experiment. The treatment includes leaf age (current year=new, other=old), irrigation treatment (100% or 33%), and location of leaf (upper leaf in the sun=sun, lower shaded leaf=shade).

Treatment	MMR Chanel						
	1	2	3	4	5	6	7
Reflectance of top of leaf							
New,100%,Sun	6	12	7	43	43	35	24
Old,100%,Sun	7	11	8	51	51	41	28
33%,Sun	8	15	11	48	48	39	26
Old,100%,Shaded	7	11	9	44	44	36	24
Reflectance of bottom of leaf							
New,100%,Sun	9	18	12	43	43	35	23
Old,100%,Sun	9	18	13	50	50	41	28
33%,Sun	11	20	15	48	48	39	26
Old,100%,Shaded	9	16	16	45	45	36	25
Transmittance of leaf							
New,100%,Sun	3	13	7	47	47	38	26
Old,100%,Sun	1	3	2	33	33	26	18
33%,Sun	1	6	4	35	35	28	19
Old,100%,Shaded	1	6	3	40	40	32	22

The Walnut stem dielectric measurements indicated a large change in xylem water content over a diurnal cycle of transpiration. A simple stem water conduction model was constructed to accommodate both radial and longitudinal movement of water as a function of transpiration rate. Work on this model was stopped when Ray Hunt began work on the project with JoBea Cimino because he had considerably more expertise in this area and apparently was going to do that modeling.

Estimating the leaf-area-index (LAI) of the Walnut orchard is very difficult so we analyzed several fish-eye photographs that had been taken by Susan Ustin to obtain an indirect estimate of LAI. The average LAI from six fish-eye photographs was 2.0. David Goldhammer also made gap-fraction measurements at solar noon in 1987 using a large gridded canvas, and our estimate of LAI from his measurements is 2.6. These values are much lower than the LAI measurements obtained from directly sampling trees; direct sampling yielded LAI=3.7. The reason for this difference may be associated with the clumping of vegetation on branches and trees.

The Cupid BRDF model was originally limited to canopies with leaf azimuth angle distributions that were symmetric about the points of the compass. We have modified Cupid to include azimuthally asymmetric leaf azimuth angle distributions. The BRDF for a canopy can be quite sensitive to whether the leaf azimuth angle distribution is symmetric. The Walnut orchard appears to be reasonably symmetric about the azimuth from canopy structure measurements so this refinement may only provide a small improvement in model predictions.

The main objective of this research has been to compare predictions of canopy BRDF with measurements from the Walnut orchard experiment. Unfortunately only one nadir set of data has been made available so that is the only comparison work that we have done. The one set of nadir-view MMR measurement results that have been provided to us are for a single observation time between 1500 and 1530 Pacific Daylight Time on August 24, 1987. This data is from the 100% plot and consists of the average of 720 measurements in seven wavelength bands. These results are compared with predictions of the one-dimensional Cupid model (Norman et al. 1985) for leaf-area-indices of 2.0 and 3.7 using measured leaf spectral properties and estimated soil reflectances (Table 2). Leaf spectral properties varied with age and height and average properties were used in the model. The fraction of incident radiation above the canopy that is in direct beam is also required as an input for Cupid. Unfortunately this is very difficult to measure in each MMR wavelength band and so was not available in the data set. A detailed study at Nebraska in 1982 provided estimates of direct-beam fractions in the seven MMR wavelength bands for clear skies over a range of solar zenith angles. These values should be appropriate for clear skies at Fresno, California and are tabulated in Table 2.

TABLE 2. Average measured leaf reflectance and transmittance for seven MMR wavelength bands on Walnut leaves and estimated dry soil reflectances. Beam fractions of incident radiation were estimated from clear sky observations made in Nebraska in 1982 and should be appropriate for clear skies in California at similar zenith angles.

	MMR Wavelength Bands						
	1	2	3	4	5	6	7
Leaf Reflectance	6.5	11.0	7.0	45.0	42.5	34.5	22.0
Leaf Transmittance	2.5	10.0	5.0	42.0	41.5	32.5	22.5
Soil Reflectance	5.0	6.0	8.0	14.0	21.0	21.0	13.0
Beam Fraction	0.80	0.86	0.89	0.91	0.93	0.95	0.97

The results of the comparison of nadir measurements with predictions from the Cupid model are summarized in Table 3. Most of the model results fall within the range of the measured mean plus or minus one standard error. This is surprisingly close agreement between a one-dimensional model and measurements over an orchard that has distinct rows. The effect of the LAI uncertainty is minor because at an LAI of 2.0 only a small amount of soil is apparent anyway.

TABLE 3. Comparison of nadir measurements of canopy bidirectional reflectance with predictions from the one-dimensional model, Cupid, in seven MMR wavelength bands on the 100% Evapotranspiration treatment in a Walnut orchard (Caldwell and Vanderbilt, 1989).

	MMR Wavelength Band						
	1	2	3	4	5	6	7
Measurements	2.8	4.5	4.0	25.8	26.1	15.0	6.6
(std. error)	(0.9)	(1.4)	(1.3)	(9.0)	(8.0)	(4.6)	(2.1)
Cupid Model							
LAI=2.0	2.2	3.8	2.6	23.1	23.5	16.6	8.7
LAI=3.7	2.0	3.8	2.3	27.1	25.6	16/8	8.5

References:

Caldwell, W. and V.C. Vanderbilt. 1989. Tree canopy radiance measurement system. Optical Engineering 28:1227-1236.

Norman, J.M., J.M. Welles, and E.A. Walter-Shea. 1985. Contrasts among bidirectional reflectance of leaves, canopies and soils. IEEE Trans. Geoscience and Remote Sensing GE-23:659-667.

3) Planned Activities

The primary activity for the upcoming year of research will be to compare the Cupid model predictions of BRDF with measurements from the Walnut orchard. This cannot be done until some measurement results are available. At the present time the model appears to be working adequately for nadir predictions but we have no indication about off-nadir comparisons. Originally we had planned to invert the Cupid model using measured BRDF data as another part of the research through cooperation with Dr. Naren Goel of New York. However because of problems in the contract office at NASA this work was only funded the first year. In the second year we lost the funds to do this work because of some technicality in NASA. It has never been clear why we had no problem the first year and then lost the funds the second year. Therefore we are not able to do any inversion work on Cupid.

The second activity is to continue to work with Susan Ustin to characterize the canopy of the Walnut orchard. We plan to modify a program that will estimate leaf area density and leaf angle distribution for a heterogeneous canopy using a three-dimensional kernal. The input for this work will be digitized fish-eye photographs from the Walnut orchard.

4) Personnel Supported

Wayne Polley (Univ. of Nebraska)- Partial support from this grant to develop the stem flow model and process the leaf reflectance and transmittance data for Walnut leaves.

Naren Goel (SUNY-Binghamton)- Consultant the first year to assist in the inversion of optical models such as Cupid and begin work on the joint inversion of RADAR and optical models. He participated in three meetings of the research group and demonstrated that the Cupid model is invertible.

Jia-Lin Chen (Univ. of Wisconsin)- Assisted in the adaptation of the Cupid model to run on the Unix computer at the University of Wisconsin (Cupid was originally written on an IBM computer) and modified the Cupid model to accommodate azimuthally asymmetric leaf angle distributions.

5) Publications

Martens, S.N., S.L. Ustin and J.M. Norman. 1990. Measurement of tree canopy architecture. Submitted to International J. of Remote Sensing.

Ustin, S.L., S.N. Martens, J.M. Norman and D. Goldhammer. 1988. Measurement and characterization of tree canopy architecture. IGARSS. Edinburgh, Scotland. Sept. 13-16, 1988. ESA,SP-284. Vol. 3 p.1753. Abstract.

Cimino, J., J.Paris, M.C.Dobson, D.Gates, J.A.Weber, F.T.Ulaby, S.L.Ustin, V. Vanderbilt, J.Norman, R.Lang and E.Kasischke.1988. Eos synergism study: Overview and objectives. Abstract.

Cimino, J., J.Paris, M.C.Dobson, F.T.Ulaby, J.A.Weber, V.Vanderbilt, S.L.Ustin, J.M.Norman, R.Lang, E.Kasischke and R.Hunt. 1989. Synergism study: Implication of diurnal change in vegetation canopies on Eos orbit selection. IGARSS. Vancouver, B.C., Canada. July 1989. Abstract.

UNIVERSITY OF CALIFORNIA, DAVIS

BERKELEY • DAVIS • IRVINE • LOS ANGELES • RIVERSIDE • SAN DIEGO • SAN FRANCISCO • SANTA BARBARA • SANTA CRUZ

DEPARTMENT OF BOTANY
(916) 752-0617
FAX: (916) 752-4754

DAVIS, CALIFORNIA 95616

December 4, 1989

Dr. Fawwaz T. Ulaby
Professor and Director
Center for Space Terahertz Technology
College of Engineering
University of Michigan
3228 EECS Building
Ann Arbor, MI 48109-2122

Dear Dr. Ulaby:

Please accept the technical progress report you requested for our NASA subgrant under the "Extended Ecosystem Signatures with Application to Eos Synergism Requirements" program. Funding for the research effort under this program has been subsidized from other research grants to Dr. Vanderbilt and myself. Analysis to date of the MMR data has required about 8 person-months, analysis of the canopy geometry data and associated programming has required about 24 person-months, about 3 person-months to design and build the optical measurement system, about 2.5 person-months of contract administration (including field station reports to the Kearney Agricultural Center), about 12 person-months for the Kearney field experiment (including subsequent data collection), about 1 person-month for the Duke and Shasta field experiments, and about 6 person-months in manuscript preparation and abstract/presentation preparation for scientific meetings. We anticipate about 3 more months of work are necessary to analyze the MMR data and about 1-2 more months to complete the canopy analyses. We do not know how much time will be required to properly analyze the AVIRIS data since it is a relatively new instrument and we will be using new software and new computers for the analyses. Due to the large number of spectral bands the time to fully explore the data could easily exceed the entire budget for this grant. We plan to minimize the time by restricting our approach to a comparison among coregistered scenes having the same solar angles. We will provide some further exploration of the data structure but most of this work will be postponed until FY90-91 funding is available.

If you need further clarification of the status of work performed under this grant, please do not hesitate to contact me.

Sincerely,

Susan Ustin

Susan L. Ustin
Research Botanist

RE: Program objectives and review for U. Michigan subcontract # 204272, "Measurement and modeling of canopy geometry for remote sensing applications," under NASA grant NAGW-1101, "Extended ecosystem signatures with application to Eos Synergism Requirements."

Susan L. Ustin, Principal Investigator and Vern C. Vanderbilt, CO-Principal Investigator.

1. Objectives. The objective of this subgrant has been to participate in field experiments that measure, test, and validate remotely sensed optical models for the detection of canopy structure and water relations. To date, the emphasis has been on developing an efficient strategy and appropriate techniques for the measurement of forest vegetation data and of optical datasets. These data will be used in optical and microwave inversion models and in field experiments. The focus of current FY 89-90 emphasis is to (1) complete analyses on the orchard experiment and to (2) test the optical models in a forest environment using an aircraft data set and to (3) collaborate with the microwave modelers in the project, in the development of joint algorithms for the extraction of vegetation biophysical characteristics.

These research objectives provide two key elements that are necessary to the overall goals of the Eos Simultaneity project: First, provide the canopy architectural and water relations information for testing the predictions of optical and microwave inversion algorithms. Second, provide analysis of the optical data sets from the walnut orchard experiment and the Shasta experiment. The results of these data analyses will be used in collaboration with other PI's to develop joint optical-microwave inversion algorithms.

2. Major Accomplishments.

2.1. Specific Accomplishments.

1. Participated in the design of, and collection of, field datasets for describing canopy architecture and water relations for the walnut experiment. Provided the student crew for the experiment.

2. Designed and built a device for making the optical measurements for the walnut experiment. Participated in the collection of the optical datasets of the walnut experiment and provided 14 student assistants who participated in the field data collection.

3. Provided data entry, quality control checking, and statistical data analysis for all canopy geometry and optical datasets from the walnut experiment.

4. Published one paper on the sampling design and canopy

radiance measurement system, one paper on the canopy water relations, and have submitted one paper for publication describing the canopy geometric properties from the walnut experiment (included in the appendix).

5. Acquired field spectra of loblolly pine branches as part of the Duke Forest Experiment.

6. Acquired fish-eye photos of Mt. Shasta study sites as part of the characterization of the stand structure. Acquired field water relations, Regan radiometer and reflectance calibration data at Mt. Shasta as part of the AVIRIS water relations experiment.

7. Acquired dataset to compare the use of four commercially available optical sensors for indirectly measuring leaf area index and mean leaf angle distributions from the walnut orchard and from a Ponderosa pine forest.

2.2 Detail Statement. The first three publications from this research are included in the appendix, "Canopy radiance measurement system," by W. Caldwell and V.C. Vanderbilt (Opt. Eng. 28: 1227-1236), and "Measurement and modeling of tree canopy architecture," by S.N. Martens, S.L. Ustin, and J.M. Norman (submitted, Int. J. Remote Sens.), and "Water relations of a walnut orchard: Simultaneous measurement with remote sensing," by J.A. Weber and S.L. Ustin (IGARSS '88, ESA SP-284 Vol. 3: 1749-1751). These three papers, and related abstracts describe the methods of measurement used to describe the optical, geometric, and water relations properties of the walnut orchard. The design and measurement of the orchard was complex due to the fact that the row structure produced a highly non-random periodicity in the datasets. Water relations properties change diurnally and spatially vary with canopy position and sun angle. Adequate statistical sampling of the orchard required obtaining relatively large datasets for these variables, which were acquired over the two-week experiment, and which have since required significant amounts of time to quality-control check all data. Most of the time spent so far has been in validating the data quality, but which now has been completed. More synthetic analyses of the results are presently underway.

We began work on the second field experiment last summer. We obtained field reflectance spectra of foliage of loblolly pine by needle age-class and by stand age at the Duke forest. These data will provide a description of the variation in optical spectral signatures as a function of foliage age and stand age (an indirect measure of soil nutrient status). This work is part of a broader investigation of environmental factors controlling spectral signature components in conifer foliage. Initially, this data was to have been used in connection with analysis of AVIRIS data from the site, however, due to technical problems with the aircraft instrument, the AVIRIS data was not obtained at the Duke forest. Eight flightlines of AVIRIS data were acquired at Shasta, CA during September, 1989. We designed the flight so that we could examine

whether diurnal changes in reflectance could be attributed to changes in canopy water status. We obtained field calibration spectra, regan radiometer data, and foliage water potential data at one of the Shasta sites, to be used for calibrating and analyzing AVIRIS data.

3. Planned Activities.

1. We plan to complete the statistical analysis of the optical datasets from the walnut experiment during this budget period. This will include analysis of the spectral signatures of walnut leaves and correlation with leaf biochemistry, and analysis of the canopy reflectance properties as a function of position and time of day. These data will be compared with the results of the geometry study for examining and validating optical inversion models.

2. We will determine the vertical distribution of canopy geometry (branch size class distributions, foliage and fruit distributions as a function of height) for 2 class (trunk, canopy) and 3 class (trunk, low and high canopy) groupings. We will determine the probability density distribution function for the vertical classes.

3. We will complete analysis and submit for publication, our comparison of different methods for indirectly sampling canopy geometric properties. Most of the data analysis has been completed, with the exception of running a 3-d canopy inversion model on the datasets. We have implemented an analysis program for analyzing the data to calculate leaf area index and mean tip angle distribution, assuming a 1-d model. We plan to implement Wells and Norman's 3-d model on the computer system this winter.

4. We will obtain AVIRIS data and initiate analyses of the Shasta dataset this year. We have initiated a collaboration with Dr. Youguan Kou (Environmental Systems Research Institute) who will be coregistering the AVIRIS flightlines and will digitize a topographic map of the Shasta study site. We will analyze the AVIRIS datasets for diurnal patterns associated with alterations in the water status of the forest canopy. Field datasets to be used for validation and calibration have been analyzed.

4. Personnel Supported. The following personnel were supported by this project. Scott Martens will receive his Ph.D. in Dec. 1989.

Name	Status	Project Responsibility
Principal support:		
Susan Ustin	PI	canopy measurements, leaf spectra, AVIRIS data analysis, administration of grant

Vern Vanderbilt	PI	MMR measurements and analysis, AVIRIS data analysis
Rita Pettigrew	assistant	MMR data analysis
Scott Martens	Ph.D. Student expected degree 12/89	canopy data analyses
Robert Rousseau	assistant	canopy data analyses, AVIRIS data analysis
Guy Cook	assistant	microwave data analysis

Short-term support:

Walnut field experiment:

Kevin Berger	undergrad	MMR measurements
Jenny Clark	undergrad	MMR measurements
William Caldwell	undergrad	MMR measurements
Peter Collins	undergrad	canopy measurements
Aram Derowetski	grad	canopy measurements
Carol Hotton	grad	canopy measurements
Paul Rich	post-doc	canopy analysis software
Doug Ryden	assistant	microwave data analysis
Ken Severin	grad	canopy measurements
John Shin	undergrad	canopy measurements
Jatinder Singh	undergrad	canopy measurements
Curtis Smith	undergrad	canopy measurements; data entry
Erik Ustin	undergrad	canopy measurements
Jerome Ward	post-doc	fish-eye photo analysis
Monica Wiley	undergrad	water relations
Nicole Wiley	undergrad	water relations

Collaboration (without support):

Dr. Brian Curtiss U. Colorado	spectral signatures of conifer foliage
Dr. Barry Ganipole U. Arizona	MMR data and canopy analysis
Dr. Youguan Kou Environmental Systems Research Institute	GIS database

5. Publications.

The following publications and abstracts have resulted from the research funded under this program. We anticipate several additional publications from this work during the FY-89-90 year that provide additional analyses of the canopy architecture and reflectance properties from the walnut experiment.

PUBLISHED PAPERS AND MANUSCRIPTS

1990 Martens, S.N., S.L. Ustin, and J.M. Norman. Measurement and characterization of tree canopy architecture. (submitted, Int. J. Remote sens.)

1990 J. Way, M. Schier, N. Christensen, C. Dobson, D. Gates, F. Ulaby, E. Kasischke, R. Lang, J. Norman, J. Paris, S.L. Ustin, V.C. Vanderbilt, and J. Weber. Eos Synergism Study: Diurnal Change in trees as observed by optical and microwave sensors. (to be submitted to Trans. Geosci. and Remote Sens.).

1989 William Caldwell and V.C. Vanderbilt. Canopy radiance measurement system. Opt. Eng. 28: 1227-1236.

1989 Curtiss, B. and S.L. Ustin. The remote detection of early stages of air pollution injury in coniferous forests using imaging spectrometer. Int. J. Remote Sensing (in press).

1988 Weber, J.A., and S.L. Ustin. Water relations of a walnut orchard: Simultaneous measurement with remote sensing. IGARSS '88, Edinburgh, Scotland, UK, Sept. 13-16, 1988. ESA-SP284 Vol. III: 1749-1752.

PAPERS PRESENTED AT SCIENTIFIC MEETINGS

1990 Ustin, S.L., V.C. Vanderbilt, J. Way, F. Ulaby, C. Dobson, and D.M. Gates. IGARSS '90. Opportunities for Eos instrument synergism in monitoring of forest ecosystems. Geosci. and Remote Sens. Symp. University of Maryland, College Park, MD May 20-24, 1990.

1989 Cimino, J., J. Paris, C. Dobson, F. Ulaby, J. Weber, V. Vanderbilt, S. Ustin, J. Norman, R. Lang, E. Kasischke, and R. Hunt. Synergism Study: Implication of diurnal change in vegetation canopies on Eos orbit selection. IGARSS '89 Geosci. and Remote Sens. Symp. Vancouver, B.C. July, 1989.

1989 Ustin, S.L. and S.N. Martens. Measurement and characterization of tree canopy architecture. Ecol. Soc. Am. 74th Ann. Meeting, Toronto, Canada. August 6-10, 1989. Bull. Ecol Soc. 70: 285.

1988 Ustin, S.L., S. Martens, J. Norman, and D. Goldhamer. Measurement and characterization of tree canopy architecture. IGARSS '88, Edinburgh, Scotland, UK, Sept. 13-16, 1988. ESA SP-284, Vol. 3: 1753.

1988 Weber, J.A., and S.L. Ustin. Water relations of a walnut

orchard: Simultaneous measurement with remote sensing. IGARSS '88, Edinburgh, Scotland, UK, Sept. 13-16, 1988. ESA SP-284, Vol. 3: 1749-1752.

1988 W. Caldwell and V.C. Vanderbilt. Field system to determine reflectance of tree canopies. IGARSS '88, Edinburgh, Scotland, UK, Sept. 13-16, 1988. ESA SP-284, Vol. 3: 1756.

1988 Cimino, J., J. Paris, M.C. Dobson, D. Gates, J.A. Weber, F.T. Ulaby, S.L. Ustin, V. Vanderbilt, J. Norman, R. Lang, and E. Kasischke. Eos Synergism Study: Overview and Objectives. IGARSS '88, Edinburgh, Scotland, UK, Sept. 13-16, 1988.

1988 Curtiss, B. and S.L. Ustin. The remote detection of early stages of air pollution injury in coniferous forests using imaging spectrometry. Proc. European Joint Research Center Remote Sensing of Forests Workshop. Ispara, Italy, Sept. 4-6, 1988.

November 1989
Volume 28 Number 11
ISSN 0091-3286

The International Society for Optical Engineering

Optical Engineering

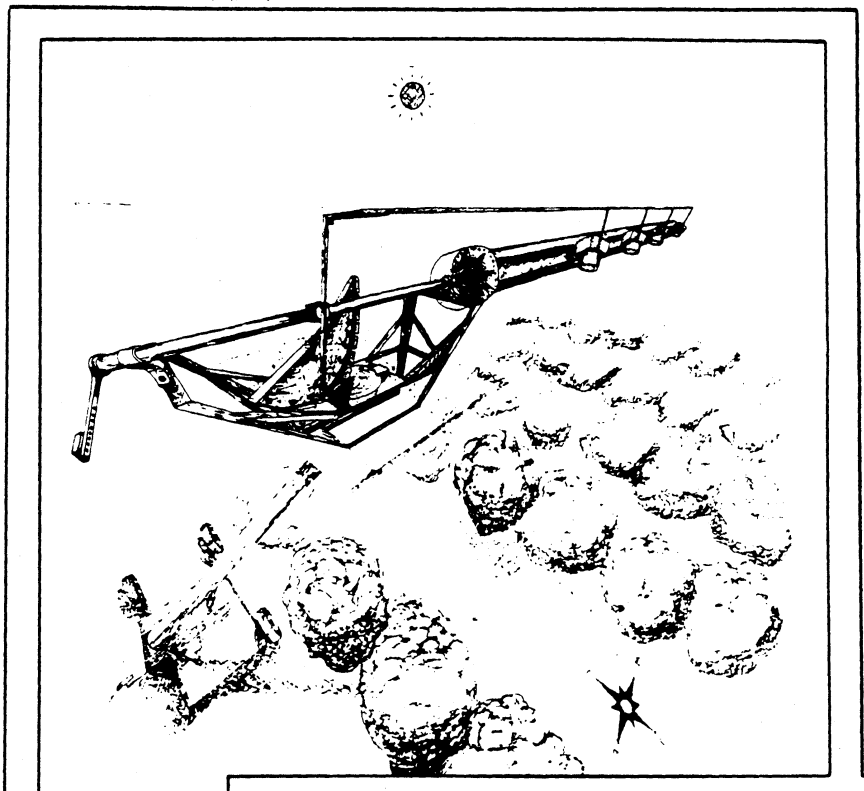

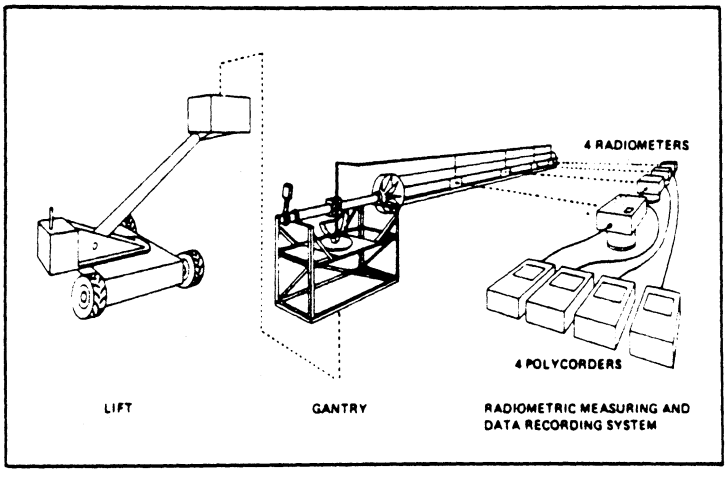

Point Sources
Infrared Focal Plane Arrays
Holographic Optical Elements
Gradient Index Lenses
Optical Design
Optical Buses
Fiber Optics
Pattern Synthesis
Moire
Target Acquisition
Radiance
Point Spread Function
Interferometric Tomography
Helmet-Mounted Displays

SPIE Reports — Book Reviews
Short Courses — Meetings

'ree canopy radiance measurement system

illiam Caldwell
ASA Ames Research Center
echanical Systems and Controls Branch
S 213-4
offett Field, California 94035-4000

C. Vanderbilt, MEMBER SPIE
iS Technology, Inc.
S 242-4
offett Field, California 94035-4000

Abstract. A system is described for obtaining both an estimate of the spatial mean bidirectional reflectance factor (BRF) for a tree canopy (displaying a horizontally heterogeneous foliage distribution) and the statistical significance of that estimate. The system includes a manlift supporting a horizontal beam 7 m long on which are mounted four radiometers. These radiometers may be pointed, and radiance data acquired, in any of 11 view directions in the principal plane of the sun. A total of 80 data points, acquired in 3 min, were used to estimate the BRF of a walnut orchard 5 m tall and detect true differences of 12% of the mean approximately 90% of the time.

Subject terms: radiance; bidirectional reflectance factor; bidirectional reflectance distribution function; tree canopy.

Optical Engineering 28(11), 1227-1236 (November 1989).

NTENTS

TRODUCTION

tree canopy, as for any other plant canopy, determining the bidirectional reflectance factor (BRF) from field measurements is a sampling problem. It requires estimation of the statistics of the signal: a radiance L(i;r,x,y) that varies as a function of both horizontal (x,y) location and sun and view (i;r) directions.[1]

In remote sensing and plant sciences, such reflectance data are needed for developing and testing mathematical models of the radiation regime in plant canopies.[2] These models are used in parameter studies to gain understanding of remotely sensed images from satellite sensors and thereby to address the more detailed problems of discriminating species of plants, determining their areal extent, and assessing their morphological and physiological condition. Such information will support future efforts in earth system science.[3,4]

Part of the variability in a set of radiance data of a plant canopy depends on the horizontal (x,y) location at which each measurement was made. The variability provides an indication of how representative the measured portions of the canopy might be, compared to the entire canopy if it were measured.

The spatial variability of the radiance decreases as the field radiometric instrument [having generally a field of view (FOV) of 10° or 15°] is elevated higher above the canopy. This is because the size of the instrument's "footprint" on the canopy (the area of the canopy within the FOV of the instrument) increases with instrument altitude, thereby including at higher altitudes a sample more representative of the entire canopy.[1] In practice, the reduction in the variability of the data that comes with increasing the instrument altitude is limited, since cost and other factors constrain the maximum height of the ground-based platform supporting the instrument. Comparison of radiance data acquired using a satellite sensor and a field radiometric instrument requires consideration of their differing fields of view: fractions of a milliradian for the instantaneous FOV of a

:659 received Dec. 13, 1988; revised manuscript received May 30, 1989; d for publication May 30, 1989.
) Society of Photo-Opucal Instrumentation Engineers.

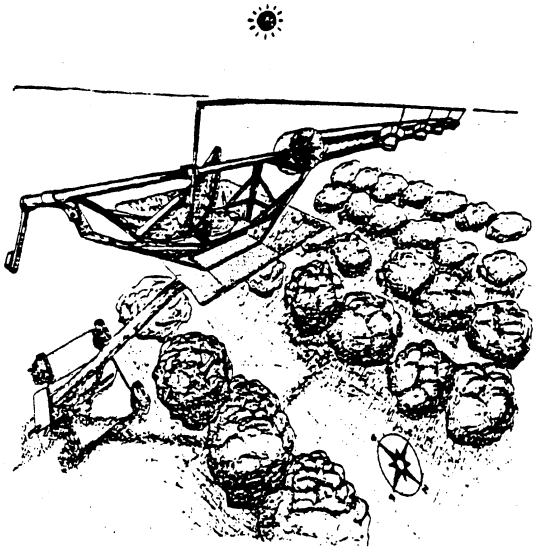

Fig. 1. Operator's view of the tree canopy radiance measurement system above the walnut orchard.

satellite sensor compared with as much as 20° for a ground-based sensor.

The second source of radiance variability, sun and view directions, is canopy dependent.[5–11] For many canopies (those both horizontally and azimuthally isotropic, for example), measurements indicate that both the "hot spot" and the "cold spot" (local maximum and minimum, respectively, in the BRF[12,13] are found in the principal plane.[5–11] The principal plane is defined by the two vectors describing the sun direction and earth vertical.

Our main goal was to construct an apparatus to provide the capability to sample the radiance and determine the mean BRF of a tree canopy measured in essentially one sun direction and one view direction (i;r).

We deemed the achievement of this goal a potentially daunting task because the tree canopy to be measured, a walnut orchard, displays significant horizontal morphologic variability. Trees approximately 5 m tall are planted in a rectangular pattern, 3.4 m × 6.7 m, which forms rows of foliage separating parallel strips of bare soil. Because the radiance variation was a function of horizontal location, use of the innovative PARABOLA instrument, a radiometer quite cleverly designed for rapidly acquiring data as a function of view direction, was not considered.[6]

This paper describes the apparatus, the tree canopy radiance measurement system, and provides an analysis of data collected using the system.

2. TREE CANOPY RADIANCE MEASUREMENT SYSTEM

2.1. Design objectives

The rationale for design of the tree canopy radiance measurement system was to provide the capability to determine the mean BRF of tree canopies measured in as many as 11 view directions in the principal plane of the sun. Data were to be acquired at various times during a day. We had the following specific objectives:

(1) The measured reflectance values should be obtained by a method that is directly comparable with established field measurement procedures.[14] Data values obtained with the method should be directly comparable with published data sets for other plant canopies.

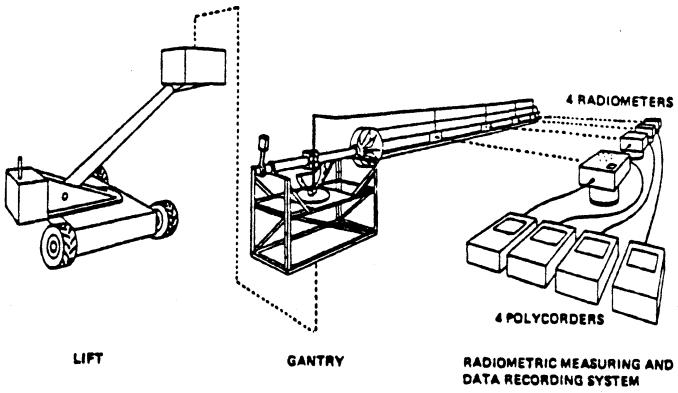

Fig. 2. Tree canopy radiance measurement system.

(2) The reflected flux should be estimated in the wavelength bands of the Thematic Mapper sensor on the Landsat series of satellites. Because several Barnes Engineering MMR model 12-1000 radiometers[15] were available, this was the model that was used for these measurements. This model has an FOV of 15°.

(3) The design should allow a data acquisition sequence, repeated at intervals of approximately 0.5 h, that includes measurements of the canopy viewed in the principal plane at zenith angles of 0°, ± 15°, ± 30°, ± 45°, ± 60°, and ± 75°. The design should allow the sky radiance field to be measured in 41 directions, the same positive zenith view angles (as used for downward viewing) at azimuth angles forming the eight points of the compass.

(4) The mean BRF of the tree canopy should be estimated within a period of approximately 3 min at the $\alpha = 0.05$ level of statistical significance.

2.2. Description of tree canopy radiance measurement system

The tree canopy radiance measurement system (Figs. 1 to 5) consists of three parts: the radiometric measuring and data recording system, the manlift, and the gantry. The system for measuring and recording the radiometric data (Fig. 2) includes four Barnes MMR radiometers, each capable of measuring the canopy radiance in seven wavelength bands (Table I). Paired with each radiometer is an Omnidata Polycorder (Omnidata Inc., Logan, Utah) for digitizing and recording the data and later transferring those data directly to a computer.

The manlift (approximately equivalent to model MZ46A, Grove Manufacturing, Shady Grove, Pa.), a mobile aerial platform, has a maximum vertical platform height of 12 m, a maximum horizontal reach of 9.8 m, and a maximum platform load carrying capacity of 340 kg. When radiance data were acquired, the manlift was operated from the basket and driven back and forth along a road 25 m long.

The gantry (Fig. 3) mounts to and extends 7 m horizontally from the basket of the manlift. The gantry is designed to support both the radiometers and a motor-driven camera and to facilitate their rotation to coincident zenith and azimuth view directions. It includes a horizontal cantilever beam and support frame. Also on the gantry are the control lever (Fig. 4) and sundial (Fig. 5), both used to adjust the view direction of the radiometers.

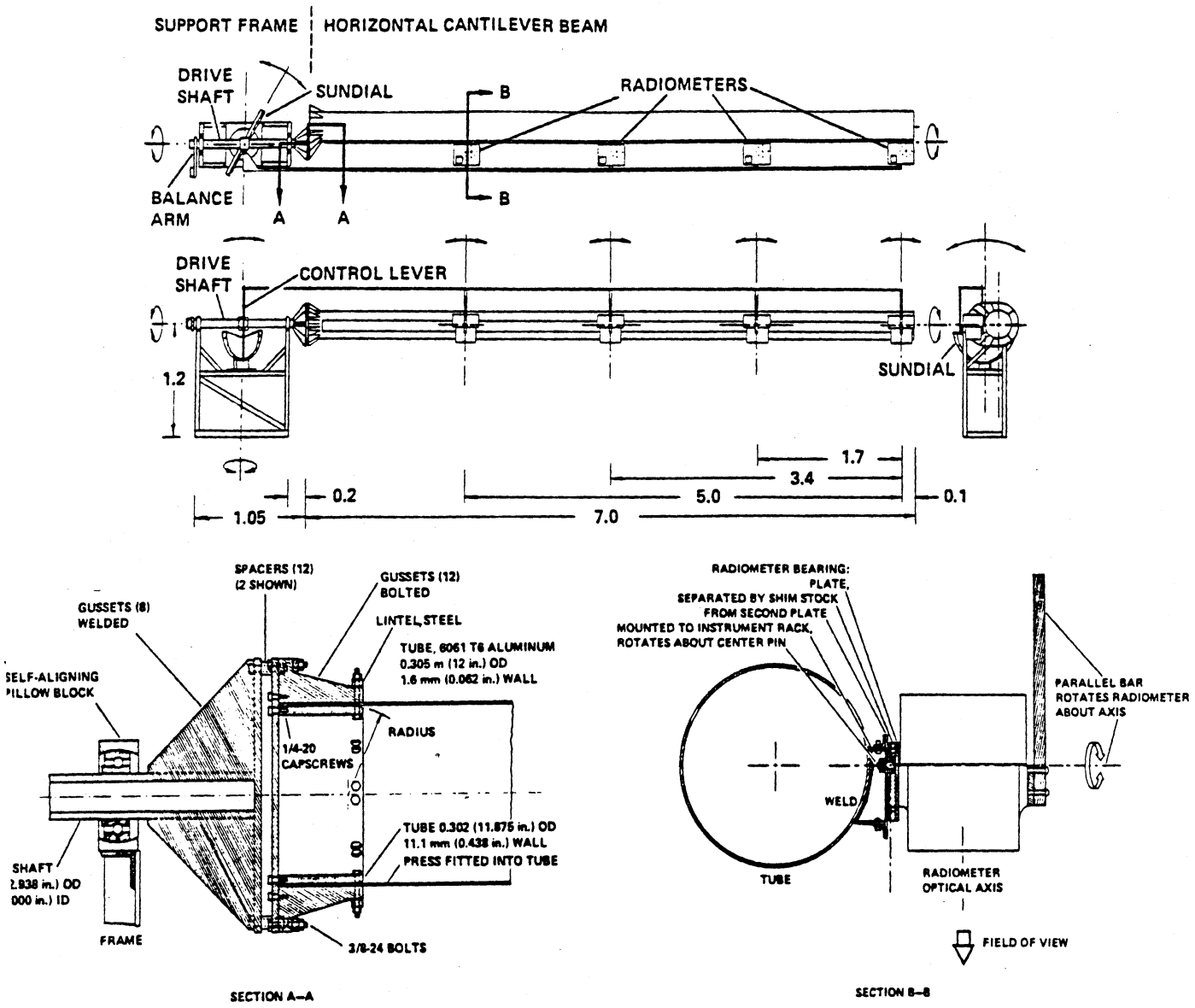

. The gantry supports four radiometers for measuring the canopy radiance in any of 11 view directions (zenith angles) in the principal of the sun. Dimensions are in meters.

. *Horizontal cantilever beam*

ıorizontal cantilever beam (Figs. 1 to 3) consists of a lrical tube, 7 m in length, with an instrument rack riveted udinally along the outside surface. The tube is constructed 51-T6 aluminum, welded longitudinally along the inside, n outer diameter of 0.30 m, a wall thickness of 1.59 mm, total mass of approximately 29 kg (West Coast Tube and Agoura Hills, Calif.). To increase the strength of the weld he instrument rack (Fig. 3, section B-B) is riveted directly ıe weld seam, with one row of rivets on each side of the

ched to one end of the horizontal cantilever beam is a ing flange. Bolted gussets brace the flange to the wall of indrical tube. A short length of aluminum pipe (outer wall er 30.163 cm × 15 cm length × 1.11 cm), press-fitted : cylindrical tube, provides strength to the tube in the area gussets. The end of the 1.11 cm pipe (Fig. 3, section A-A) ded to prevent the concentration of stress at that location vall of the cylindrical tube.

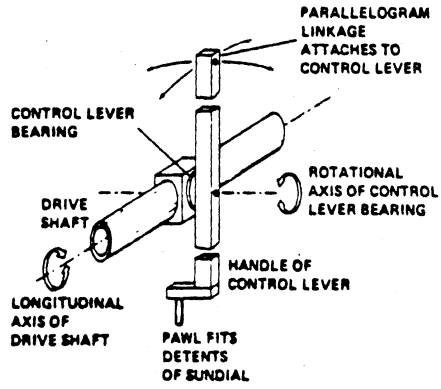

Fig. 4. The control lever, through rotation about two axes, points the radiometers in the direction defined by the axis of the pawl.

Each radiometer (Fig. 3, section B-B) is attached to the instrument rack with the aid of a radiometer bearing formed from two plates that pivot about a center pin and are thinly separated by lubricated shim stock. The radiometer bearings are

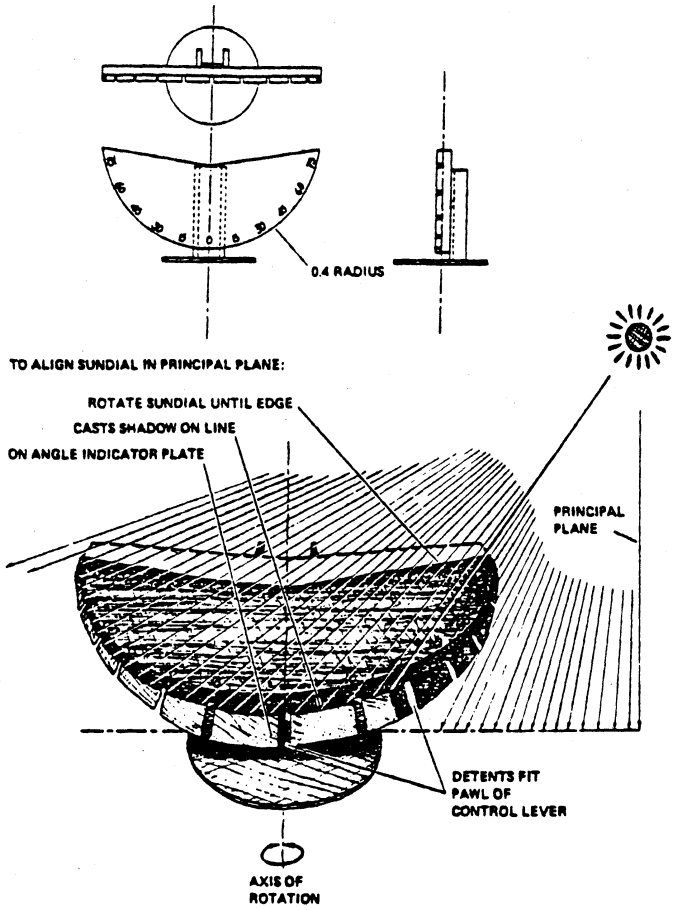

Fig. 5. On the sundial, which is rotated to the solar azimuth, detents accept the control lever pawl and thereby allow the optical axes of the radiometers to be pointed in parallel in any one of 11 zenith angular directions in the principal plane of the sun.

mounted so that their axes of rotation are parallel, allowing the radiometers various view directions toward or away from the manlift.

The number of radiometers that can be mounted on the instrument rack is limited by their combined weight. At full load, the system is designed to accept six Barnes MMR radiometers, each 5 kg, spaced equally along the length of the beam and one motor-driven 35 mm camera mounted at the end of the beam. At full load, the system is designed to withstand 4 g dynamic loads applied in the vertical direction. At the end of the beam, the vertical deflection due to bending in the horizontal cantilever beam and in the drive shaft is calculated to be 5 cm at static full load.

To prevent secondary illumination (e.g., due to sunlight specularly reflected by the side of the tube) from reaching the target—particularly the calibration panel—a black, coarse mesh of plastic material (medium Weathashade, Weathashade, Inc., Apoka, Fla.) was sewn to form a sock around the tube. To further reduce the possibility of unwanted specular reflection, the mesh on the sides of the tube was sprayed with matte black paint containing a carbon black pigment.

2.2.2. Support frame

The support frame (Fig. 3), a truss of aluminum angle and channel beams, is anchored with 1.3 cm bolts to steel channel beams in the floor of the basket of the manlift. Both the drive

TABLE I. Estimates of the mean and CV of the BRF of the walnut canopy measured in seven wavelength bands having approximately the spectral characteristics of the Landsat Thematic Mapper. There are 180 measurements represented by the CV for all data and 20 by the CV and the nugget for track 5. Each measurement is defined as an average of the data collected simultaneously from the four radiometers at a point along the track traveled by the manlift; thus, 20 measurements represent acquisition of 80 radiometric data points. The view direction is nadir, and solar zenith and azimuth angles are approximately 39° and 238°.

Band	Wavelength range, μm	Estimated mean bidirectional reflectance factor (BRF), %	Coefficient of variation (CV) All data, %	Track 5, %	nugget track 5, %
1	0.45-0.52	2.8	30.7	15.9	10.8
2	0.52-0.60	4.5	32.2	15.6	12.2
3	0.63-0.69	4.0	32.5	18.8	8.0
4	0.76-0.90	25.8	35.0	10.7	13.2
5*	1.15-1.30	26.1	30.5	9.9	10.7
6*	1.55-1.75	15.0	30.5	11.2	9.7
7*	2.08-2.35	6.6	32.0	15.5	7.6

*These band numbers do not correspond to the band numbers of the Landsat Thematic Mapper, which does not have a wavelength band from 1.15 to 1.30 μm.

shaft and the sundial are attached to the support frame. Its height, 1.5 m, allows elevation of the horizontal cantilever beam above the top edge of the basket of the manlift, permitting the gantry to be mounted without modification of the basket.

The drive shaft, an aluminum pipe with a flange and bracing gussets welded to one end, attaches through a bolt ring to the mating flange of the horizontal cantilever beam. The drive shaft attaches to the support frame through two pillow block bearings that permit the drive shaft/beam assembly to rotate about the longitudinal axis of the drive shaft.

The longitudinal axes of the drive shaft and horizontal cantilever beam are parallel but are offset 15 cm. The offset places the center of gravity of the assembly (drive shaft, horizontal cantilever beam, radiometers, and camera) closer to its axis of rotation (the axis of the drive shaft), and thereby facilitates rotationally balancing the system with the addition of minimal amounts of dead weight. Balancing is accomplished by adjusting both the angle of the balance arm (Figs. 1 to 3), clamped to project radially from the drive shaft, and the radial position of the balance mass, which is bolted to the balance arm.

2.2.3. Control lever

All radiometers may be pointed simultaneously to any desired zenith and azimuth view direction by moving the handle of the control lever (Figs. 3 and 4) about either or both of its two orthogonal axes of rotation. When the handle is moved about the first axis, it rotates the drive shaft/horizontal cantilever beam assembly and the attached radiometers about the longitudinal axis of the drive shaft. When the handle is moved about the second axis, that of the control lever bearing, the radiometers are simultaneously rotated with the aid of a parallelogram linkage that connects the control lever to parallel bars attached to

:h radiometer. The control lever handle always points in the ection of view of the radiometers.

.4. Sundial

: sundial (Fig. 5), used with the control lever, permits identi- ıtion of the desired zenith view directions of the radiometers he principal plane of the sun. To identify the principal plane, sundial is rotated until its top edge is pointed in the solar nuth direction. When oriented at this angle, the partially truding top edge casts a sun shadow along a corresponding painted on the angle indicator plate. The plate forms a -circle centered at the intersection of the three axes of rota- , two of the control lever and one of the sundial. Proper ation of the sundial requires that the basket of the manlift be l, ensuring that the rotational axis of the sundial is vertical thus that the principal plane is correctly identified. Once this e is identified, the desired zenith view direction is selected ıoving the pawl of the control lever handle into one of the ıts located at 15° increments in the angle indicator plate.

ANOPY REFLECTANCE

Calibration

ration of all radiance data to determine the BRF was ac- ılished with reference to a field calibration standard, a)4 painted, 1.3 m × 1.3 m aluminum panel. (The results ported as BRF and not as a bidirectional reflectance distri- ı function, an alternative descriptor of the light scattering rties of the canopy.[16]) The BRF of the field standard was nined from comparison with pressed $BaSO_4$ measured in boratory. Nicodemus et al.[16] and Milton[14] describe the ions and procedures for obtaining the reflectance factor. g measurement, the field calibration panel was level and)cated on top of a 7 m tower, 2 m higher than the tree y, so that light scattered by foliage would not illuminate nel, thereby affecting the calibration measurements. Dur- ta collection, a recording pyranometer was used to moni- solar insolation, providing assurance that the quality of ctral data was not compromised due to clouds.

BRF of the plant canopy measured in each wavelength as approximated as a biconical reflectance factor deter- by using the formula

$$;i;r;x,y) = \frac{V_{canopy} - V_{dark}}{V_{cal} - V_{dark}} BRF_{cal}, \quad (1)$$

V_{canopy}, V_{cal}, and V_{dark} are the voltages of the radiometer ıe orchard, calibration panel, and zero light (instrument ponse) were measured. In Eq. (1), the letter l signifies gth band, (x,y) is a horizontal position relative to the and the i and r correspond to the directions in which incident and reflected, respectively. BRF_{cal} is the BRF libration panel measured in the laboratory at an incident tion angle of 10° and radiometer view direction of nadir. = of the panel was not corrected for the incident illumin- gle. Each radiometer measurement of the orchard at one time was calibrated using a linear interpolation pro- pplied to calibration panel measurements acquired at fore and after collection of the orchard measurements.

irectional reflectance factor of the canopy

py BRF for specific directions of irradiation and reflec- tion (i;r) is the flux from the canopy, measured both for directions (i;r) and within the solid angle of the instrument, divided by the flux that would be received from a hypothetical, perfectly white, perfectly diffuse, level calibration surface also measured for (i;r) by the same instrument. We shall assume that both the canopy and the calibration surface are equal in area. The flux from the canopy is found as an integral of the flux Φ from each $\Delta x \Delta y$ area:

$$BRF = \frac{\Phi_{canopy}}{\Phi_{calibration}} \quad (2a)$$

$$= \frac{\iint_{canopy} \Phi(l;i;r;x,y)dxdy}{\iint_{calibration} \Phi(l;i;r;x,y)dxdy}. \quad (2b)$$

The flux in the denominator of Eq. (2b) is a constant, indicating that the flux reflected by the calibration panel does not vary as a function of the (x,y) position and that it may be taken outside the integral. Dividing this constant calibration flux into the flux from the canopy [the numerator of Eq. (2b), which does vary with (x,y) position], we find that the BRF of the canopy is the integral of the value of the BRF_{xy} at each point above the canopy normalized by the area of the calibration panel. But we have assumed that the measured areas of both the calibration panel and the canopy are identical; thus,

$$BRF(l;i;r) = \frac{\iint_{canopy} BRF_{xy}(l;i;r;x,y)dxdy}{\iint_{canopy} dxdy}. \quad (3)$$

4. TEST AND EVALUATION OF SYSTEM: WALNUT CANOPY REFLECTANCE

4.1. Data acquisition

To evaluate the tree canopy radiance measurement system, data were acquired at the Kearney Agricultural Center (at Parlier, Calif., 36° 36′ north latitude, 119° 31′ west longitude) of the University of California at Davis on Aug. 24, 1987. Data were collected on an irrigated orchard (Fig. 6) of six-year-old black walnut trees (*J. hindsii*) of the "Chico" J. regia (English) variety. The localized spray irrigation system had been operated during the night prior to data collection, leaving the soil surface a mottled mixture of wet and dry, dark and light areas.

The trees were approximately 5 m tall and planted 3.4 m apart in rows 6.7 m wide. The tree crowns were closed (i.e., contiguous) within the rows but not between rows; the ground cover was estimated to be 65%.

Spectral data were collected periodically in time as the manlift with the four radiometers 11 m above the soil was driven slowly back and forth on eight parallel tracks on a short roadway adjacent to the walnut canopy (Fig. 6). At each of the along-track points at which data were acquired, the outputs of the radiometers were sampled in each wavelength band. Eighty data points were acquired on each track in each wavelength band, 40 as the manlift was driven forward on the track, then 40 additional points as the manlift was driven backward on the same

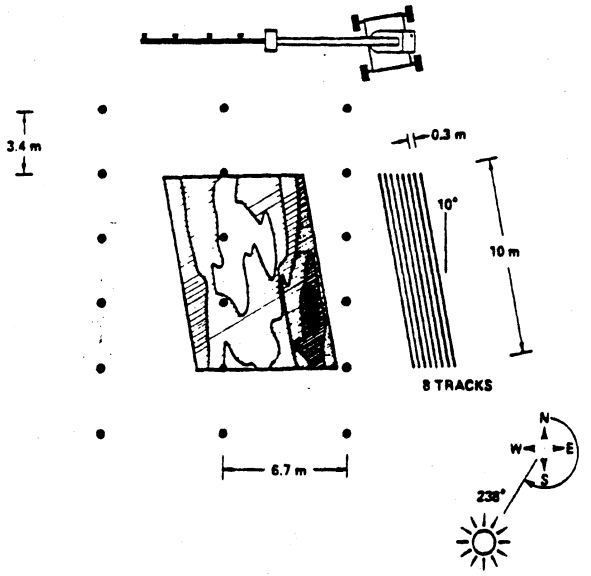

Fig. 6. Plan view of walnut orchard overlaid with normalized difference vegetation index ($NDVI_{xy}$) data. Black dots represent the locations of tree trunks; gray shading represents tree foliage. The radiance data were acquired in the nadir direction by the four radiometers of the tree canopy radiance measurement system as the manlift was driven along each of eight tracks located on a road adjacent to the canopy. The tower used to support the white calibration surface above the canopy was located off the map, 10 m south of the eight tracks. On the plot of $NDVI_{xy}$, the black area represents values from the minimum observed value (0.52) to 0.57, represented by the contour line. Subsequent contours represent values of 0.62, 0.67, 0.72, and 0.77. The white area represents values from 0.77 to the maximum observed value (0.82). The view direction is nadir and illumination zenith and azimuth angles are approximately 39° and 238°.

track. Nine data sets totaling 720 measurements were acquired in each of the seven wavelength bands in the nadir viewing direction between 3:00 and 3:30 p.m. Pacific Daylight Time (22:00 to 22:30 GMT). To gauge the effect of the changing sun angle during data collection, the last data set was acquired on the same track used to acquire the first data set. All spectral data were collected in the nadir view direction, one of 11 possible zenith angle view directions with the tree canopy radiance measurement system.

4.2. BRF of a periodic structure

A practical objective in the design of the tree canopy radiance measurement system was to minimize the use of radiometers, which are expensive to purchase and difficult to borrow. This goal was addressed by selecting the positions of the radiometers to aid in sampling the $BRF_{xy}(l;i;r;x,y)$. Because of the pronounced row structure of the canopy, we expected a priori that BRF_{xy} should be quasi-periodic in x in the sense that BRF_x is periodic in x; thus, the integral in the along-row direction y,

$$BRF_x(l;i;r;x) = \int BRF_{xy}(l;i;r;x,y)dy\,, \tag{4}$$

is periodic in x with a period of 6.7 m. Thus,

$$\int BRF_{xy}(l;i;r;x,y)dy = \int BRF_{xy}(l;i;r;x+6.7,y)dy\,. \tag{5}$$

Making this assumption of periodicity allowed us to modify the trapezoidal formula for numerical integration. The modified formula weighted equally data from four radiometers, located as shown in Fig. 3, and did not require use of a fifth radiometer located at x = 6.7 m, one period. All of this means that the integration, Eq. (3), can be approximated as

$$BRF(l;i;r) \approx \frac{\sum_{j=1}^{20}\sum_{k=1}^{4} BRF_{xy}(l;i;r;x_j,p_k)A}{80A}\,, \tag{6}$$

where A, the area of the field of view of each radiometer, may be canceled from numerator and denominator and the p_k are positions at which data were acquired in the along-track direction traveled by the manlift. In the across-row direction, the x_j are the positions of the four radiometers measured from the end of the horizontal cantilever beam (Fig. 3).

For purposes of statistical analysis, the two summations in Eq. (6) were performed separately, first yielding

$$BRF_y(l;i;r;p_k) \approx \frac{\sum_{j=1}^{4} BRF_{xy}(l;i;r;x_j,p_k)}{4}\,, \tag{7}$$

where BRF_y represents an estimate of the mean of the point-by-point canopy reflectance, BRF_{xy}, averaged along the cross-row transect corresponding to position p_k. The BRF of the canopy and the coefficient of variation were estimated from the average of 20 values of BRF_y representing the data from one track:

$$BRF(l;i;r) \approx \frac{\sum_{k=1}^{20} BRF_y(l;i;r;p_k)}{20}\,. \tag{8}$$

4.3. Data analysis

4.3.1. Spatial variability of data

The magnitude of the (x,y) spatial variability of the data was examined with the intent of documenting the need for a spatial sampling methodology. To do this, the normalized difference vegetation index ($NDVI_{xy}$) was plotted against the rows of foliage that form the dominant feature of the canopy architecture. Here $NDVI_{xy}$ is defined from the BRF_{xy} in the near infrared (band 4) and red (band 3) spectral regions:

$$NDVI_{xy} = \frac{BRF_{xy}(4;i;r;x,y) - BRF_{xy}(3;i;r;x,y)}{BRF_{xy}(4;i;r;x,y) + BRF_{xy}(3;i;r;x,y)}\,. \tag{9}$$

Often employed in remote sensing research, NDVI provides an indication of the photosynthetic capacity of a plant canopy.[17,18] Typical values of NDVI range from near 1.0 for a dense, green, actively photosynthesizing plant canopy to approximately 0.1 for sparse vegetation growing under desert conditions. NDVI is most often computed using satellite sensor radiances rather than reflectance factors. Our definition, involving BRF rather than radiance, does not affect the results of the spatial analysis, but some $NDVI_{xy}$ values reported here may differ from those that would be obtained from a satellite sensor measuring the walnut canopy. The NDVI of the canopy is determined by appropriately averaging the per-point $NDVI_{xy}$.

Figure 6 displays the spatial variability of the $NDVI_{xy}$ as a function of position in directions both across and along the rows

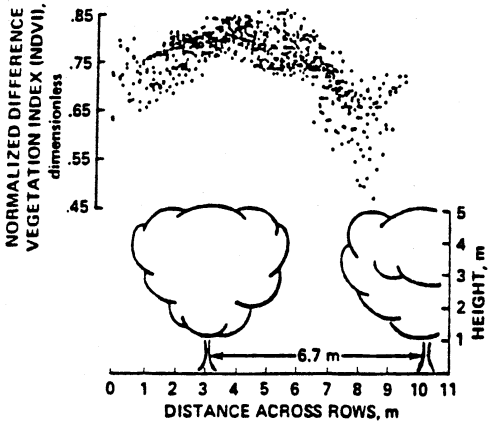

7. Variation of $NDVI_{xy}$ with distance across the rows of walnut ıs. The viewing direction of the plotted data is toward the north. view direction of the radiometer is nadir and illumination zenith, the azimuth angles are approximately 39° and 238°.

walnut trees. Figure 7 displays the spatial variability of the VI_{xy} across the rows. As shown in Figs. 6 and 7, the ıllest values (0.52) of $NDVI_{xy}$ correspond to locations be-en the rows of trees, where the field of view of the radi-ɛter was more likely to include shadowed soil. The largest ıes (0.84) of $NDVI_{xy}$ correspond to locations on the rows of s where the field of view of the radiometer was most likely to ude sunlit foliage.

hese results (Figs. 6 and 7) show that $NDVI_{xy}$ varied in a ial pattern corresponding to the row structure of the canopy. ratio of the largest value (0.84) of $NDVI_{xy}$ to the smallest 2) is 1.6; no one of these $NDVI_{xy}$ estimates, chosen ran-ıly, can be expected a priori to represent the NDVI of the ɔpy. The results affirm the need for an appropriate measure-ıt strategy with which to sample this spatial variability.

2. *Statistical analysis of data*

each wavelength band, two specific statistical issues were stigated. First, are the estimates of the canopy BRF biased ırding to track number? Second, in estimation of the canopy ', what are its statistical properties and how many data ts should be acquired?

2.1. *Estimated BRF biased by track*

lefinition, the BRF of a plant canopy represents the entire py; it does not depend upon the (x,y) location of the sensor to acquire the data. The estimates of the walnut canopy do appear to depend upon the sensor location (i.e., the that the manlift traveled), decreasing, as Fig. 8 shows, increasing track number. The downward trend in the BRF ıe canopy was statistically modeled for each wavelength with the aid of a linear regression of the data (Fig. 8) as a ion of time. The data from the revisit of track No. 1 at 5 GMT were excluded from the analysis.

terpretation of the downward trend in the estimates of the py BRF is complicated by the fact that the data for all eight s were collected during a 0.5 h period, and therefore the number (Fig. 8) corresponds both to a set of data acquisi-locations (the portion of the canopy measured as the manlift led that track) and to the sun angles at which the data were ired. Indeed, the fact that for each wavelength band there is ference in the BRF estimated for the first and last data sets,

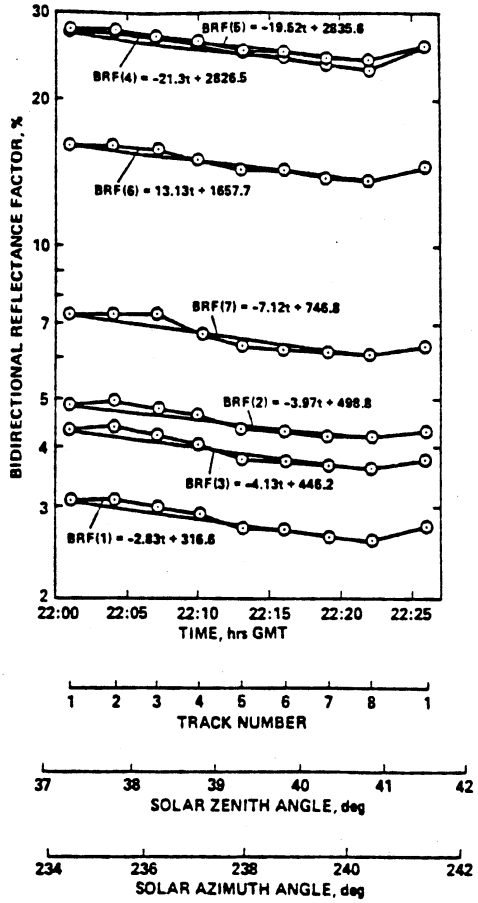

Fig. 8. Estimates of the canopy BRF for each track traveled by the manlift. Wavelength bands are listed in Table I. Each equation is a linear regression of the eight estimates of the canopy BRF for each wavelength band. The data acquired at 22:26 GMT were excluded from the analysis. Note that the per-point $NDVI_{xy}$ results (Figs. 6 and 7), if they were spatially averaged, could be compared to a canopy NDVI estimated from the results in this figure.

both acquired on track No. 1, suggests that at least part of the systematic decrease in the estimated BRF (Fig. 8) is due to changing sun angles. Another factor to consider in understanding the decrease is an edge-of-field effect, possibly present in the data acquired where the radiometers viewed the row of trees bordering the orchard. The downward trend is likely not due to a track-dependent bias. Such a bias would tend to be oscillatory, with a period fixed by the distance between radiometers, rather than approximately linear as shown in Fig. 8. The results (Fig. 8) suggest that the overall downward trend is due to both a changing sun angle and an edge-of-field effect.

Evidence for an oscillatory, track-dependent bias in the estimates of the BRF of the canopy was investigated with the aid of the residual, the difference between the actual BRF and the BRF predicted using the regression equations (Fig. 8). The results (Fig. 9) show that for each wavelength band, the residual normalized by the mean, $(BRF - \widehat{BRF})/\overline{BRF}$, varies up to 3.5% about the regression line (Fig. 8). The three factors—changes in sun angle (Fig. 8), an edge-of-field effect, and a track-dependent bias—must be considered for understanding the oscillatory pattern (Fig. 9). However, the spatial period of the pattern, approximately the distance 1.67 m between the radiometers on the horizontal cantilever beam, corresponds to a property of the measurement process rather than the canopy architecture or sun

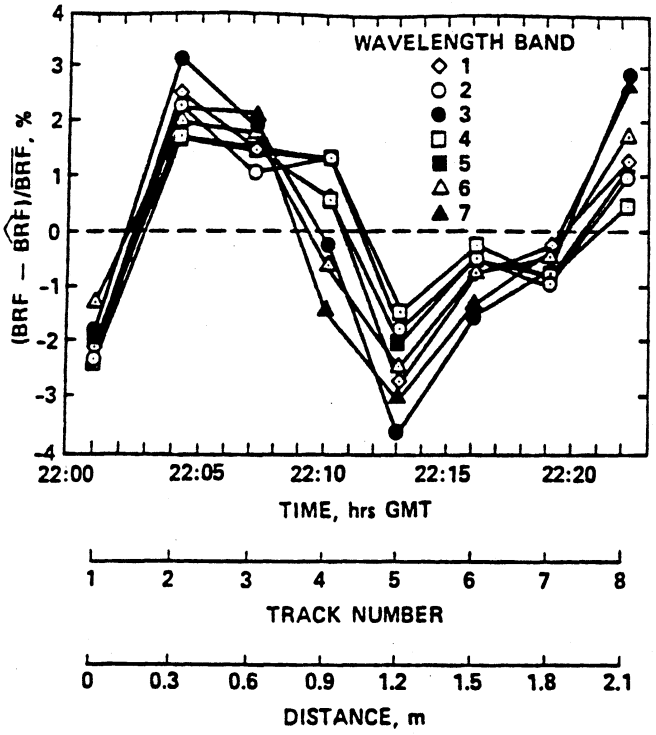

Fig. 9. For each wavelength band, the residual of a linear regression of the data (Fig. 8), normalized by the mean, shows the percent deviation from the downward trend in the estimated BRF of the canopy.

angle changes. This supports the hypothesis that the procedure for estimating the BRF of the canopy includes a bias dependent on the track traveled by the manlift. The magnitude of this bias, less than 3.5% of the measured value, is comparatively small and apparently predictable. If it is not removed from the data, then it will add to the uncertainty in the estimates of canopy BRF. The fact that the bias exists shows that the sampling strategy developed for locating the radiometers along the length of the horizontal cantilever beam (Fig. 3) may be improved by taking advantage of a priori knowledge of the BRF_{xy}.

4.3.2.2. Statistics of estimated BRF

Table I shows the mean (i.e., the canopy BRF) and coefficient of variation (CV) of BRF_y [Eq. (7)], both determined from all BRF_y from all tracks, providing a total of 180 data points. View direction is nadir. Solar zenith and azimuth angles were approximately 39° and 238° (Fig. 8). The mean shows the expected[5,7,8] "green vegetation" variation with wavelength, while the CV for all data is almost a constant, varying only from 31% to 35%. Table I shows that the CV for track 5, the track with the largest individual CV, ranged from 9.9% in band 5 to 18.8% in band 3.

Both periodic and random spatial variation of the canopy reflectance contribute to the magnitude of the CV. This spatial variation in the data of each track may be characterized with the aid of the semivariogram.[19,20] Table I shows that the value of the nugget of the semivariogram for each wavelength band for track 5 was approximately ⅓ of the value of the CV of the track. This suggests that approximately ⅔ of the CV is attributable to microscale variability of the data, which represents both scene variability at a higher spatial frequency than the sampling frequency and measurement noise. The size of this "white noise," rather than the size of the spatially correlated variability (the remaining ⅓ of the CV for these data), is the value of importance that determines the statistical significance and statistical power associated with an estimate of the mean value of the data. The size of the nugget should not exceed the CV. Comparison shows that two values (13.2% of band 4 and 10.7% of band 5) do. This provides an indication of the potential inaccuracy in these nugget estimates, which are based on only 20 data points. If the value 13.2% is disregarded, the largest value of the nugget is 12.2%.

TABLE II. Minimum number of measurements required for detecting true differences among treatments using CV = 0.12 and an α = 0.05 test of significance. Each measurement is defined as an average, by wavelength, of the four data points collected simultaneously from the four radiometers of the tree canopy measurement radiance system.

	True difference as percent of mean				
Power*	20	10	5.0	2.5	1.0
	number				
0.80	6	23	91	362	2258
0.85	7	26	104	415	2592
0.90	8	31	122	487	3042
0.95	10	38	150	598	3733
0.98	12	48	189	756	4724
0.99	14	55	218	872	5450

*Power relates to the probability that we will detect a difference that is there.

The number of data points required to estimate the canopy BRF was investigated using the approach to statistical power found in Howell.[21] Table II shows the minimum number of measurements required for detecting true differences among treatments as a function of power using an α = 0.05 test of significance. Each measurement is an average of the data from the four radiometers. It is assumed that the track-dependent bias has been removed from the estimates of BRF. The results are predicated on the approximate upper bound on the value of the nugget (12%) in Table I. These numbers represent in effect a lower limit to the number of measurements required to estimate a mean for data having the type of "white noise" properties represented by the nugget. Values of α and power were selected to obtain a low probability of finding a true difference in the mean (the canopy BRF) that is not there (therefore α = 0.05) and a high probability of finding a true difference that is there (therefore values of power > 0.8).

The results, Table II, demonstrate that a comparatively large data set must be acquired if the reflectances of two similar canopies are to be distinguished. For example, if we acquire 31 measurements (each defined as an average of the data of the four radiometers, 4×31 = 124 total data points) on each of two treatments for which the true means (the canopy BRF of each treatment) differ by 10% and use an α = 0.05 test of statistical significance, then 90% of the time we will reject the null hypothesis and accept correctly the hypothesis that this difference exists. Or 95% of the time we will accept correctly the hypothesis that a true difference of 5% exists in the means, if we acquire 150 measurements and again use an α = 0.05 test of significance.

We actually acquired 20 measurements on each track, which means that we can detect true differences of 12% with a power of 90%, using an α = 0.05 test of significance.

4.4. Vegetation results

The estimate of the spectral BRF of the walnut orchard, Table I, appears typical of the spectral BRF of other healthy, green vegetation canopies.[5,7,8] The estimated BRF is relatively small in the chlorophyll absorption region (the blue and red regions), relatively large in the green spectral region, larger still in the middle infrared (bands 6 and 7), and largest in the near infrared (bands 4 and 5).

The large variability in the canopy architecture, due to the pronounced, widely spaced rows of foliage and soil, manifests significant variability in the BRF_{xy} but a comparatively small coefficient of variation of the BRF_{xy} of the canopy. These results affirm the validity of the process for estimating the BRF of the canopy—as an average of the BRF_{xy} provided by four appropriately placed radiometers. There is evidence for track-dependent bias in the estimates of the canopy BRF. But the comparatively small value of this bias, less than 3.5% of the measured value, affirms the validity of the sampling strategy concerning where to place the radiometers on the horizontal cantilever beam. And because this bias appears to be predictable, it may be removed from the estimated BRF a posteriori. These results provide the a priori information needed for developing an unbiased sampling strategy for future data collection efforts involving the walnut orchard.

A total of 20 measurements (each an average of the data of four radiometers) were acquired in 3 min to estimate the canopy BRF and detect true differences of 12% of the mean approximately 90% of the time.

RECOMMENDATIONS

We have three recommendations concerning improvements that could be made in the design of the tree canopy radiance measurement system and one recommendation concerning the comparison of the estimated BRF shown in Table I with the BRF predicted by canopy reflectance models.

We recommend increasing the strength of the drive shaft to provide a 4 g safety margin. The drive shaft, a critical part of the system, does not meet the design criterion for withstanding a 4 g inertial force because of its relatively small outer diameter (7.6 cm) and the fact that it was machined down to slip fit into the pillow block bearings. When loaded, the shaft has a stress concentration at a circumscribed groove located forward of the pillow block 30 cm behind the shaft/beam flange connection. This shallow undercut groove is necessary for machining purposes to ensure the correct shaft diameter at the pillow block bearings.) Consequently, the safety factor for the current drive system is only 2.4. To increase the strength of the drive shaft, we recommend increasing its diameter. For example, increasing the shaft diameter to 9.5 cm, while maintaining the same wall thickness, increases the safety factor to 4.1, with a weight penalty of only 4 kg. In addition, the increase in shaft diameter reduces the amount of deflection at the beam's free end by a highly desirable design objective for measurement accuracy.

We recommend increasing the memory capacity of the data acquisition system of the tree canopy radiance measurement system to permit system operation for an extended period of time, preferably for all day without interruption. The system presently reached memory capacity after acquiring approximately 1000 data points during a period of 0.5 h and required frequent interruptions during which the contents of the memories of the Polycorders were transferred to a laboratory computer. A portable computer dedicated to storing the radiance data as they are acquired by the Polycorders is one possible solution to this problem.

We recommend altering the method by which the view direction is selected so that the radiometers might be pointed in all view directions, not just those in the principal plane. This could be accomplished by replacing the sundial with a sun dish, a portion of a sphere centered at the same point as the angle indicator plate, that is, at the intersection of the axes of the drive shaft and the control lever bearing. Like the sundial, the sun dish would be oriented in the solar azimuth direction during operation. Various radiometer view directions would be identified with the aid of holes in the sun dish into which the pawl would be extended axially from the control lever handle.

Finally, we recommend that those seeking to compare the results reported here with results obtained from satellite sensor data or using models for the canopy reflectance take into account both the field of view, 15°, and the altitude of the measuring radiometers, a bit more than twice the canopy height. First, rather than integrating within an angular FOV, models and satellite sensors typically represent the canopy reflectance for a collimated view. Second, in the results reported here, there is an interaction between the noncollimated FOV and the altitude such that the light received from a scatterer is differentially weighted according to its height. Because of these two effects, that is, a noncollimated FOV and the interaction between the FOV and the sensor altitude, each radiometric measurement will be unlike those obtained from a satellite sensor, a fact that must be taken into account in the modeling process if valid comparisons are to be made.

6. SUMMARY

The tree canopy radiance measurement system is a practical approach to estimating the BRF of a tree canopy displaying large heterogeneity as a function of horizontal location. The fact that within a short time period high quality spectral data were acquired over a tree canopy approximately 5 m tall displaying a heterogenous foliage distribution provides validating evidence of the utility of the design and of the use of four radiometers to average out much of the spatial variability. For the walnut canopy, a total of 20 measurements (each measurement is defined as the average of the data from the four radiometers) was acquired in 3 min to estimate the canopy BRF and detect true differences of 12% of the mean approximately 90% of the time. In these results only the nadir view direction was used. The system has already been used to measure an additional tree canopy, viewed from 11 directions, and will be employed in the future to obtain better understanding of the BRF of tree canopies.

7. ACKNOWLEDGMENTS

This work was performed for the Jet Propulsion Laboratory, California Institute of Technology, and was supported by the National Aeronautics and Space Administration program on Eos Synergism.

We thank Barry D. Ganapol of the University of Arizona, Tucson, for his good humored assistance in the design and construction of the gantry, a task performed in the summer heat of Fresno, Calif., for which success, just as Thomas A. Edison said, was more than 98% perspiration.

We thank the manager and staff of the Kearney Agricultural Center of the University of California at Davis for access to the machine shop and facilities of the center and Dave Goldhamer of the University of California at Davis for use of the walnut orchard for data collection.

We thank Harry Brining of Grove Manufacturing, Shady Grove, Pa., for advice and information about the capabilities of manlifts.

Finally, we thank the team that made the effort possible: JoBea Cimino, Craig Dobson, Jack Paris, Susan Ustin, Guy Cook, Jenny Clark, Eric Kasischke, and Kevin Berger.

8. REFERENCES

1. C. S. T. Daughtry, V. C. Vanderbilt, and V. J. Pollara, "Variability of reflectance measurements with sensor altitude and canopy type," Agron. J. 74, 744–751 (1982).
2. J. A. Smith, "Matter-energy interaction in the optical region," in *Manual of Remote Sensing*, Second Edition, R. N. Colwell, editor-in-chief, pp. 61–113, Am. Soc. of Photogram., Falls Church, Va. (1983).
3. "Earth system science, a program for global change," NASA, Washington, D.C. (May 1986).
4. "Earth system science, a closer view," Rept. of Earth System Sciences Committee, NASA Advisory Council, NASA, Washington, D.C. (Jan. 1988).
5. K. T. Kriebel, "Measured spectral bidirectional reflection properties of four vegetated surfaces," Appl. Opt. 17(2), 253–259 (1978).
6. N. S. Goel and D. W. Deering, "Evaluation of a canopy reflectance model for LAI estimation through its inversion," IEEE Trans. Geosci. Remote Sens. GE-23, 674–684 (1985).
7. K. J. Ranson, C. S. T. Daughtry, L. L. Biehl, and M. E. Bauer, "Sun-view angle effects on reflectance factors of corn canopies," Remote Sens. Environ. 18, 147–161 (1985).
8. K. J. Ranson, L. L. Biehl, and M. E. Bauer, "Variation in spectral response of soybeans with respect to illumination, view, and canopy geometry," Int. J. Remote Sens. 6, 1827–1842 (1985).
9. K. J. Ranson, C. S. T. Daughtry, and L. L. Biehl, "Sun angle, view angle and background effects on response of simulated balsam fir canopies," Photogram. Eng. Remote Sens. 52, 649–658 (1986).
10. D. S. Kimes, W. W. Newcomb, R. F. Nelson, and J. B. Schutt, "Directional scattering properties of a wintering deciduous hardwood canopy," IEEE Trans. Geosci. Remote Sens. GE-24, 281–293 (1986).
11. D. S. Kimes and W. W. Newcomb, "Directional scattering properties of a wintering deciduous hardwood canopy," IEEE Trans. Geosci. Remote Sens. GE-25, 510–515 (1987).
12. S. A. W. Gerstl and A. Zardecki, "Coupled atmosphere/canopy model for remote sensing of plant reflectance features," Appl. Opt. 24, 94–103 (1985).
13. S. A. W. Gerstl and C. Simmer, "Radiation physics and modeling i off-nadir satellite sensing of non-Lambertian surfaces," Remote Ser Environ. 20, 1–29 (1986).
14. E. J. Milton, "Principles of field spectroscopy," Int. J. Remote Sens. 1807–1827 (1988).
15. B. F. Robinson, M. E. Bauer, D. P. DeWitt, L. F. Silva, and V. Vanderbilt, "Multiband radiometer for field research," in *Measurements Optical Radiations*, Proc. SPIE 196, 8–15 (1979).
16. F. E. Nicodemus, J. C. Richmond, J. J. Hsia, I. W. Ginsberg, and Limperis, "Geometrical considerations and nomenclature for reflectanc NBS monograph 160, Nat. Bur. of Stand., Washington, D.C. (1977).
17. P. J. Sellers, "Canopy reflectance, photosynthesis, and transpiration," I J. Remote Sens. 6, 1335–1372 (1985).
18. P. J. Sellers, "Canopy reflectance, photosynthesis, and transpiration II. T role of biophysics in the linearity of their interdependence," Remote Ser Environ. 21, 143–183 (1987).
19. A. G. Journel and C. J. Huijbregts, *Mining Geostatistics*, Academic Pre New York (1978).
20. P. J. Curran, "The semivariogram in remote sensing: an introduction Remote Sens. Environ. 24, 493–507 (1988).
21. D. C. Howell, *Statistical Methods for Psychology*, Duxbury Press, Bosto Mass. (1982).

William F. Caldwell received the BS degr in mechanical engineering in 1988 from t University of California at Davis. He is cu rently a mechanical design engineer f NASA Ames Research Center and is workir toward the MS degree in mechanical eng neering at Stanford University, Palo Alt Calif.

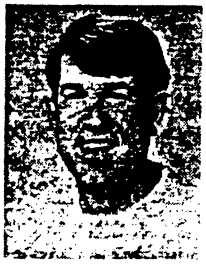

Vern C. Vanderbilt is a senior research scie tist at the Ames Operations of TGS Techno ogy, with research interests in the light-sca tering characteristics of plant canopies an leaves and also in the development of th sensors associated with measuring suc characteristics. Dr. Vanderbilt earned his B MS, and Ph.D. degrees in electrical enginee ing from Purdue University, where he serve first as a postdoctoral fellow and then as research engineer in the Laboratory for Ap plications of Remote Sensing.

WATER RELATIONS OF A WALNUT ORCHARD: SIMULTANEOUS MEASUREMENT WITH REMOTE SENSING

J A Weber
Biological Station
The University of Michigan
Ann Arbor, MI 48109-1048, U.S.A

S L Ustin
Department of Botany
University of California
Davis, CA 95616, U.S.A

ABSTRACT

Water relations of trees vary over time scales of hours to weeks. The effect of changes in water status on microwave backscatter measurements from tree canopies was determined. Of the several parameters measured, leaf xylem water potential showed the greatest diurnal variation and appeared to co-vary in time with C-, L-, and X-band microwave measurements. In addition data collected with L-band dielectric probes embedded in the trunk of selected trees showed parallel temporal variations. It is unlikely that water potential, per se, is being sensed; however, water potential of the leaves is a sensitive measure of overall plant water status and is a useful parameter for connecting remotely sensed data to plant activity.

Keywords: water potential, water content, relative water content, transpiration

1. INTRODUCTION

Study of water relations of encompasses not only water status but also the dynamic processes of transpiration and water flux through the plant. Water status (any measure of the general state of water, (Ref. 7)) of a plant is a primary determinant of growth and development (Ref. 4). The components of water status (e.g., water potential, water content, and transpiration) can vary over periods of hours to weeks. Because of its significance to plant functioning, estimation of plant water relations parameters using remotely sensed data would be useful. Several studies have suggested the utility of optical data to determine water relations properties (Refs. 5, 8, 10). Since microwaves are sensitive to the water content of objects (Ref. 11), they may be useful for detection of short- to long-term changes in water status, while for other applications of microwaves, e.g., estimates of biomass, such changes will add to the noise in the signals.

1.2 Water relations

Water movement through the soil-plant-atmosphere continuum is affected by a variety of factors, including: soil water potential, conductances between the various compartments, and storage. The primary driving force for movement of water is evaporation from the leaves (transpiration). Water status may be measured in several ways. Water content is the easiest parameter to measure; however, it is the least reliable. Leaves are especially variable in both amount of water and dry mass. Water content can vary at full hydration from less than 70% to nearly 90% depending on species (Ref. 6). Within a species or treatment, a large number of samples are needed in order to reduce inherent variability. Relative water content (i.e., in situ water mass per water mass at full hydration) reduces the apparently stochastic variability. However, comparison among different species is questionable.

The concept of water potential (Ref. 7) is derived from steady-state thermodynamics using the chemical potential of pure water as a reference. Water potential is the sum of turgor pressure (the mechanical pressure of the cell sap on the cell wall), osmotic pressure (effect of solutes), and matrix pressure (effect of various matrices, mainly cell wall). Water potential provides a more consistent measure of plant water status and connection to plant function than water content. As transpiration increases, flow rate to the leaves increases and the amount of stored water decreases (Ref. 9). Leaf water potential responds by decreasing.

2. MATERIALS AND METHODS

Water status was measured on walnut trees growing in an experimental orchard (Kearney Agricultural Center, Fresno Co., California, USA) irrigated at 100% or 33% of potential evapotranspiration. Several parameters were measured to provide a broad picture of water status for comparison with concurrently acquired microwave and optical data.

Fresh and dry weight, water and osmotic potential of leaves were measured periodically throughout the experimental period. Single leaflets were placed in plastic bags, excess air removed and sealed. Samples were stored on ice for fresh weight determinations. Dry

Proceedings of IGARSS '88 Symposium, Edinburgh, Scotland, 13-16 Sept. 1988 (IEEE 88CH2497-6)

weight was measured after drying at 70 C for 36-48 hr. Water potential of leaflets was measured with a pressure chamber. Relative water content was determined by hydrating leaves at 0-4 C. Osmotic potential was measured using pressure-volume curves or frozen samples for thermocouple psychrometry (6). Transpiration rate and leaf conductance was measured during the day in conjunction with leaf water potential measurements. Fresh and dry weights of fruit (husks and nuts) were measured over diurnal periods. A few measurements of stem water content were taken.

Optical and microwave measurement are presented in (Refs. 1, 3). L-band dielectric probes were used to measure the dielectric constant at various positions and depths in trunks (Ref. 2).

3. RESULTS

Water content as a function of dry or fresh weight, or leaf area varied so much from leaf to leaf that no diurnal pattern was observed. On average water content per unit dry weight was lower for sun leaves than shade leaves. Relative water content of leaves was between 0.8 and 1.0 with little diurnal change. Over a two week period fruit water content declined slightly as they mature.

Unlike the other measures of water status, water potential showed very strong diurnal variation with maximum water potential of about -2 bars occurring before sunrise and the minimum of -15 to -20 bars in the early afternoon, when transpirational water loss is maximum. Osmotic pressure did not vary significantly between early morning and afternoon. Shaded leaves in the 100% irrigation treatment generally had higher water potentials than sun leaves, reflecting difference in transpiration. However, shade and sun leaves in the 33% treatment had essentially the same water potentials, probably reflecting both more open canopy and lower water availability. The minimum turgor, calculated as the difference between osmotic potential and water potential, occurs in the early afternoon, with minimum values for both irrigation treatment of 0-5 bars.

Diurnal changes in backscatter of microwaves paralleled changes in water potential (Ref. 3). Data from the dielectric probe (Ref. 2) show that the dielectric constant of the trunk (and presumably the water content) declines markedly during the day and rebounds at night.

4. DISCUSSION

The basic diurnal pattern in leaf water potential is typical of plants growing in a region of high evaporative demand (i.e., high temperature and low humidity). However, at no time did any of the trees on either 33% and 100% potential evapotranspiration treatments have water potentials less than -20 bars, although a few leaves reached this level and had wilted. These data indicate that irrigation treatment effects were manifested by altered canopy development rather than altered water transport processes. Coupling of water flow through the soil-plant-atmosphere continuum makes measurement of leaf water potential a sensitive indicator of plant water status for trees.

The most striking observation is the parallel diurnal variation of dielectric constant and water potential. Both parameters declined from dawn until early afternoon then recovered overnight. The spatial variation in dielectric constant (Ref. 2) indicates a complex process, but more information needs to be gathered to characterize the response of dielectric probes to changes in water status in tree trunks.

C-, X-, and L-bands showed diurnal changes in backscatter features that paralleled changes in water potential (Ref. 3). While it is highly unlikely that microwave backscatter is directly sensing water potential, the fact that backscatter and water potential co-vary provides a potential opportunity to monitor indirectly water potentials of canopies. However, this correlation may also introduce noise into remotely sensed microwave data unless analyses include water status models.

5. REFERENCES

1. Caldwell, W. and V. C. Vanderbilt, 1988, "Field system to determine reflectance of tree canopies," to appear in *IGARSS'88 Digest*, Edinburgh, Scotland, September 13-16, 1988.

2. Dobson, M. C., 1988, "Diurnal and seasonal variations in the microwave dielectric constant of selected trees," to appear in *IGARSS'88 Digest*, Edinburgh, Scotland, September 13-16, 1988.

3. Dobson, M. C., K. McDonald, F. T. Ulaby, and J. F. Paris, 1988, "Diurnal patterns in multi-frequency, multipolarization backscattering by a walnut orchard," to appear in *IGARSS'88 Digest*, Edinburgh, Scotland, September 13-16, 1988.

4. Bradford, K.J. and T.C. Hsiao, 1982, "Physiological Responses to Moderate Water Stress," In Lange, O.R., P.S. Nobe, C.B. Osmond, and H. Ziegler (Eds.) *Ency. Plant Phys. NS 12B. Physiological Plant Ecology II*, Springer-Verlag, pp. 264-324.

5. Hunt, E.R., Jr., B. N. Rock, and P. S. Nobel, 1987, "Measurement of leaf relative water content by infrared reflectance," *Remote Sens. Environ.*, 22: 429-435.

6. Kramer, Paul J., 1983, *Water Relations of Plants*, Academic Press, Inc., New York.

7. Passioura, J. B., 1982, "Water in the soil-plant-atmosphere continuum." In: O. L. Lange et al Eds., *Physiological Plant Ecology II. Encyclo Plant Physiol. NS*, Vol. 12 B. pp 5-33.

8. Ripple, W. J. and B. J. Schrumpt, 1987, "Remote sensing of plant water status," *Proc. Int. Conf. Measurement of Soil and Plant Water Status,* Logan, UT. July-6-10, 1987, V2: 103-109.

9. Schulze, E-D., J. Cermak, R. Matyssek, M. Penka, R. Zimmermann, F. Vasicek, W. Gries, and J. Kucera, 1985, "Canopy transpiration and water fluxes in the xylem of the trunk of Larix and Picea trees -- A comparison of xylem flow, porometer and cuvette measurements," *Oecologia,* 66: 475-483.

10. Sellers, P. J., 1985, "Canopy reflectance, photosynthesis and transpiration," *Int. J. Remote Sens,* 6: 1335-1372.

11. Ulaby, F. T., R. K. Moore, and A. K. Fung, *Microwave Remote Sensing: Active and Passive, Vol. I. -- Microwave Remote Sensing Fundamentals and Radiometery,* Addison-Wesley, Reading, MA, 1981, 456 pages.

MEASUREMENT OF TREE CANOPY ARCHITECTURE

BY

S.N. Martens and S.L. Ustin, Department of Botany, University of California, Davis, CA 95616, USA and
J.M. Norman, Department of Soil Science, University of Wisconsin, Madison, WI 53706, USA

SUBMITTED TO:

INTERNATIONAL JOURNAL OF REMOTE SENSING

ABSTRACT. The lack of accurate, extensive geometric data on tree canopies has retarded development and validation of radiative transfer models. We devised a stratified sampling method to measure the three-dimensional geometry of 16 walnut trees which received irrigation treatments of either 100% or 33% of evapotranspirational demand for the previous two years. Graphic reconstructions of the 3D geometry were verified by 58 independent measurements. The distributions of stem and leaf size classes, lengths, and angle classes were determined and used to calculate leaf area index (LAI), stem area, and biomass. Reduced irrigation trees have lower biomass of stems, leaves and fruit, lower LAI, steeper leaf angles and altered biomass allocation to large stems. These data can be used in ecological models that link canopy processes with remotely sensed measurements.

Address correspondence to: Scott N. Martens, Department of Botany, University of California, Davis, CA 95616; Phone (916) 752-2956

1. Introduction

Radiative transfer models have wide application for meteorological and ecological studies of canopy energy exchange processes and for studies of plant productivity. Improved knowledge of the geometric structure of plant canopies is essential to the further development and validation of radiative transfer models of canopy reflectance. The lack of accurate, extensive geometric data has retarded development and testing of canopy reflectance models (Vanderbilt 1985). Existing models for canopy reflectance use minimal geometric input perhaps in part because of the difficulty of obtaining necessary data (Kimes and Kirchner 1982; Norman and Welles 1983; Goel and Grier 1988).

The fundamental description of canopy geometry includes the inclination, azimuth, surface area, and location of individual plant parts. Data gathering requirements can be eased by applying some reasonable assumptions. Azimuthal angle distributions of stems and leaves can be assumed to be symmetric, which is usually the case for most non-heliotropic plant species. Further, the location of individual canopy elements can be assumed to be random, usually in a horizontal monolayer. These are reasonable assumptions for many herbaceous canopies of nearly full

cover (Norman 1979) so that the remaining parameter, inclination angle, is all that need be documented.

Further refinements are needed for canopies having widely spaced plants with non-homogeneous horizontal or vertical dispersion patterns. Agricultural examples include orchard trees with dense crowns or some widely spaced row crops such as grapes. In natural communities, individual plants may be aggregated due to microsite differences or to competitive interactions. For these complex cases, higher dimension shapes, such as ellipsoids (Norman and Welles 1983), have been used to decompose canopies into subunits. Ellipsoids may represent individual plants within the canopy or may depict a cylinder of biomass as might occur along a row of closely spaced plants. Canopy elements are usually assumed to be randomly located within ellipsoids though aggregation can be introduced if more information on the geometric structure of individual plants is available.

The location of canopy elements is obviously non-random in canopies of some large plants, e.g., trees and some shrubs, even though inclination and azimuth angles may be random. Smaller stems are completely dependent upon larger stems with respect to location. Because branching angle can be genetically fixed in a species the inclination and azimuth angles of smaller stems are also dependent on those of larger stems to some degree. Leaves, in turn, are usually

attached only to the smaller stems and are dependent on them for location. However, because of phyllotaxy or twisting of petioles among other reasons, leaf angular distributions can be relatively independent of the stem angular distributions (Fisher 1986). Because of these location dependencies statistical sampling of canopy geometry for extrapolation to the stand or field level can be difficult.

1.B. Geometric assumptions of canopy radiation transfer models

A considerable literature on canopy radiation transfer models exists and several reviews are available (e.g., Ross 1981; Goel 1988). An early use of a one-dimensional canopy radiation model was made by de Wit (1965) to estimate canopy photosynthesis. His model, based on work by Monsi and Saeki (1953), assumed a canopy of randomly positioned foliage elements. Several studies have shown that canopy photosynthesis or carbon gain can be estimated from knowledge of the photosynthetically active radiation (PAR) intercepted by a canopy (Monteith 1981; Jarvis and Leverenz 1983; Linder 1986; Russell et al. 1989). Much literature now exists on this type of one-dimensional model for predicting light penetration in vegetation and for its use in estimating canopy photosynthesis (Lemeur and Blad 1974; Norman 1975; Ross 1981; Sellers 1985, 1987).

The simplest one-dimensional models of radiative exchange in vegetation canopies, e.g. Verhoef (1984), assume that leaves are randomly located Lambertian scatterers, symmetrically distributed about the azimuth and inclined to the horizontal with some reasonable distribution. The essential information required for input to such models is leaf spectral properties, leaf area index (LAI), and leaf inclination distribution (LID). The LAI can be measured by a number of direct and indirect techniques (Norman and Campbell 1988). The LID can be characterized by a two-parameter beta distribution (Goel and Strebel 1984) or a single parameter ellipsoidal distribution (Campbell 1986).

Suits (1972) one-dimensional model, which assumed random leaf positioning, a symmetric azimuthal distribution and leaves inclined in only vertical or horizontal directions, was the first to predict canopy bidirectional reflectance. Verhoef (1984) generalized Suits (1972) approach to include any leaf inclination distribution with azimuthal symmetry. Several newer models have been proposed that are based on Lambertian leaf spectral properties, random leaf positioning, azimuthal symmetry, and any leaf inclination angle distributions (e.g. Cooper et al. 1982; Camillo 1987; Choudhury 1987). Hapke (1984) published a similar model for soil surfaces. Norman et al. (1985) describe a numerical model of canopy bidirectional reflectance similar in assumptions but which specifically considers the soil

bidirectional reflectance and non-Lambertian leaf characteristics.

A slight variation on the random-leaf-positioning concept was proposed by Nilson (1971) to accommodate clumping or regular-leaf-spacing tendencies with empirical coefficients. However, obtaining the necessary empirical coefficients depends more on fitting the modified quasi-random model to radiation penetration measurements than on appropriate canopy structural measurements. A different concept of clumping was proposed by Norman and Jarvis (1975) for spruce trees, and the radiation penetration model was linked to measurements of projected needle area of shoots and the organization of shoots onto branches, with the model including the woody portions of the canopy. This might be referred to as a weighted-random approach. Other clumping models have been proposed for predicting light penetration in agricultural crops and some are reviewed in Norman (1974).

Models that incorporate clumping require some measurements of the horizontal distribution of foliage and these are difficult to obtain. The three-dimensional radiation penetration model of Norman and Welles (1983), which is similar to the models of Whitfield and Conners (1981) and Welles (1976), has attempted to simplify the measurement input requirements by requiring only the dimensions of an

ellipsoidal envelope within which all the leaves are contained and assumed randomly distributed. Thus, for these envelope models, the only additional measurements beyond those required for a one-dimensional model are the overall crown dimensions of individual trees. The light penetration model of Norman and Welles (1983) has been recently extended to include the canopy bidirectional reflectance distribution function (BRDF) by Welles (1988).

Incorporating the three-dimensional structure of the canopy into radiation models permits closer approximation of the complexity of real canopies. The model of Kimes and Kirchner (1982), which considers the general three-dimensional distribution of elements requires even more detailed spatial data on the distribution of canopy elements than envelope models. This is also true for the model of Wang (1988).

The most general three-dimensional canopy radiative transfer models are based on ray tracing (Myneni et al. 1987) and Monte Carlo techniques (Ross and Marshak 1985). An additional general method termed radiosity has been used in graphics applications (Greenberg 1986) but no published literature is yet available for its application in canopy studies. In principle, these radiative transfer approaches can accommodate almost any architecture. The Monte Carlo model of Ross and Marshak (1985, 1988) is a good example of

a model capable of predicting the canopy BRDF, including the "hot spot", for generalized canopy architectural descriptions even though they considered a random canopy. The latter model inputs considerable canopy structural information, including the number of leaves per canopy and the distance between leaves -- information which is not generally available.

The greatest obstacle to the application of three-dimensional radiative transfer models is that suitable canopy architectural information is scarce because of the difficulty in obtaining such measurements. Although recent advances in L-systems (Lindenmayer 1987) and fractal geometry (Mandelbrot 1982) can provide quantitative tools for representing some vegetation structures, detailed structural characteristics such as branching patterns, leaf size, leaf shape, and the distribution of flowers and fruits must still be measured directly.

The study described in this paper provides the essential information required to fully characterize a three-dimensional canopy with L-systems or fractals, but that task will be the subject of another paper. Here we describe the methodology for obtaining the essential information and summarize the results of the fundamental distribution of canopy elements from row-spaced trees with complex crown architecture. The canopy geometry of walnut trees which had

received irrigation treatments of 100% and 33% of calculated evapotranspiration for two years was measured. The angular and spatial distributions of stems were sampled in such a manner as to readily allow a verifiable three-dimensional reconstruction of the canopy stem components. Combined with other data (e.g., leaf angular distributions, tallies of branches, leaves, and fruits, wood and leaf specific weights) we can provide estimates of important canopy architectural characteristics such as leaf area index and biomass.

2. Methods

2.A. Description of Study Site

The walnut orchard is at the University of California Kearney Agricultural Center, Parlier, CA, USA (36.60° N 119.50° W). The trees (Juglans regia cv. 'Chico') were 6 years old at the time of sampling in August 1987. Tree spacing is nominally 6.7m across and 3.35m along the north - south oriented rows. Average maximum height of the crown outline was 4.8 m (n=24). Treatment blocks of 8 trees (2 rows by 4 trees) are surrounded by one row of border trees which receive the same irrigation treatment. Irrigation treatments of 33%, 66% (not sampled in our study) and 100% of calculated evapotranspirational use have been applied since 1986 (Goldhamer et al. 1988). Pruning is of the

"hedgerow" type where alternate row-facing sides of the trees are pruned each year. There is also pruning of some excessively heavy upper canopy branches as well as branches in the lower (< 1m) canopy. Walnut trees have a long-shoot/short-shoot morphology. The short shoots ("spurs"), which are usually less than 1 cm diameter, frequently occur at more or less uniform intervals along the long-shoots. Leaves and fruits occur at the apices of these short-shoots or at dominant terminal apices on larger shoots.

2.B. Sampling Rationale

For the purpose of relating the geometry data set to spectral data we need to make inferences about the population of leaves and stems and their angular and spatial distribution in the orchard. The obvious natural sampling unit, the tree, is not appropriate because sampling a tree would undersample the least frequent components (e.g. large stems, which are few per tree, but many per orchard) and oversample the most abundant canopy components (i.e. small stems and leaves). By regarding the orchard as several populations of canopy components (i.e. stems in 5 diameter size classes, leaves, fruits), we could sample each with the appropriate sampling effort. However, the spatial and angular dependencies among canopy components complicates this simple stratified population scheme. Sampling to reveal the dependencies (e.g. location, branching angles)

among the populations, however, must be done on a natural unit, the tree. Therefore, we applied the stratified sampling scheme at the scale of orchard, tree, and branch levels to yield a data set which can be synthesized to provide angular distributions and spatial locations of the canopy components at the orchard level.

2.C. Sampling Methods

2.C.1. Stems

Stem segments were divided into 5 size classes based on diameter at the midpoint along the length: Class 1, <= 1.0 cm; Class 2, 1.1 to 2.0 cm; Class 3, 2.1 to 3.0 cm; Class 4, 3.1 to 4.0 cm; Class 5, > 4.0 cm.

Stems were sampled as segments. A segment (the definition of which differs slightly depending on the sampling level) was a section of stem, uniform along its length in azimuth and elevation angle, which is terminated by either 1) a break in zenith angle, 2) a break in azimuth angle, 3) an apex, or 4) branching into a stem of diameter equal to or less than the critical size class. The critical size class stem depended upon the stratified sampling level as described below.

For each segment we measured length, diameter, zenith angle (from vertical), and azimuth. Figure 1 presents a diagram of the stem and leaf angles measured. Lengths were measured to the nearest cm. Zenith angle (θb, Figure 1A) was measured by placing a draftsmen's protractor with a plumb-bob along the segment. Zenith angle is the angle between a vertical line and the line the branch segment forms when its' base intersects the vertical line. A branch pointing straight up would have a zenith of 0°; horizontally, 90°; straight down, 180°. Zenith angles were translated to elevation angles (0° = horizontal; 90° = vertical) for use in the beta distribution calculations described below. Azimuth angles (θ_α, Figure 1A) were measured with a magnetic compass and later corrected to true north, or estimated with the protractor (using the true north - south row direction for orientation) where accurate magnetic readings were precluded. All angles were recorded to the nearest 5°.

Data for each segment were stored in a doubly-linked list, i.e. the segment number from which the current segment came was recorded as well as the numbers of the segments into which the current segment branched. A doubly-linked list was used, even though a singly-linked list would suffice, to safeguard against errors which would break the linkage. This data structure allowed us to examine the relations among the segments and permitted the three-dimensional reconstruction of the data set.

2.C.1.a. Orchard-level Sampling

Eight trees, in a 2 tree by 4 tree block, were sampled for each irrigation treatment (33% ET and 100% ET). For the orchard-level sampling, the critical size class was Class 4, so that only segments greater than 4 cm diameter (229 in all) were measured on all sixteen trees. All segments greater than 4 cm diameter are referred to collectively as Class 5 segments. All segments of size Classes 1 through 4 which branched directly from the Class 5 segments were tallied. There were no leaves or fruits directly attached to any of the Class 5 segments.

2.C.1.b. Tree-level Sampling

Two trees in each of the two irrigation treatments were sampled. Each Class 3 or Class 4 segment tallied in the orchard-level sampling was measured down to and including Class 2 segments. Here, the critical size class was Class 1, so no Class 1 segments were measured on these Class 3 or Class 4 segments except when 1) a Class 1 segment terminated a long-shoot or 2) was greater than 25 cm in length (a "sucker" shoot). A total of 553 segments were measured. The number of Class 1 segments occurring on each segment measured were tallied. The number of leaves and fruits on the Class 1 segments measured were tallied. Notice that

this sampling scheme does not include Class 2 segments which branch directly from Class 5 segments. A relatively small number of these branches exist. Most of these Class 2 segments were located in the interior of the canopy and, for the purposes of calculations described below, are estimated to be the equivalent of three Class 1 branches.

2.C.1.c. Branch-level Sampling

Five branches, each on a different tree, were sampled down to and including all Class 1 segments. The diameters of the basal segment of these branches were 1.9, 1.9, 2.0, 2.0, and 3.4 cm. They included upper, lower, east- and west-side canopy positions. All leaves and fruits occurring on Class 1 segments were tallied. Of the 256 segments sampled, 126 were Class 1 segments which contained 378 leaves and 209 fruits. These data are used here primarily for establishing leaf and fruit numbers per Class 1 branch for extrapolations to the whole tree level.

2.C.2. Leaves

The odd-pinnate compound leaves show a bilateral symmetry about a plane along the rachis such that the elevation angle of the lateral leaflets from this plane is about the same on both sides. The leaflets also show a similar symmetry of laminar folding about the midrib of the leaflet (Figure 1C).

We measured 147 leaves on 20 vertical transects of 8 trees in the 100% ET treatment and 72 leaves on 10 vertical transects of 6 trees in the 33% ET treatment. The transect locations were randomly selected below the canopy and the leaf nearest the vertical transect at 0.5 m intervals from the ground was measured. Measurements were made to fully describe the leaf in three-dimensions. For each leaf we measured the height, number of leaflets, the length of the petiole plus rachis, and the zenith (θ_r) and azimuth (θ_a) of the rachis (Figure 1A). The terminal and lateral leaflets were obviously different in several respects so we measured the terminal leaflet and the adjacent left-lateral leaflet for the following: midrib zenith (θ_l) and azimuth angles, the azimuth of the normal to the leaflet lamina (or the zenith angle of the normal if necessary), and the width at the widest part of the leaflet lamina when naturally folded and when flattened with the ruler. The last two measurements allowed calculation of the folding angle of the leaflet lamina about the leaflet midrib (θ_m, Figure 1C).

2.C.3. Biomass measurement

Stem volumes for 110 stem segments were determined by displacement of water and subsequently divided by the stem dry weight to determine the wood density for stems in size

classes 1 through 3. Stems in Classes 4 and 5 were assumed to have the same density as those in Class 3.

The dry weight of 100 fruits in the 33% ET treatment and 80 fruits in the 100% ET treatment was measured.

Both dry weight and leaf area (LICOR LI-3000 Leaf Area Meter) were measured on each of 50 freshly excised leaves to determine leaf specific weight.

Leaf area was measured for each leaflet on 100 leaves from each irrigation treatment. These data were used in the calculation of the area-weighted average of leaf zenith angles.

2.C.4. Plumb line Measurements

To verify the three-dimensional reconstruction based on the angle and length measurements for stems we hung plumb lines at identified points in each of the trees sampled for tree-level measurements. The measured vertical height and distance from the trunk of each of the 58 plumb lines were compared with calculated values from the reconstruction.

3. Results and Discussion

3.A. Orchard and Tree Reconstructions

To visualize the degree of sampling at the orchard- and tree-levels, diagrammatic representations of the canopy reconstructions are presented in Figure 2. The two irrigation treatment blocks of 8 trees each are shown in realistic proximity to one another. The 4 trees sampled at tree-level are shown with the applicable level of detail, which includes all measured branches down to Class 2 size and some Class 1 branches. The other trees are represented by a reconstruction of all segments greater than 4 cm diameter (Class 5 branches). Figure 3 illustrates the tree-level sampling using data for tree R3T09 from the 100% ET treatment. The line segments are color coded with respect to diameter size class. The figures demonstrate the realistic reconstruction of this orchard and how the complex spatial structure is retained in the data set. Once verified, this data set will be useful for evaluating spatial distributions of canopy components and for validating model predictions of canopy properties based on remotely sensed optical and microwave data.

The three-dimensional reconstructions are subject to cumulative positional errors. These errors could be a function of the number of preceding segments (greater chance for errors) or a function of the length of the preceding segments (incorrect projection of segments due to errors in angle measurements). To evaluate the fidelity of the three-

dimensional reconstructions we compared the calculated positions in space of 58 points on the 4 trees used in the tree-level sampling with independent measurements of location determined by plumb lines. There is close agreement between the two data sets for both vertical height (Figure 4) and horizontal distance from the trunk (Figure 5). The regression equation in each case is highly significant ($p < .001$). Intercepts are not significantly different from 0 and slopes are not significantly different from 1.0 (standard error of slope for each regression is 0.025). Examination of residuals shows no deviation from the linear model.

Close inspection of the statistical patterns provides further support for the validity of the reconstructions. Correlations of residuals from regressions in Figures 2 and 3 to the number of preceding segments, or their summed length were significant only for distance residuals versus number of preceding segments ($r = 0.474$, $p = .001$). However, when the number of preceding segments was included as a term in the regression model for distance the R^2 increased only slightly from 0.9773 to 0.9801. Thus, the accumulation of measurement errors, leading to large deviations from the expected measurements in height or distance, was not found to be significant in the data set. Hence, this data set can be used with some confidence for

parameters which depend on the three-dimensional location of canopy components.

3.B. Stem Size Classes

The stem length distributions of stem diameter sizes is presented for the orchard-level (Figure 6) and tree-level (Figure 7) sampling. The orchard-level data is the summed length of stems of each diameter size class for the 8 trees in each treatment. Summed length of stems was used because the number of segments (stems) measured is an artifactual value due to the manner in which segments were defined and sampled. Smaller diameter stems are more frequent overall but there is a rise in frequency in the 13 to 16 cm size classes which corresponds to the sizes of most of the trunks on the trees. The largest stem diameters (17 cm and 18 cm classes) are exclusively among the 100% ET treatment trees while the largest stem diameters in the 33% ET treatments are 13 cm to 16 cm. Similarly, stem size categories from 5 cm to 10 cm have greater length in the 100% ET treatment than the 33% ET treatment (Figure 6). T-tests between the treatments for each size class category indicate a significant difference for only the 7 cm class ($t = 2.2681$, $p < .04$). However, the total length of stems $\geq$ 4 cm diameter per tree is significantly less in the 33% ET treatment ($t = 2.8353$, $p < .02$). The difference could result from reduced allocation of photosynthate to the growth of large stems

during the two seasons of reduced irrigation. The observation that the largest diameter stems are in the 100% ET treatment is consistent with this idea. The 100% ET treatment also has a greater calculated biomass of Class 5 stems ($\bar{x}$ = 26.63 kg/tree) than the 33% ET treatment ($\bar{x}$ = 20.44 kg/tree; $t = 2.265$, $p < .04$).

The stem length distributions for the tree-level sampling (Figure 7) are expressed for the two irrigation treatments (two trees per treatment). The data for Class 1 and Class 2 stems includes extrapolated values for the tallied Class 1 and Class 2 stems which occurred on the Class 5 stems. Extrapolations were based on the following assumptions. A mean Class 1 branch length of 6.72 cm (calculated from the branch-level sampling) was assumed for the tallied Class 1 branches. A further assumption was made for the Class 2 segments tallied on Class 5 segments. These small branches are mostly in the interior of the canopy. Examination of branch-level data most similar to them indicates that the Class 2 branches are equivalent in length to 3 to 6 Class 1 segments. We assumed for our calculations that one Class 2 branch is equivalent to three Class 1 segments. An assumption at the upper extreme of 6 Class 1 segments per Class 2 would increase the summed length of Class 2 segments by 9.0% in the 100% ET treatment and 6.4% in the 33% ET treatment. The summed length of all stem size classes would increase 2.9% in the 100% ET treatment and 2.1% in the 33%

ET treatment. Thus, the worst case error indicates the assumptions provide reasonable values for further modelling.

The results (Figure 7) for the two irrigation treatments are very similar for each size class category and similar in the summed length of all stem size classes (27.5 m and 27.0 m in the 100% and 33% ET treatments respectively). This pattern is consistent with the maintenance of the carbon allocation to smaller stems under water-stress and contrasts with the observed pattern of reduced allocation to larger stems.

3.C. Stem Angle Distributions

The azimuthal distribution of stems of Classes 2 through 5 for both treatments is presented in Figure 8. The distribution of each size class is uniform with respect to azimuth. The smallest size class, Class 2, appears to have an increased frequency in the north to northeast quadrant ($X^2 = 12.68$, $p < .01$). The relatively symmetric azimuthal distribution of stems we found, while expected for open-grown trees, might not be expected in this situation where the trees are grown with compact spacing along the rows (north - south) and receive hedgerow pruning on alternate sides (east - west) every year.

The zenith angle of the 4 stem size classes for both treatments is shown in Figure 9. Stem zenith angles range

from 0° (vertical) to 90° (horizontal) to 180° (stem pointing downward). Our definition of zenith angle for stems differs from the conventional because the angle is expressed in reference to the origin of the stem and therefore extends over a 180° arc. There is a clear trend for larger stems to be more upright as shown by the rapid rise of the curve for the Class 5 (> 4.0 cm diameter) branches in the 0° to 90° region. In contrast, the Class 2 stems are nearly uniformly distributed throughout the 180° range.

3.D. Leaf Angle Distributions

The azimuthal angle distribution of lateral and terminal leaflet types by irrigation treatment is presented in Figure 10. All four leaflet types appear to be uniformly distributed with respect to azimuth.

The zenith angles of the four leaflet types are shown in Figure 11. Zenith angles are expressed relative to the origin of the petiole and the top surface of the leaf. Leaf zenith angles may exceed 180° in cases of extreme petiole twisting. Terminal leaflets are more steeply angled than lateral leaflets within a treatment. The mean angles for the 100% ET leaves are 151.4° and 131.0°, terminal and lateral leaflets respectively; 156.4° and 139.8° for the 33% ET treatment. The leaflets of the 100% treatment are more horizontal than the same type of leaflet in the 33%

treatment as shown by the shift to lower zenith angles in Figure 11 for the 100% ET treatment leaflets.

The area-weighted average leaflet zenith angle was calculated for each treatment. The 100% ET treatment leaves have 6.77 leaflets per leaf and the 33% ET treatment leaves have 6.49 leaflets per leaf. Average terminal leaflet area is 83.0 and 77.8 cm^2, lateral leaflet area is 36.3 and 36.2 cm^2, for 100% and 33% ET treatments. Therefore, the area-weighted average leaflet angle for the 100% ET treatment is 136.8° from vertical and is 144.5° for the 33% ET treatment.

3.E. Beta Distributions of Elevation Angles

The angular distributions of the canopy components can also be expressed using the beta distribution (Goel and Strebel 1984). The two parameters of the beta distribution, mu and nu, can be calculated from the mean and variance of the leaf and stem elevation angle distributions, and together can be used to characterize distributions relative to ideal types (de Wit 1965; Ross 1981). Zenith angles were translated to the 0° (horizontal) to 90° (vertical) quadrant for these calculations and are referred to as elevation angles. All angles referred to concerning the beta distributions are relative to this expression of zenith angles.

The beta distribution parameters for the five size classes of branches are plotted in Figure 12 for each treatment. The smallest diameter branches in both treatments show a uniform distribution tending slightly towards planophilic (most angles horizontal). With increasing diameter the distribution shifts past uniform toward spherical or spherical - erectophilic (most angles vertical). Branches of Classes 3 and 4 in the 33% ET treatment tend to be more towards plagiotropic (most angles about 45°) than the corresponding 100% ET treatment branches. Class 5 branches of both treatments tend toward the erectophilic distribution but the 33% ET branches show a lower variance.

Leaflet angle beta distributions are plotted in Figure 13. Terminal leaflets in both treatments have an approximately spherical distribution of elevation angles. The distribution of lateral leaflets differs between the treatments. The 33% ET lateral leaflets have a plagiotropic distribution. The 100% ET lateral leaflets have a distribution between uniform and plagiotropic due to a greater variance ($\bar{x}$ = 41.0°, s^2 = 381.2) than the 33% ET lateral leaflets ($\bar{x}$ = 48.7°, s^2 = 259.8). The tendency for the 33% ET leaflets to be more erect than the 100% ET leaflets is indicated by their position more towards the erectophile point than the uniform - plagiotropic line.

3.F. Leaf Geometry Changes with Height

Several parameters of leaf geometry were noted to vary with height in the canopy (Table 1). The leaflet folding angle describes the folding of the lamina about the midrib (Figure 1C). Leaflet folding angles decreased with height in the canopy for all four leaflet types indicating increased folding. The folding angle was more pronounced for terminal leaflets (146.8° and 148.4°) than for lateral leaflets (156.3° and 160.1°, 100% ET and 33% ET treatments respectively) when averaged over all heights. Folding angles differed significantly between leaflet types (t-tests, $p \leq .002$) within the same treatment but neither leaflet type differed significantly between treatments (t-tests, $p \geq .24$).

The zenith angle of the leaflet midrib showed a significant increase with height for lateral leaflets in both treatments but only weakly for terminal leaflets in the 100% ET treatment. The zenith angle of the rachis, to which the leaflets are attached, is significantly negatively correlated with height only in the 33% ET treatment. The angle becomes more horizontal toward the top of the canopy.

The width of the terminal leaflets is negatively correlated with height for both treatments. Lateral leaflets show a significant negative correlation with height only in the

100% ET treatment. The number of leaflets per leaf significantly increases with height in both treatments

Despite the statistically significant correlations of some leaf geometry parameters with height it is important to note that the R^2 values are generally low and the slopes are often small.

3.G. Tree Descriptors

A number of descriptors for each of the four trees sampled in the tree-level sampling are presented in Table 2. We assumed that each tallied Class 2 branch, as we did for length (see 3B above), was equivalent to three Class 1 branches with respect to weight, area and numbers of fruits and leaves. If the assumption of 6 Class 1 branches per tallied Class 2 branch were used instead (see 3B above) the range of percent increase in the values would be as follows: branch biomass, .28% to .37%; branch area, .70% to 1.05%; leaf area and biomass, 4.81% to 6.68%; nut mass, 5.13% to 8.77%. The 100% ET trees (R2T09 and R3T09) show greater increases within the ranges given because they have more tallied Class 2 segments than the 33% ET treatment trees (R2T14 and R3T17). The same leaf specific weight (7.409 mg per cm^2) was used for calculations for both irrigation treatments. Wood density was measured as 347.2, 388.6, 447.6, and 449.6 mg/cm^3 for stems of Classes 1 through 4.

Class 5 stems were assumed to have the same wood density as Class 4 stems. Individual fruit weight was 11.10 g and 8.29 g for the 100% ET and 33% ET treatments respectively. Leaf area per leaf was measured at 297.04 cm^2 in the 100% ET treatment and 285.43 cm^2 for the 33% ET treatment.

The average height of the 100% ET trees is greater than for the 33% ET trees but there is near overlap in values. However, the maximum height of the Class 5 branches shows significant separation of the two types with the 100% ET trees taller than the 33% ET trees. This is consistent with the results for Class 5 segments on all 16 trees measured at the orchard-level where the 100% ET trees have a maximum height of 411 cm which is significantly greater than the 335 cm height of the 33% ET trees ($t = 5.245$, $p = 0.0001$). The 33% ET trees may reach maximum heights as great as the 100% ET trees but have fewer large diameter branches in the upper canopy. The reduced irrigation treatment appears to have decreased radial growth of stems more than extension growth.

The total biomass of the 100% ET trees is greater than the 33% ET trees which are about 86% of the biomass of the 100% ET trees. The apportionment of biomass among organs, however, seems to be about the same between the treatments except for fruits. Notably, the 33% ET trees are 89% of the stem weight and 94% of the leaf weight, but they have only 76% of the fruit weight of the 100% ET trees.

Stem areas were calculated as the summation of length times diameter for all stems. Stem areas and leaf areas are greater for the 100% ET trees. LAI (m^2 leaf area per m^2 ground area) averages 3.40 for the two 100% ET trees and 3.18 for the two 33% ET trees presented in Table 2. However, projected LAI exhibits a greater difference between the treatments due to the steeper leaflet angles of the 33% ET trees. The number of sucker shoots is greater on the 100% ET trees (7 and 9 shoots) compared to the 33% ET trees (0 and 4 shoots) which contributes to the dissimilar appearances of the trees in the field. The projected surface outline of the upper tree canopy is the primary visual difference between the treatments and leads to this perception.

4. Future Work

The potential exists for deriving more detailed descriptions of some canopy components from this data set. In addition, the synthesis of the stem and leaf data into a three-dimensional representation of the orchard canopy would provide an unparalleled data set for radiation transfer model development and validation. Because of the high level of detail supplied it may also aid in clarifying the degree of abstraction permissible in models before physical fidelity is lost. Specifically, the assumption of random

versus clumped distributions of canopy elements in sub-canopy volumes, an area much in need of further research (Goel and Grier, 1988), can be addressed. Further, the data set could be used in models of canopy growth, development, or physiology (e.g. Caldwell et al. 1988; Myneni et al. 1989; Sellers 1985, 1987) and so can support the link between canopy processes and remote sensing.

5. Conclusion

The sampling procedure we used allowed us to collect detailed data on many aspects of canopy components and faithfully, and verifiably, represent those components in three-dimensional space. Some of the basic data needed for input into models of canopy reflectance are presented. The three-dimensional geometry was reconstructed for each of the 16 trees measured for all branch segments with diameter greater than 4 cm, and in 4 trees, all branch segments having diameters greater than 2 cm. Branch and leaf size classes, lengths and angle class distributions were presented for two irrigation treatments, one receiving 100% of potential evapotranspiration and the other receiving 33% evapotranspiration for two years prior to measurement. These data were used with specific weights to determine the distributions of canopy biomass. The beta distributions were determined for each irrigation treatment.

Our data set provides a good picture of the consequences of two years reduced irrigation on walnut tree morphology: less biomass of stems, fruits and leaves, lower LAI, less allocation to large stems, fewer sucker shoots, and more vertically inclined leaf angles. These data can be used to test and validate canopy photosynthesis and carbon gain models.

6. Acknowledgements

We wish to thank the University of California Kearney Agricultural Center for their assistance and cooperation during this experiment, and to Dr. David Goldhamer for the use of his experimental orchard. We wish to thank Narinder Chauhan, Peter Collins, Jatinder Singh, Curtis Smith, and Erik Ustin for field assistance. This research was supported under NASA grant NAGW1101 subcontract from the University of Michigan (#204272).

7. References

Caldwell, M.M., Meister, H.-P., Tenhunen, J.D., and Lange, O.L., 1986, Canopy structure, light microclimate and leaf gas exchange of Quercus coccifera L. in a Portuguese macchia: measurements in different canopy

layers and simulations with a canopy model. Trees, 1, 25-41.

Campbell, G.S., 1986, Extinction coefficients for radiation in plant canopies calculated using ellipsoidal inclination angle distribution. Agricultural and Forest Meteorology, 36, 317-321.

Campbell, G.S., and Norman, J.M., 1989, The description and measurement of plant canopy structure. In Plant Canopies: Their Growth, Form, and Function, edited by G. Russell, B. Marshall, and P.G. Jarvis. (New York: Cambridge University Press, Society for Experimental Biology, Series 31).

Camillo, P., 1987, A canopy reflectance model based on an analytical solution to the multiple scattering equation. Remote Sensing of Environment, 23, 453-477.

Choudhury, B.J., 1987, Relationships between vegetation indices, radiation absorption and net photosynthesis evaluated by a sensitivity analysis. Remote Sensing of Environment, 22, 209-233.

Cooper, K., Smith, J.A., and Pitts, D., 1982, Reflectance of vegetation canopies using the adding method. Applied Optics, 21, 4112-4117.

de Wit, C.T., 1965, Photosynthesis of Leaf Canopies. Agricultural Research Report, 663. (Wageningen: Centre for Agric. Pub. and Doc.).

Fisher, J.B., 1986, Branching patterns and angles in trees. In On the Economy of Plant Form and Function, edited by T.J. Givnish (Cambridge: Cambridge University Press).

Goel, N.S., 1988, Models of vegetation canopy reflectance and their use in estimation of biophysical parameters from reflectance data. Remote Sensing Reviews, 4, 1-212.

Goel, N.S., and Strebel, D.E., 1984, Simple beta distribution representation of leaf orientation in vegetation canopies. Agronomy Journal, 76, 800-802.

Goel, N.S., and Grier, T., 1988, Estimation of canopy parameters for inhomogeneous vegetation canopies from reflectance data. III. TRIM: A model for radiative transfer in heterogeneous three-dimensional canopies. Remote Sensing of Environment, 25, 255-293.

Goldhamer, D.A., Beede, R., Sibbett, S., DeJong, T.M., Ramos, D., Phene, R.C., and Doyle, J., 1988, Third

year effects of deficit irrigation on walnut tree performance. Walnut Research Reports. Walnut Marketing Board, Sacramento, CA. pp. 42-52.

Greenberg, D.P., Cohen, M.F., and Torrance, K.E., 1986, Radiosity: A method for computing global illumination. The Visual Computer, 2, 291-297.

Hapke, B., 1984, Bidirectional reflectance spectroscopy. 3. Correction for macroscopic roughness. Icarus, 59, 41-59.

Jarvis, P.G., and Leverenz, J.W., 1983, Productivity of temperate deciduous and evergreen forests. In Encyclopedia of Plant Physiology, Physiological Plant Ecology IV, NS. Ecosystem Processes: Mineral Cycling. Productivity and Man's Influence, edited by O.L. Lange, P.S. Nobel, C.B. Osmond, and H. Ziegler (New York: Springer Verlag).

Kimes, D.S., and Kirchner, J.A., 1982, Radiative transfer model for heterogeneous 3D scenes. Applied Optics, 21, 4119-4129.

Lemeur, R., and Blad, B.L., 1974, A critical review of light models for estimating the shortwave radiation

regime of plant canopies. Agricultural Meteorology, 14, 255-286.

Lindenmayer, A., 1987, Models for multicellular development: characterization, inference and complexity in L-systems. In Trends, Techniques and Problems in Theoretical Computer Science. Lecture Notes in Computer Science 281, edited by A. Kelmenova and J. Kelmer (Berlin, Springer-Verlag).

Linder, S., 1986, Potential and actual production in Australian forest stands. In Research for Forest Management, edited by J.J. Landsberg, and W. Parsons (Melbourne, Australia: CSIRO).

Mandelbrot, B.B., 1982, The Fractal Geometry of Nature (New York: W.H. Freeman and Co.)

Monsi, M. and Saeki, T., 1953, Uber den lichtfaktor in den Pflanzengesellschaften und seine Bedeutung fur die Stoffproduktion. Japanese Journal of Botany, 14, 22-52.

Monteith, J.L., 1981, Does light limit crop production? In Physiological Processes Limiting Plant Productivity, edited by C.B. Johnson (London: Butterworths).

Myneni, R.B., Asrar, G. and Kanemasu, E.T., 1987, Light scattering in plant canopies: The method of successive orders of scattering approximations (SOSA). Agricultural and Forest Meteorology, 39, 1-12.

Myneni, R.B., Ross, J. and Asrar, G., 1989, A review on the theory of photon transport in leaf canopies. Agricultural and Forest Meteorology, 45, 1-153.

Nilson, T., 1971, A theoretical analysis of the frequency of gaps in plant stands. Agricultural Meteorology, 8, 25-38.

Norman, J.M., 1975, Radiative transfer in vegetation. In Heat and Mass Transfer in the Biosphere, edited by D.A. deVries and N.H. Afgan (Washington, D.C.: Scripta Book Co.).

Norman, J.M., 1979, Modeling the complete crop canopy. In Modification of the Aerial Environment of Plants, edited by B.J. Barfield and J.F. Gerber (St. Joseph: Amer. Soc. Agric. Eng. No. 2).

Norman, J.M., and Campbell, G.S., 1989, Canopy Structure. In Plant Physiological Ecology: Field Methods and Instrumentation, edited by R.W. Pearcy, J.R.

Ehleringer, H.A. Mooney and P.W. Rundel (London, New York: Chapman and Hall).

Norman, J.M., and Jarvis, P.G., 1975, Photosynthesis in Sitka spruce (Picea sitchensis (Bong.) Carr.). V. Radiation penetration theory and a test case. Journal of Applied Ecology, 12, 839-878.

Norman, J.M., and Welles, J.M., 1983, Radiative transfer in an array of canopies. Agronomy Journal, 75, 481-488.

Norman, J.M., Welles, J.M., and Walter, E.A., 1985, Contrasts among bidirectional reflectance of leaves, canopies and soils. IEEE Transactions in Geoscience and Remote Sensing, GE-23, 659-667.

Ross, J., 1981, The Radiation Regime and Architecture of Plant Stands (The Hague: W. Junk, Publishers).

Ross, J., and Marshak, A.L., 1985, A Monte Carlo procedure for calculating the scattering of solar radiation by plant canopies. Soviet Journal of Remote Sensing, (English translation), 4, 783-801.

Ross, J., and Marshak, A.L., 1988, Calculation of the canopy bidirectional reflectance using the Monte Carlo method. Remote Sensing of Environment, 24, 213-225.

Russell, G., Jarvis, P.G., and Monteith, J.L., 1989, Absorption of radiation by canopies and stand growth. In Plant Canopies: Their Growth, Form and Function, edited by G. Russell, B. Marshall and P.G. Jarvis (New York: Cambridge University Press, Society for Experimental Biology, Series 31).

Sellers, P.J., 1985, Canopy reflectance, photosynthesis and transpiration. International Journal of Remote Sensing, 6, 1335-1372.

Sellers, P.J., 1987, Canopy reflectance, photosynthesis and transpiration. II. The role of biophysics in the linearity of their interdependence. Remote Sensing of Environment, 21, 143-183.

Suits, G.H., 1972, The calculation of the directional reflectance of a vegetative canopy. Remote Sensing of Environment, 2, 117-125.

Vanderbilt, V.C., 1985, Measuring Plant Canopy Structure. Remote Sensing of Environment, 18, 281-294.

Verhoef, W., 1984, Light scattering by leaf layers with application to canopy reflectance modeling: The SAIL model. Remote Sensing of Environment, 16, 125-141.

Wang, L-P., 1988, Crown structure, radiation absorption, photosynthesis and transpiration. (University of Edinborough: Ph.D. Dissertation), 188 p.

Welles, J.M., 1978, A model of foliage temperatures for a heated orchard. (Pennsylvania State University: M.S. Thesis), 88 p.

Welles, J.M., 1988, A Bidirectional Reflectance model for non-random canopies. (University of Nebraska: Ph.D. Dissertation), 121 p.

Whitfield, D.M., and Conners, D.J., 1980, Penetration of photosynthetically active radiation into tobacco crops. Australian Journal of Plant Physiology, 7, 449-461.

Table 1. Regressions of leaf geometry variables versus height (m) in the canopy.

Irrigation Treatment	100% ET			33% ET		
Variable	Intcp	Slope	R^2	Intcp	Slope	R^2
Terminal Lflt Folding Angle	174.60	-10.6	.2013***	168.55	-7.76	.1306**
Lateral Lflt Folding Angle	170.47	-5.42	.0671**	181.63	-8.32	.1785***
Terminal Midrib Zenith Angle	143.04	3.18	.0269*	154.66	0.70	.0023
Lateral Midrib Zenith Angle	112.15	6.66	.0900***	125.23	5.64	.1436**
Rachis Zenith Angle	137.46	-1.94	.0059	154.14	-7.95	.0980**
Terminal Lflt Width (cm)	8.27	-0.59	.1910***	7.94	-0.38	.0809*
Lateral Lflt Width (cm)	5.33	-0.19	.0581**	5.37	-0.13	.0211
Number of Leaflets per Leaf	4.97	0.69	.2694***	5.37	0.43	.1685***

* = $p < .05$; ** = $p < .01$; *** = $p < .001$

Table 2. Descriptors for the trees sampled in the tree-level sampling.

Descriptor	Tree R2T09	R3T09	R2T14	R3T17
Irrigation treatment	100	100	33	33
Max ht of Cls 5 stems (cm)	440	447	306	316
Max ht of tree (cm)	712	585	549	558
Biomass (kg)				
Stems	30.47	34.97	30.19	28.08
Stems, > 4 cm	18.15	25.04	17.18	17.38
Leaves	6.14	5.17	5.45	5.14
Fruits	16.00	13.23	11.74	10.46
Total	52.61	53.37	47.38	43.68
Area (m^2)				
Stems (Length * Diam)	2.52	2.49	2.41	2.33
Leaves	82.87	69.83	73.61	69.42
LAI	3.69	3.11	3.27	3.09
LAI, projected	2.53	2.13	1.90	1.79
Sucker shoots				
Count	7	9	0	4
Leaves per shoot	12.1	13.9	0	9.7
Leaf area, % of total	3.2	5.8	0	1.7

Captions to Illustrations

Figure 1. Illustration of the angles measured on stems and leaves. A. Zenith angle of the rachis (θ_r), and zenith angle of the branch (θ_b). The azimuth direction (θ_α) is measured from true North. B. The zenith angle of a leaflet (θ_l) is measured from the vertical to the top surface of the leaflet. C. The folding angle about the leaflet midrib (θ_m) decreases with increased folding.

Figure 2. Graphic representation of the three-dimensional structure of stems in the orchard. Orchard-level sampling stems (Class 5, > 4 cm diameter) are shown in white for the sixteen trees measured. The eight 100% ET treatment trees are to the upper left; 33% ET trees are to the lower right. Tree-level sampling stems are shown on four trees sampled at this level. Diameter class is indicated by color: Class 4, green; Class 3, blue; Class 2, yellow; Class 1, pink. The gap between the two blocks of trees represents the space occupied by the unmeasured border trees.

Figure 3. Graphic depiction of tree R3T09 stems sampled in the tree-level sampling and branch-level sampling. Diameter class of tree-level sampling stems is indicated by color as in Figure 2. Stems of the branch-level sampling are shown in orange at the right-center of the tree. Not all Class 1

and Class 2 stems are depicted as explained in the text (see section 2.C.1.b. Tree-level Sampling).

Figure 4. Comparison of the heights of 58 points in the canopy measured with a plumb line (Measured Height) or calculated from tree-level geometric sampling data (Calculated height).

Figure 5. Comparison of the horizontal distance from the trunk of 58 points in the canopy measured with a plumb line (Measured Distance) or calculated from tree-level geometric sampling data (Calculated Distance).

Figure 6. The cumulative length of stem segments sampled in the orchard-level sampling (eight trees per treatment) shown by diameter size class.

Figure 7. The cumulative length of stem segments sampled in the tree-level sampling (two trees per treatment) shown by diameter size class.

Figure 8. The cumulative frequency of azimuth angles by stem size class for the tree-level sampling.

Figure 9. The cumulative frequency of zenith angles by stem size class for the tree-level sampling.

Figure 10. The cumulative frequency of azimuth angles by leaf type. Terminal leaflets, "T", and lateral leaflets, "L", in the 100% ET treatment, "100", and 33% ET treatment, "33", are denoted.

Figure 11. The cumulative frequency of zenith angles by leaf type. Terminal leaflets, "T", and lateral leaflets, "L", in the 100% ET treatment, "100", and 33% ET treatment, "33", are denoted. Zenith angle can exceed 180° if the top surface of the leaf faces downward.

Figure 12. Plot of the two parameters of the beta distribution, mu and nu, for the five stem diameter size classes in the 100% ET treatment (x) and the 33% ET treatment (o). The positions of idealized distributions (*) are labelled on the plot.

Figure 13. Plot of the two parameters of the beta distribution, mu and nu, for terminal leaflets, "T", and lateral leaflets, "L", in the 100% ET treatment, "100", and 33% ET treatment, "33". The positions of idealized distributions (*) are labelled on the plot.

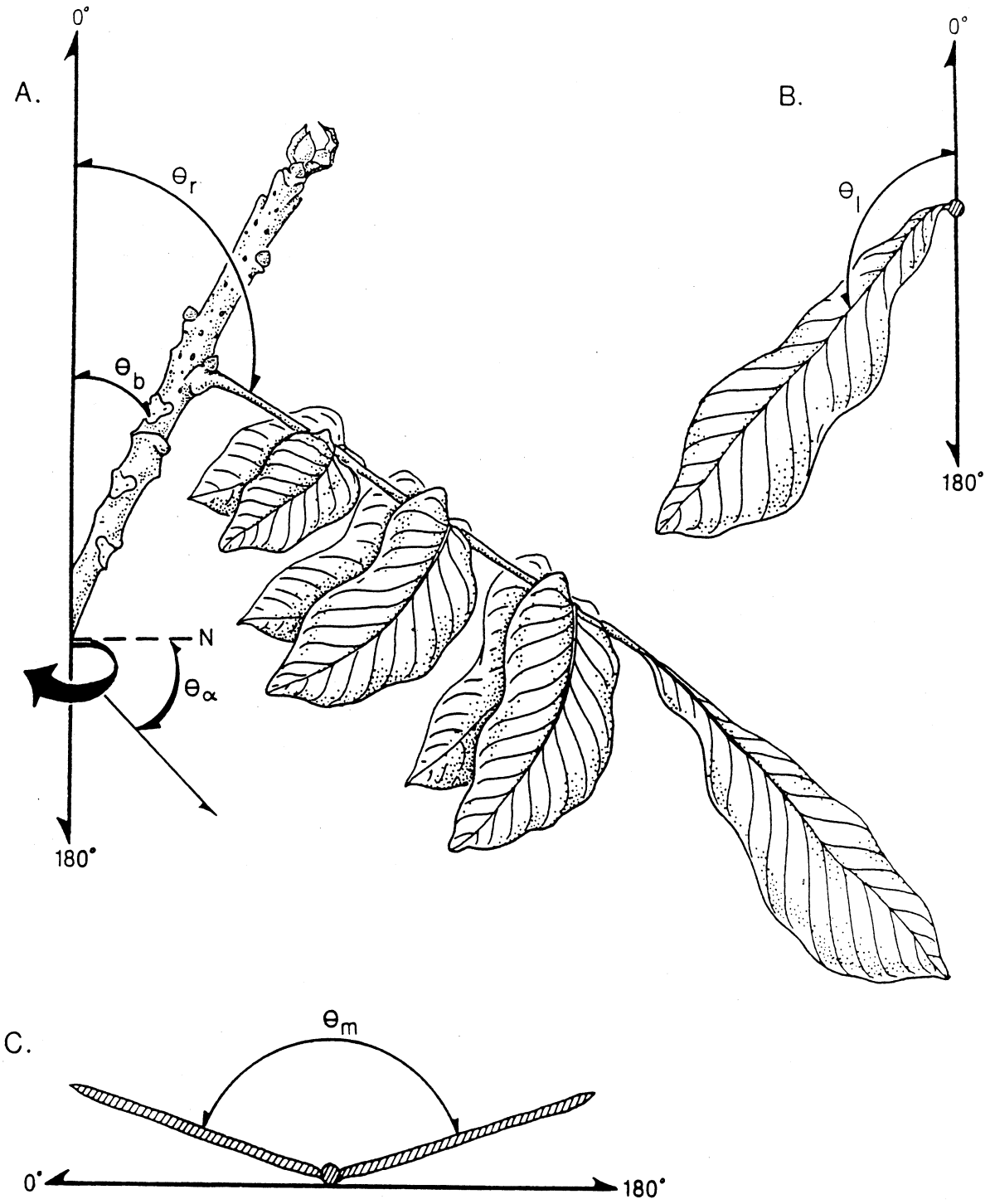
A.
0°
θr
θb
N
θα
180°
B.
0°
θl
180°
C.
θm
0°
180°

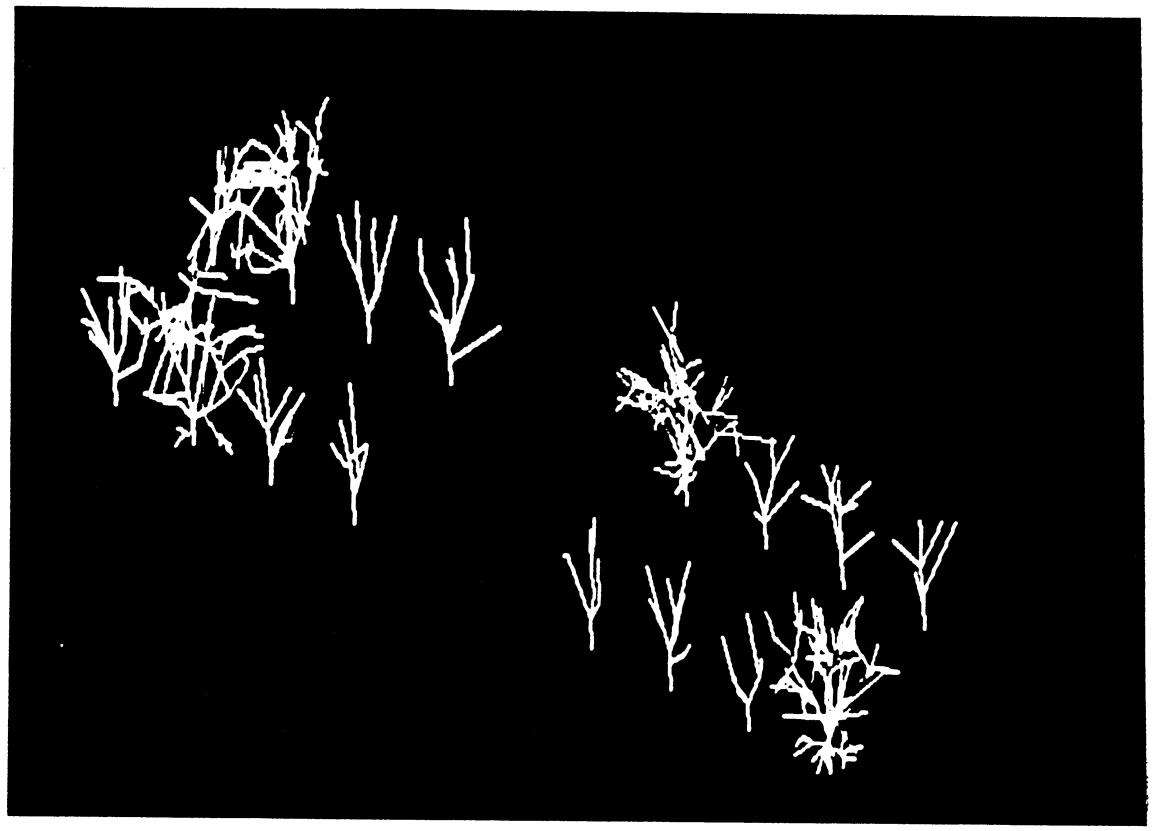

Figure 2. Martens et al., "Measurement of Tree Canopy Architecture"

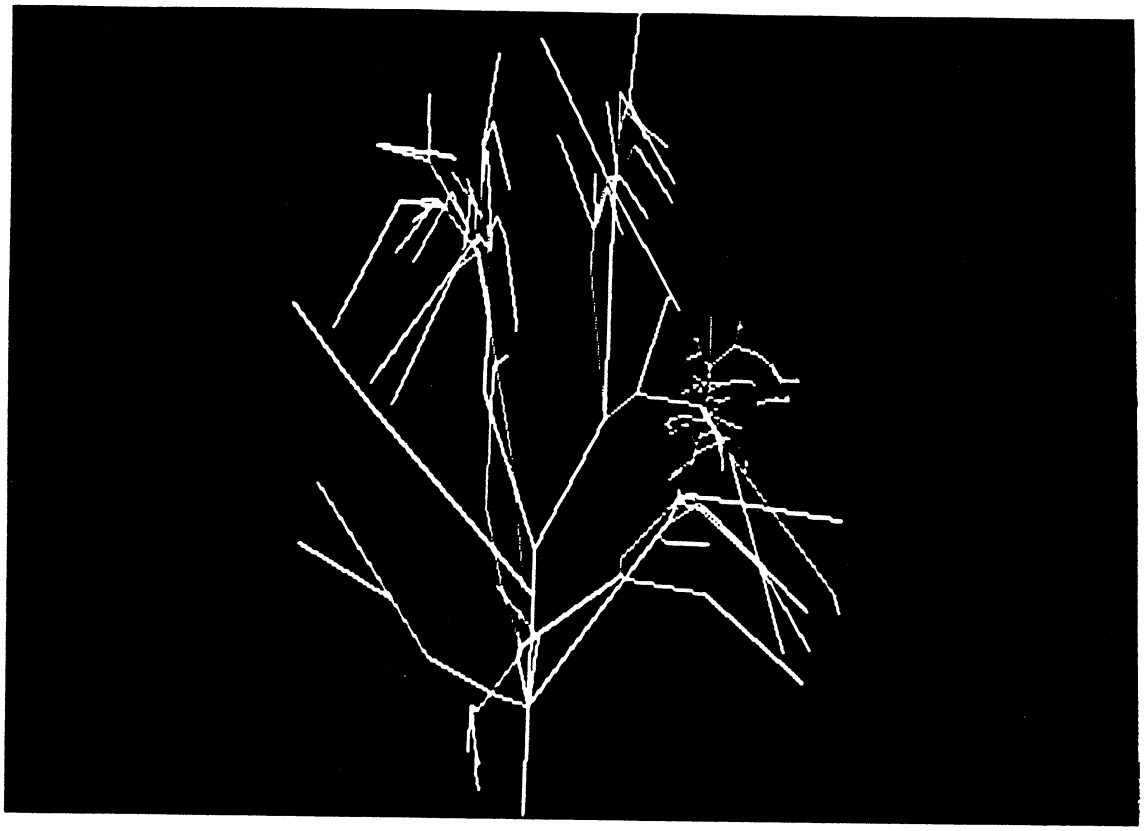

Figure 3. Martens et al., "Measurement of Tree Canopy Architecture"

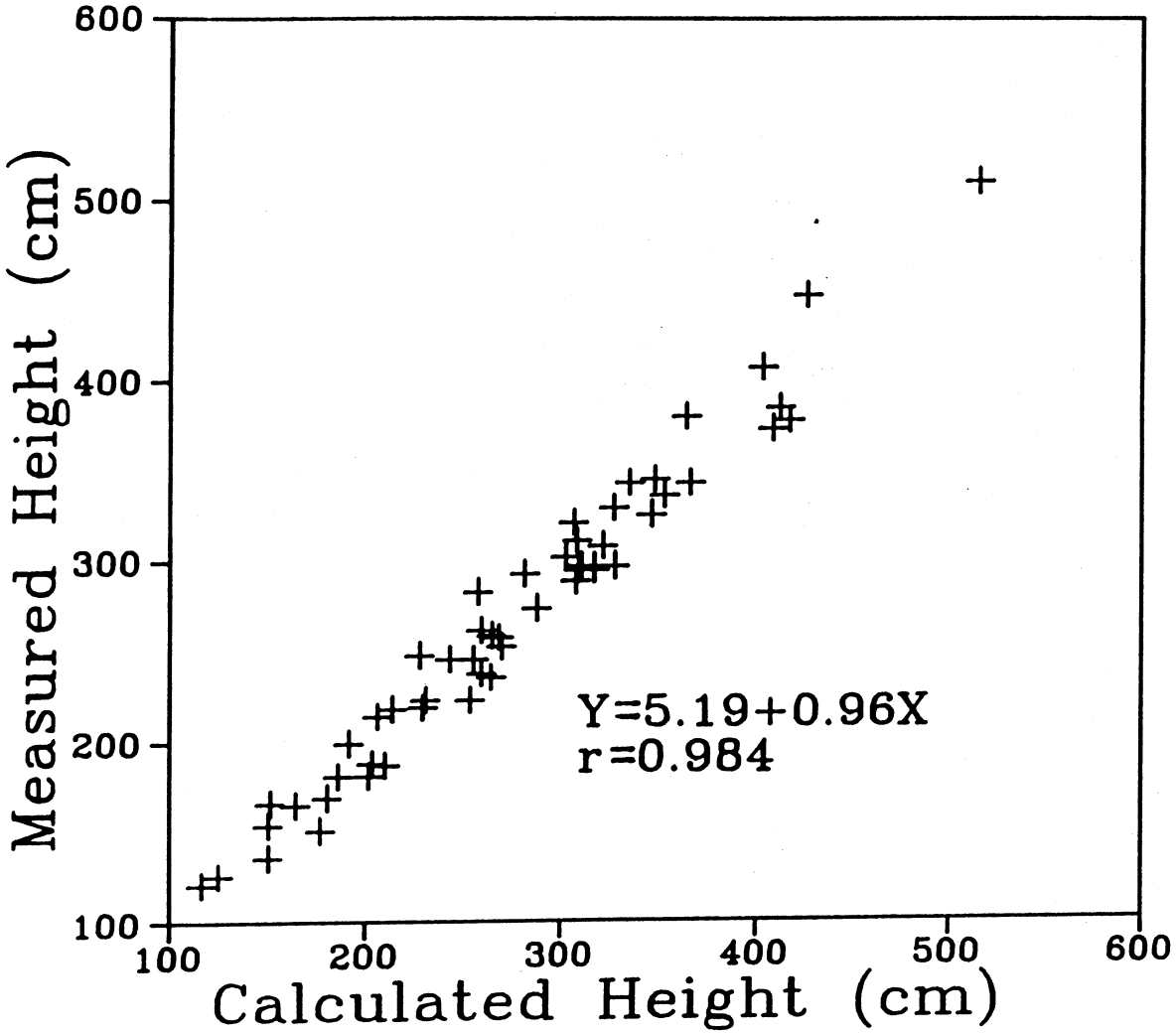

Figure 4. Martens et al., "Measurement of Tree Canopy Architecture"

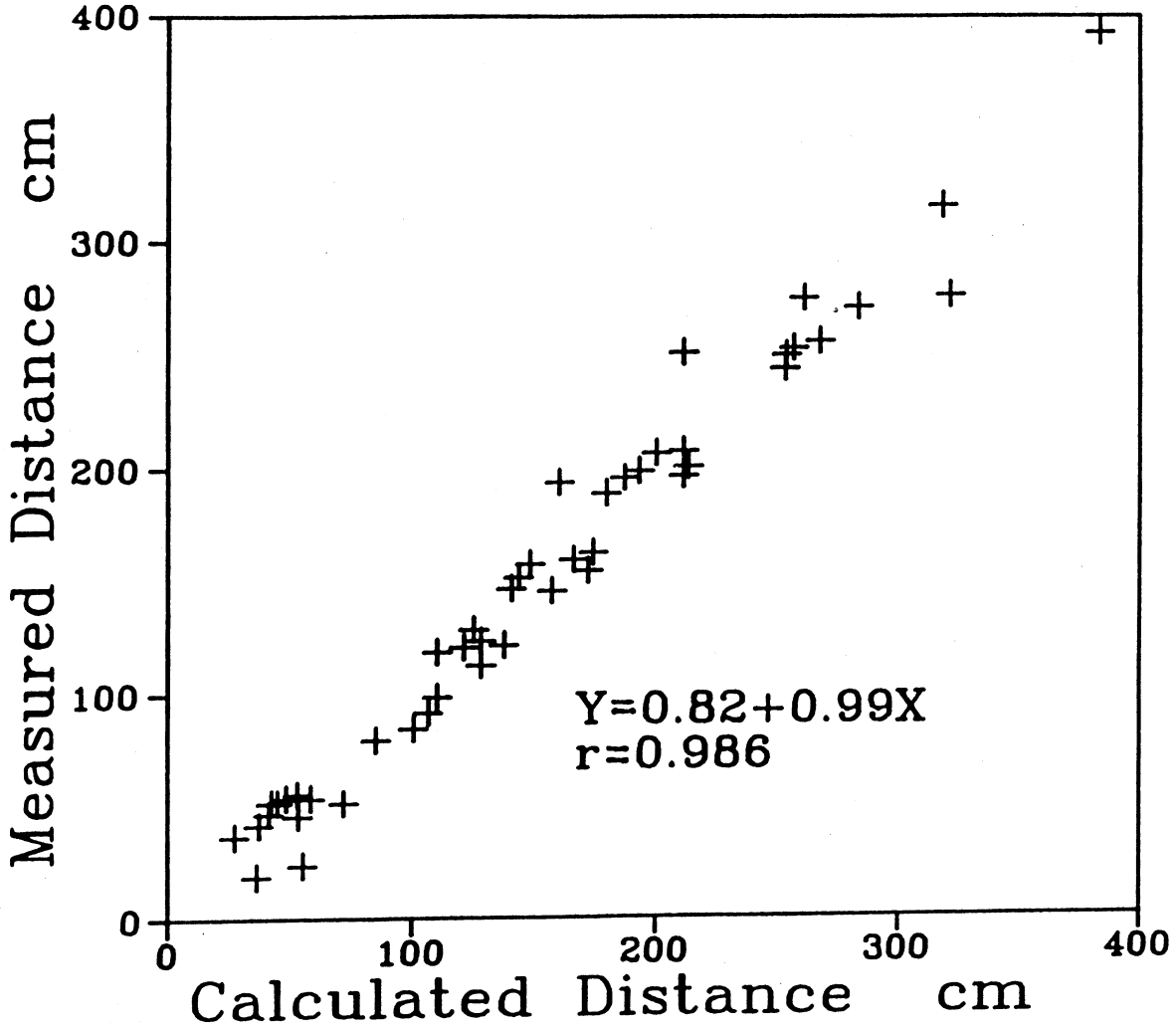

Figure 5. Martens et al., "Measurement of Tree Canopy Architecture"

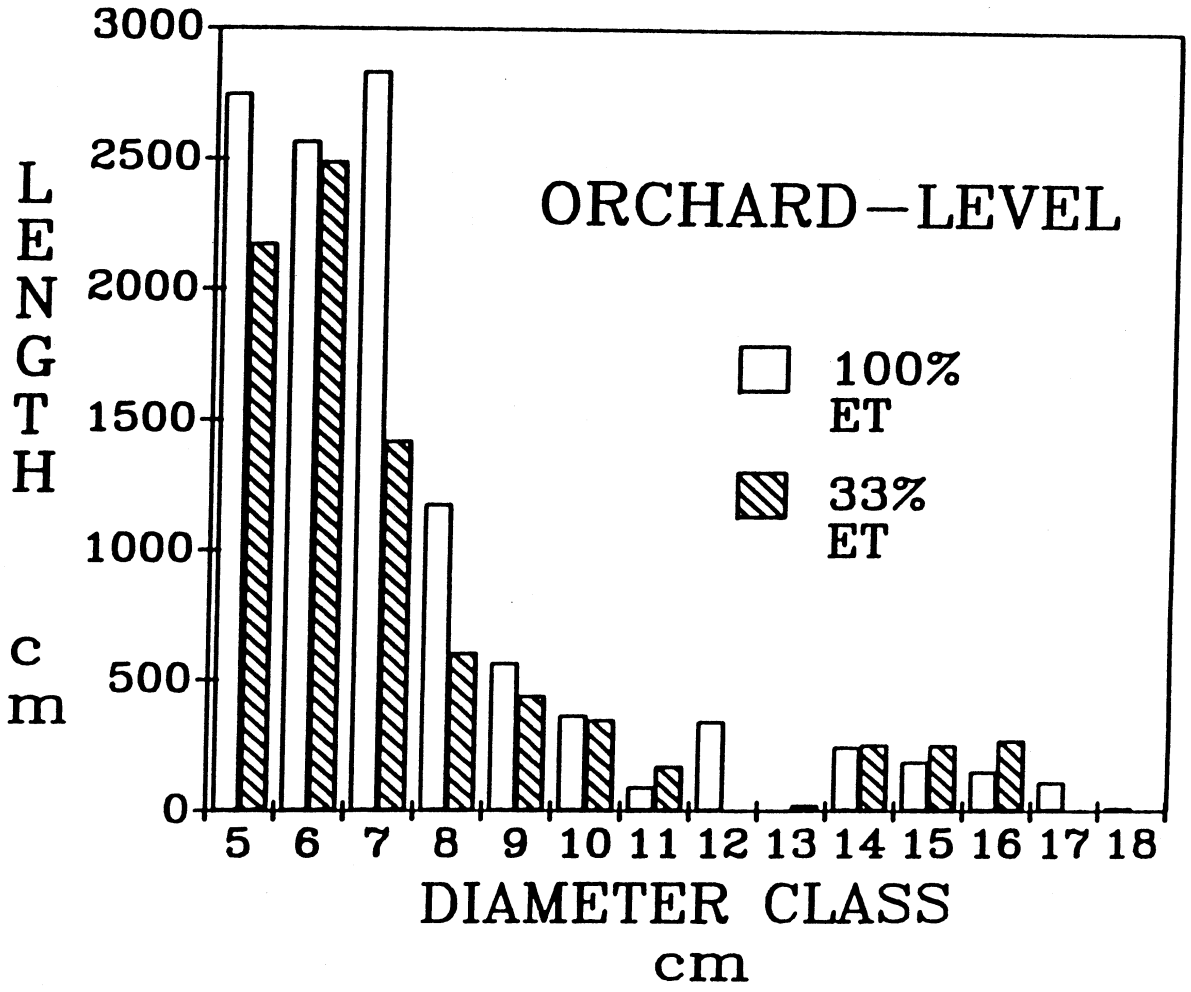

Figure 6. Martens et al., "Measurement of Tree Canopy Architecture"

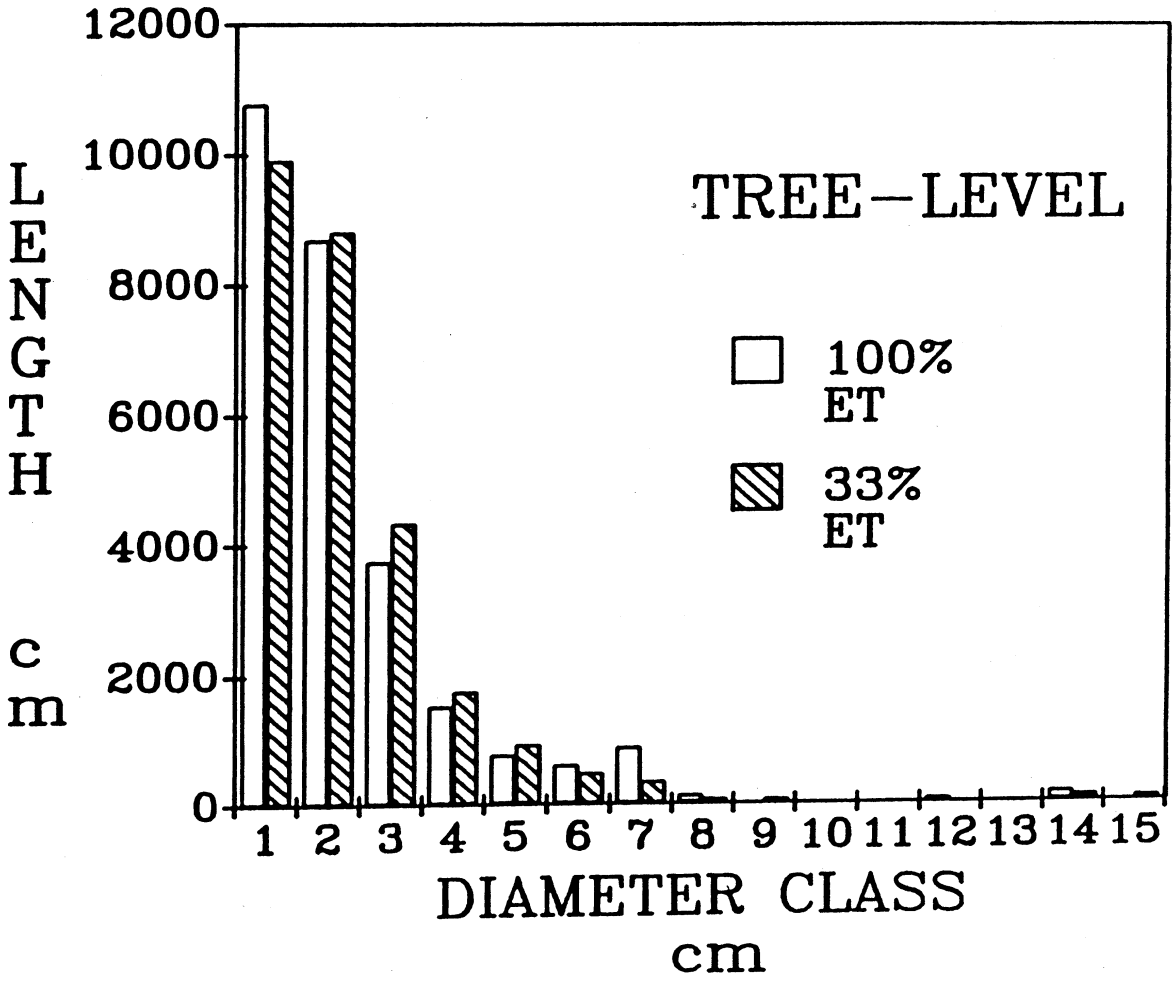

Figure 7. Martens et al., "Measurement of Tree Canopy Architecture"

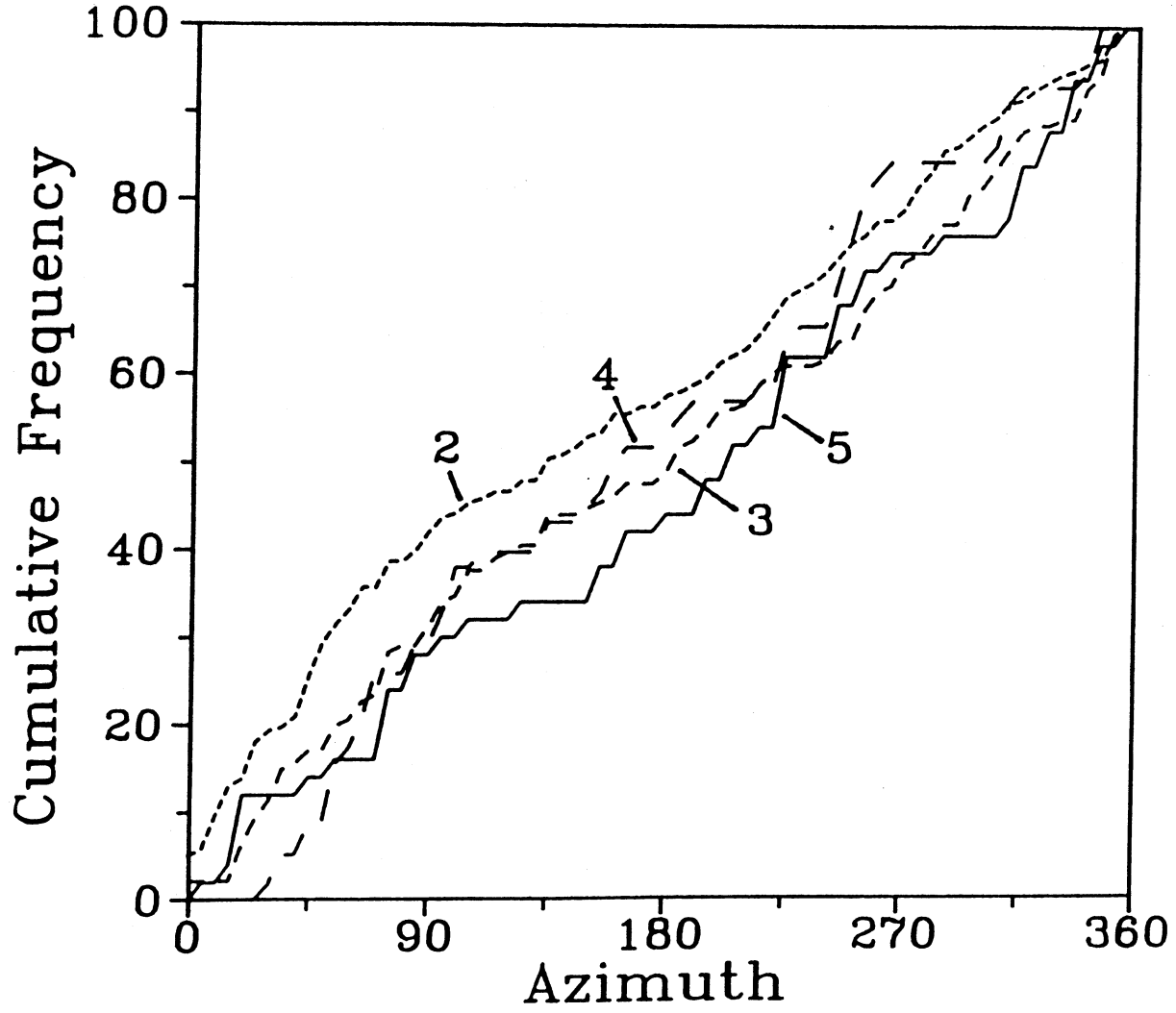

Figure 8. Martens et al., "Measurement of Tree Canopy Architecture"

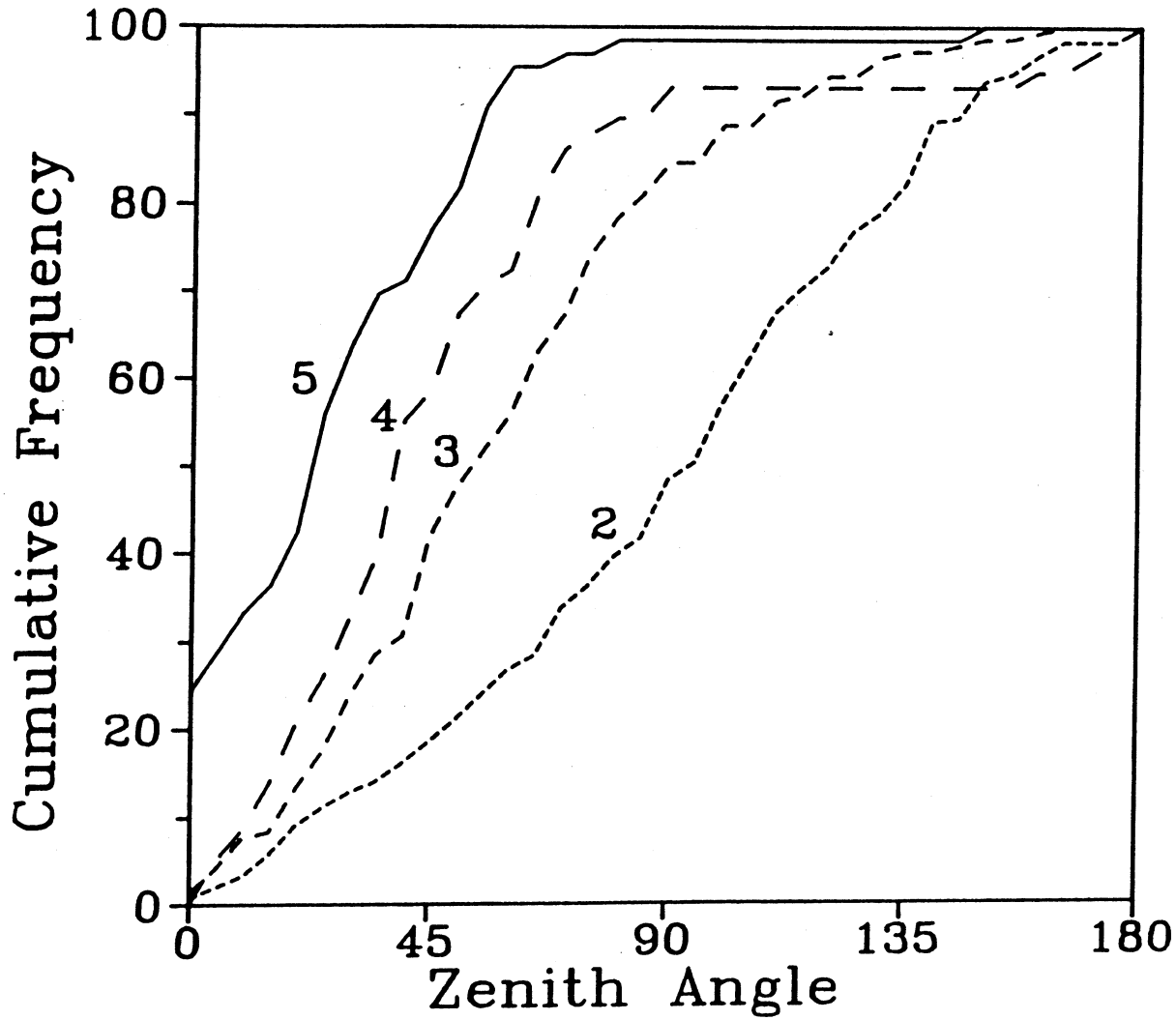

Figure 9. Martens et al., "Measurement of Tree Canopy Architecture"

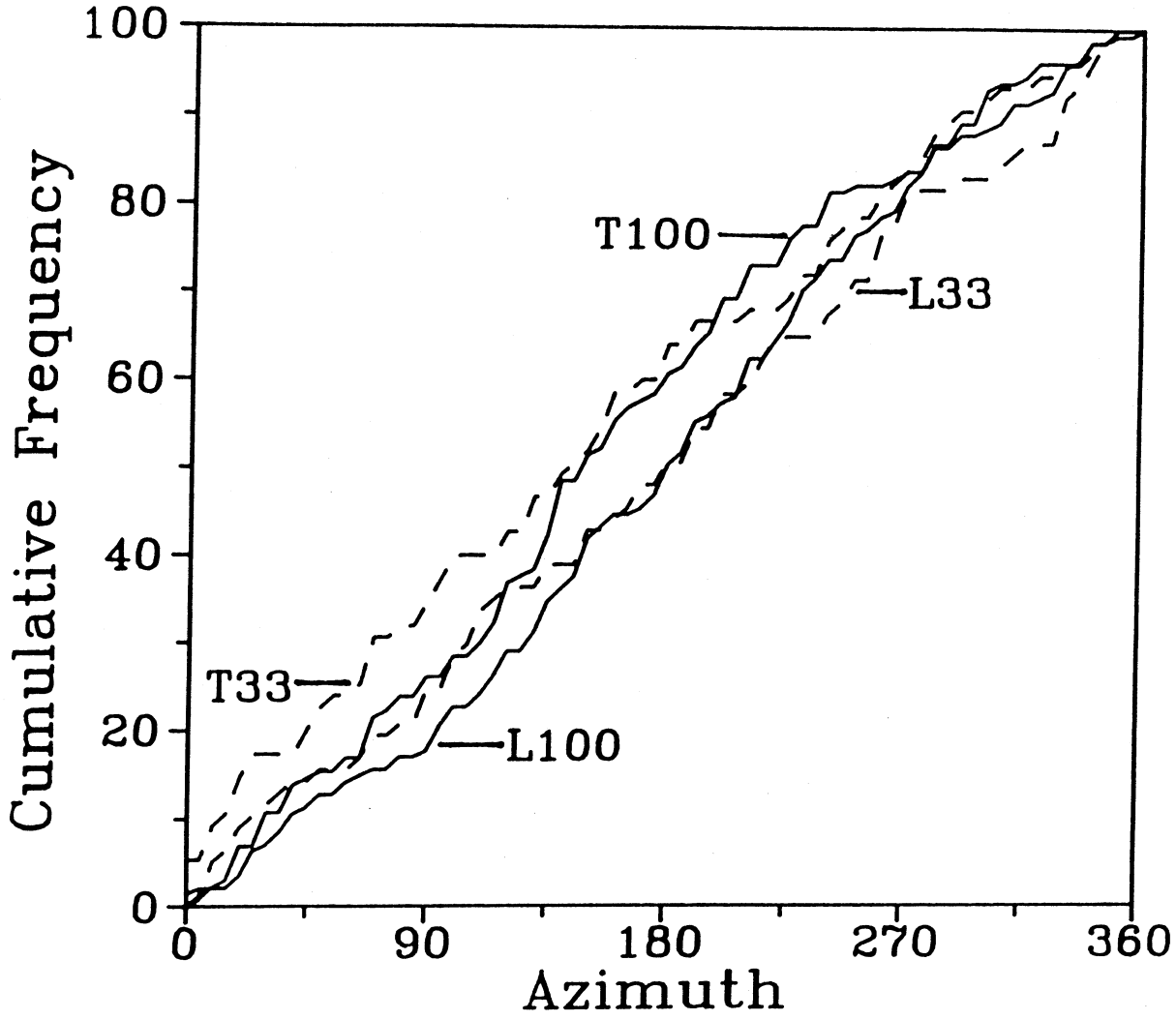

Figure 10. Martens et al., "Measurement of Tree Canopy Architecture"

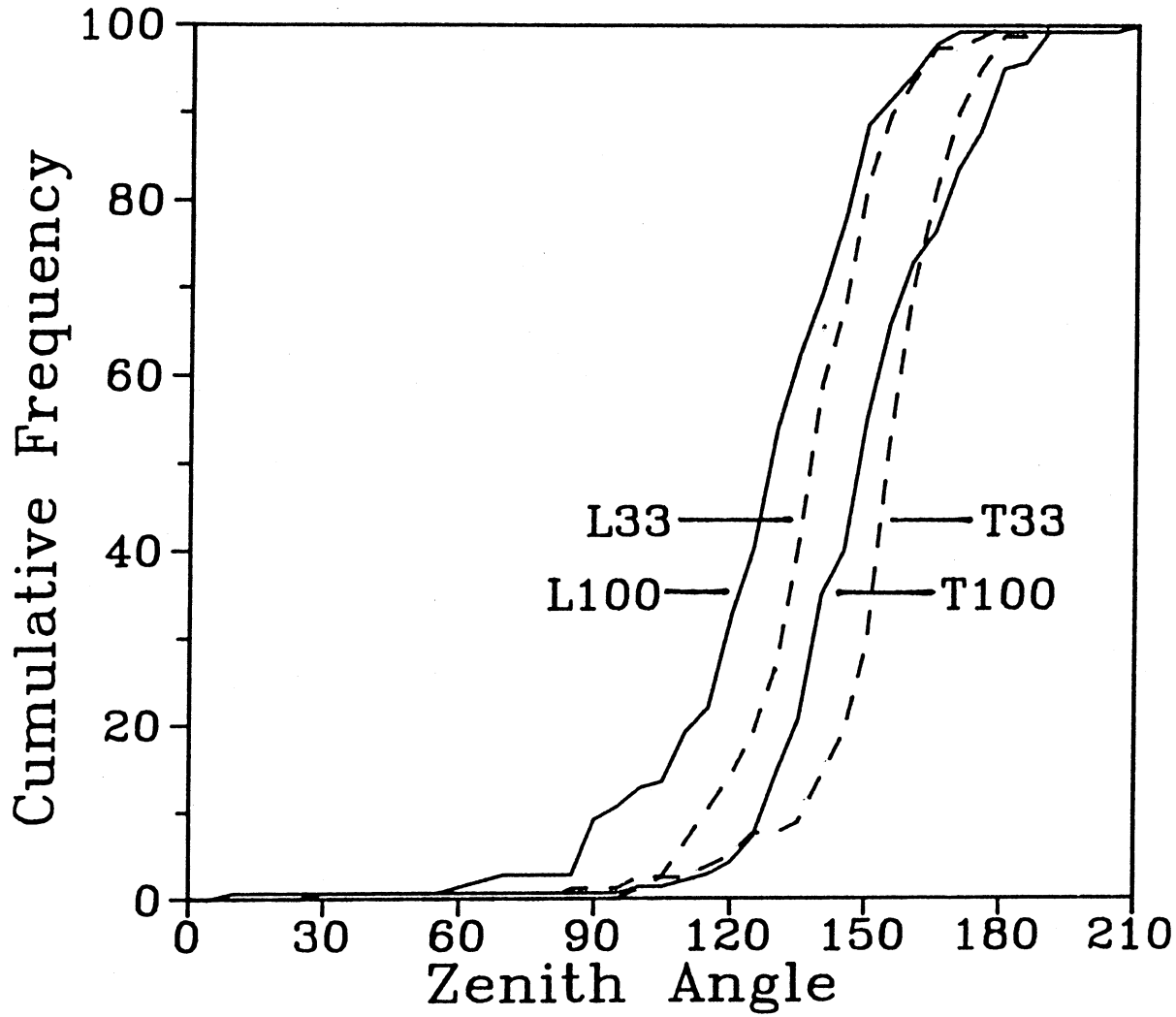

Figure 11. Martens et al., "Measurement of Tree Canopy Architecture"

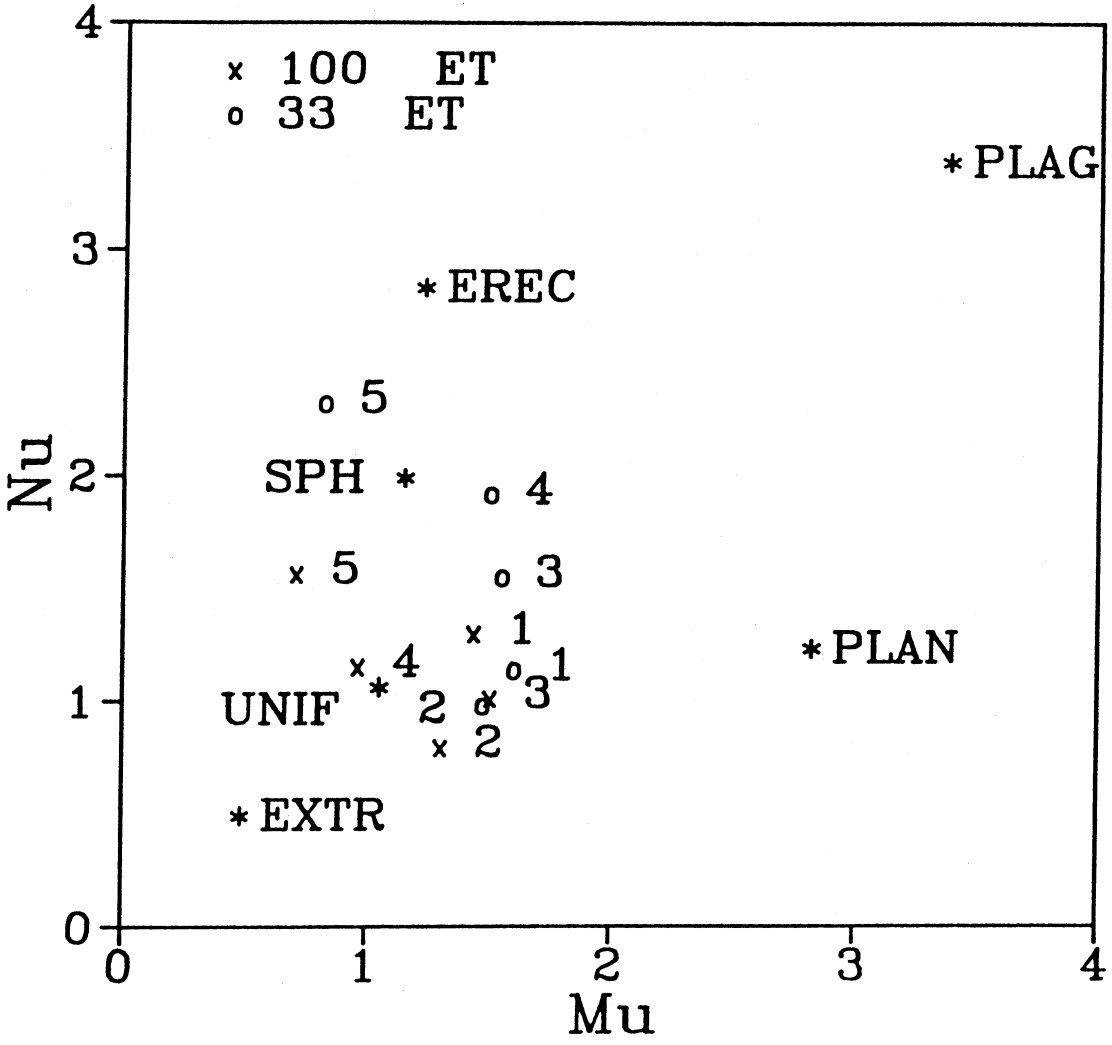

Figure 12. Martens et al., "Measurement of Tree Canopy Architecture"

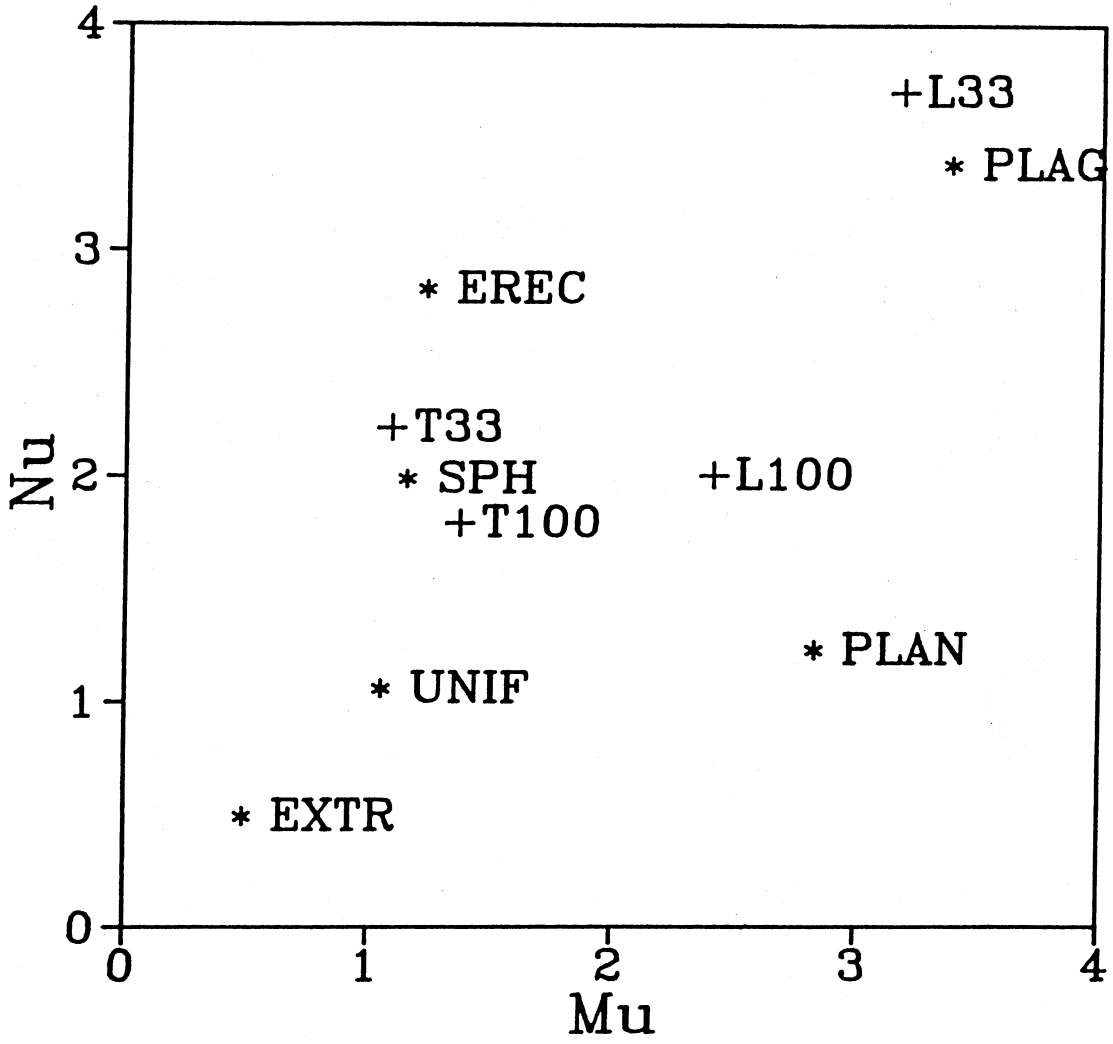

Figure 13. Martens et al., "Measurement of Tree Canopy Architecture'

1. OBJECTIVES

The overall objectives of the Eos Synergism Study was to determine the optimum orbital tracks required for the Eos visible/IR and SAR instruments to be used in monitoring terrestrial ecosystems and other vegetated surfaces. In meeting these objectives, one principal focus of the studies conducted by the Eos Synergism Team was on determining the degree of the diurnal variations in microwave signatures from vegetated terrains.

The summer field program of 1987 clearly showed that some vegetation canopies have a significant (1 to 3 dB) diurnal variation in the intensity of the radar return. This observation led to a further set of questions which need to be addressed, specifically: (1) do such diurnal variations occur in other terrestrial ecosystems, and if they do, what are the magnitudes of these variations? (2) can diurnal and seasonal variations be detected on SAR imagery collected over vegetated regions? and (3) what are the implications of these diurnal and seasonal variations on the use of information derived from SAR data as inputs into forest ecosystem models.

The research conducted under our subcontract focused on addressing these issues. Specifically, the objectives of the research conducted by ERIM using the FY88 funding were to: (1) assist in the designing and conducting of an airborne SAR data collection program over a forested test site where seasonal and diurnal variations in the microwave signature are expected; (2) further develop and evaluate techniques required for calibration of airborne SAR imagery over vegetated regions; and (3) develop a methodology whereby the information derived from SAR data can be linked to forest ecosystem models.

2. MAJOR ACCOMPLISHMENTS

During the past year, the following items were accomplished:

-A protocol for connecting forest ecosystem and microwave backscattering models was developed.

-Techniques for polarimetric calibration of airborne SAR data using a combination of calibrated targets and background clutter was developed and evaluated.

-Airborne SAR data collections over the Duke University Research Forest were planned and conducted.

Part of the research efforts over the past year have focused on the connections between forest ecosystem and microwave backscattering models. A paper was written to explore these connections (Kasischke and Christensen, 1990; see section 5 below). The connectivity between these models is a two-way street. On the one hand, the desired objective is to utilize remotely sensed data to provide inputs to the ecosystem models. However, in order to fully develop techniques to extract the required inputs from remote sensing data, it is often necessary to develop and validate theoretical remote sensing models which predict a signature based on the composition and structure of vegetation canopy. Once such models have been validated, they can be exercised to determine what canopy components are primarily responsible for the remote sensing signature, and hence assist in defining the information content of that signature.

Developing a set of inputs for these theoretical models is often not possible due to the number of different scattering elements which comprise a forest canopy, as well as the dynamic nature of tree canopies. However, using existing models of canopy structure and physiology may provide the means to develop the required input data set for the theoretical scattering models.

The paper by Kasischke and Christensen explores the connections between forest ecosystem and microwave scattering models. Forest ecosystem processes themselves can be organized on a hierarchical basis, e.g., processes can occur on an individual tree basis, at a stand level, at a community level, on up to ecosystem and biosphere levels. In utilizing remote sensing data as inputs to these ecosystem process

models, several limitations must be recognized. First, remote sensing data represents a snap shot of the ecosystem being processed; thus, in order to study a process, imagery from different dates has to be combined. Second, the parameters required as inputs to various ecosystem process models are not necessarily those parameters which are estimated from the remote sensing data. Often, these parameters have to be inferred from the remote sensing parameters.

In the paper, the connection between the different models are explored using old-field loblolly pine forest ecosystems as an examples. Specifically, the potential of SAR to estimate aboveground biomass is explored. There are two types of forest ecosystem models which can be used to assist the theoretical microwave modeler in his validation activities. First, there are those models which deal with describing tree geometric parameters, which are referred to as static condition models. Next there are models which deal with daily and seasonal changes of tree growth and physiology. These are referred to as dynamic models. Examples of how these models are used in the overall model validation process are presented in the paper.

In developing the data sets necessary for studies which will eventually lead to an Eos-type system, it is highly likely that data sets from various SAR satellites will be used (e.g., SIR-C, ERS-1, JERS-1, Radarsat, and the Eos SARs themselves). In order to maximize the time-period overwhich observations from these different SARs, calibration procedures will have to be developed and validated. In addition, one of the potential new advances in SAR remote sensing of vegetation canopies is the polarimetric capabilities of SARs. Techniques needed for calibration of these new polarimetric must also be developed and validated.

As will be discussed below, the next phase for the Eos Simultenaity Studies will involve utilizing aircraft SAR data. In all likelihood, data from two different systems will be used: the DC-8 JPL SAR and the P-3 ERIM/NADC SAR. Thus, during the present studies, techniques to cross-calibrate these two systems were explored.

These studies focused on exploring the similarities and differences between these two systems, and determining whether similar approaches

were suitable for calibration of these systems. This study, in essence, is the first step in cross-calibrating these two SARs. A paper (Sheen et al., 1989) resulted from this study.

This paper points out the major differences between these two systems, which lie in the antenna design and some differences in the radar receivers. How these differences alter the transmit and receive distortion matrices needed in polarimetric calibration are discussed. It is demonstrated that despite these differences, a similar approach can be used to calibrate the two different SARs. This technique involves using a combination of calibrated targets (corner reflectors and active radar calibrators) as well as clutter within the scene itself. This clutter calibration techniques involves exploiting the expected phase characteristics of the clutter, primarily the fact that one can assume that the two cross-polarized channels are completely uncorrelated and that the two like polarized channels are expected to be correlated.

Finally, using FY87 funding, an airborne SAR data collection was planned and carried out. This data collection occurred at the Duke University Research Forest in August/September 1989. This experiment was intended to determine was degree of diurnal and day-to-day variation exists in SAR signatures over a natural forest ecosystem. On 31 August 1989, approximately 15 passes of data were collected with the P-3 SAR System. On 2 September, approximately 10 passes of data were collected with the DC-8 SAR and on 3 September, an additional 3 passes of data were collected. Under the Simultaneity funding, calibrated radar targets (trihedrals and ARCs) were deployed to support these flights.

3. PLANNED ACTIVITIES

During the remainder of 1989 and during 1990, we plan to:

-In conjunction with Duke, U of Mich, and JPL scientists, select test sites within the Duke University Research Forest from which radar signatures will be extracted.

-Process and calibrate P-3 SAR data collected during the August mission.

-Compare data from all three frequencies (X, C and L-bands) collected in the early morning and mid-afternoon to determine if any diurnal trends can be detected.

-Assist in the calibration of data collected by the DC-8 SAR by acting as a consultant to JPL during their processing activities.

-In conjunction with JPL and U of Mich scientists, compare the various signatures extracted from the two radar data sets to determine if any day-to-day and diurnal variations are detected by the SARs.

-In conjunction with JPL, Duke and U of Mich scientists, compare any detected changes in radar signature to the ground truth collected during the experiment to determine the causes of those changes.

4. PERSONNEL SUPPORTED

The following personnel received support under this year's funding:

Eric S. Kasischke of ERIM was the Principal Investigator for this program. His responsibilities included development of techniques to connect forest ecosystem and microwave backscatter models, evaluation of SAR calibration techniques, and planning of airborne SAR data collections, and planning and conducting of ground-truth activities associated with the airborne SAR data collection programs. Dan R. Sheen of ERIM worked on calibration of the P-3 SAR data used in this study. Finally, Norman Christensen of Duke University worked as a consultant to this program, and assisted in the model development activities as well as assisted in the deployment of calibration targets during the airborne SAR experiments.

5. PUBLICATIONS

Two papers were published using funding from our subcontract:

Kasischke, E.S. and N. L. Christensen, Jr., Connecting Forest Ecosystem and Microwave Backscatter Models, **Int. J. Remote Sens., in press**, 1990.

Sheen, D.R., A. Freeman and E.S. Kasischke, Phase Calibration of Polarimetric Radar Images, **IEEE Trans. Geosci. Remote Sens., 27**, pp. 719-731, 1989.

Phase Calibration of Polarimetric Radar Images

DAN R. SHEEN, MEMBER, IEEE, ANTHONY FREEMAN, MEMBER, IEEE, AND ERIC S. KASISCHKE, MEMBER, IEEE

Abstract—The problem of phase calibration between polarization channels of an imaging radar is addressed in this paper. The causes of various types of phase errors due to the radar system architecture and system imperfections are examined. A simple model is introduced which can explain the spatial variation in phase error as being due to a displacement between the phase centers of the vertical and horizontal antennas. It is also illustrated that channel leakage can cause a spatial variation in phase error. Phase calibration using both point and distributed ground targets is discussed and a method for calibrating phase using only distributed targets is verified, subject to certain constraints. Experimental measurements using the NADC/ERIM P-3 SAR system and NASA/JPL DC-8 SAR are presented. Both of these systems are multifrequency, polarimetric, airborne, Synthetic Aperture Radar (SAR) systems. Good polarimetric calibration is required to fully exploit the promising remote-sensing capabilities of these instruments.

I. Introduction

IMAGE data from Synthetic Aperture Radars (SAR's), which measure the complete polarimetric scattering matrix on a pixel-by-pixel basis, have recently become available within the microwave remote-sensing community. The Jet Propulsion Laboratory (JPL) has developed and flown the NASA/JPL DC-8 SAR, which operates at *C*-, *L*-, and *P*-bands and is a prototype for the next Shuttle Imaging Radar (SIR-C) [1]. In conjunction with the Naval Air Development Center (NADC), the Environmental Research Institute of Michigan (ERIM) has developed and flown the NADC/ERIM P-3 SAR, which is a high-resolution system operating at *X*-, *C*-, and *L*-bands [2], [3]. In this paper the experimental results collected by these systems and analyzed by both ERIM and JPL will be presented.

To date, most uses of imaging radar have not required accurate phase information in the image. Exceptions to this include applications such as phase differencing [4], SAR interferometry and phase unwrapping [5], and analysis of ocean wave spectra from complex images [6], [7]. This paper is concerned with the problem of calibrating the relative phases between polarization channels of a polarimetric imaging radar. The problem of absolute phase calibration does not concern us here.

Manuscript received February 16, 1989; revised July 6, 1989. This work was supported by the U.S. Navy under Contract No. N00014-87-C-0726 and by the National Aeronautics and Space Administration under Grant NAGW-1101.

D. R. Sheen and E. S. Kasischke are with the Environmental Research Institute of Michigan, Radar Science Laboratory, P.O. Box 8618, Ann Arbor, MI 48107.

A. Freeman is with the Jet Propulsion Laboratory, California Institute of Technology, 4800 Oak Grove Drive, Pasadena, CA 91103.

IEEE Log Number 8930676.

Other topics which are quite important in calibrating polarimetric radar and which will not be focused on in th paper include the amplitude calibration, registration b tween channels, signal-to-noise ratio (SNR), and chann coupling. It is possible to decouple the phase calibrati from these topics to a certain extent. Of course, one shou consider all of the different performance parameters as part of designing or totally calibrating a radar [8]. T radar parameters should be specified in a consistent ma ner. A sufficient signal-to-noise ratio (SNR) is especia important in the calibration of the radar. For example, the SNR were less than 12 dB, a RMS phase error of 1 would result. Other aspects of calibration such as cc pling or noise will only be discussed when they imp the relative phase measurements described in this pape

In Section II a brief description of the two radars given, with emphasis on the parameters important to ph calibration and to end users of data. In Section III we view the basic theory of the scattering and covaria matrices and how they are observed with a polarimet radar. Then calibration procedures using point targets a clutter are discussed. In Section IV a simple model to scribe a spatially varying phase error caused by an of in the phase centers of the antennas is developed. In S tion V we give examples of phase distortions from b the NADC/ERIM P-3 and the NASA/JPL DC-8 pol metric imaging radars. Phase calibration results using b point and distributed targets are presented.

II. Radar System Overview

In Table I some fundamental specifications for the and DC-8 SAR are listed for side-by-side comparison. systems are quite similar, with both being able to ga polarimetric data. Both systems can operate at the *C*- *L*-bands. The P-3 SAR has an additional capability fo *X*-band and has a higher resolution than the DC-8 syst However, the P-3 system cannot gather polarimetric simultaneously for multiple frequencies, while the D system can. The DC-8 system also has a *P*-band sy and the P-3 does not.

The systems also have different system architecti In Fig. 1 a simplified diagram of the DC-8 system is g [9], which shows the path lengths for transmit horiz (T, H), transmit vertical (T, V), receive horizontal H), and receive vertical (R, V). In Fig. 2 a simpl diagram of the P-3 system is given. One of the fu mental differences between the two systems is that the 8 system has two receivers, while the P-3 system ha

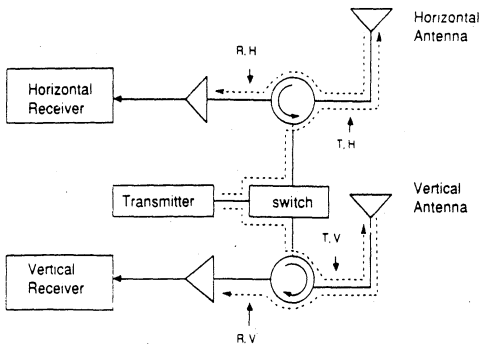

Fig. 1. Simplified diagram of the DC-8 SAR system illustrating the path lengths through the transmit and receive channels. Taken from reference [9].

TABLE I
A LIST OF OPERATING PARAMETERS FOR THE NADC/ERIM P-3 SAR AND NASA/JPL SAR

	NADC/ERIM P-3 SAR	NASA/JPL DC-8 SAR
Center frequency		
X-band	9.375 GHz	-
C-band	5.26 GHz	5.3 GHz
L-band	1.25 GHz	1.25 GHz
P-band	-	440 MHz
Wavelength		
X-band	3.2 cm	-
C-band	5.7 cm	5.65 cm
L-band	24 cm	24 cm
P-band	-	68.1 cm
Polarization isolation (boresight)		
X-band	23 dB	-
C-band	23 dB	>25 dB
L-band	23 dB	>15 dB
P-band	-	>20 dB
Range resolution (single look)	3.0 m or 1.6 m	11 m
Azimuth resolution (single look)	2.1 m	4 m
Range pixel spacing	2.4 m or 1.2 m	6.67 m
Azimuth pixel spacing	1.62 m	3.03
Image size in pixels (az x ra)	4096 x 4096	4096 x 750
Incidence angle range	20 to 65 deg*	20 to 70 deg

* Incidence angle is adjustable beyond this range for special situations.

receiver which is switched between the V and H antennas on successive pulses. The pulse-to-pulse variable attenuator in the P-3 system can be set to different values for all of the different transmit and receive polarizations. The different settings of the attenuator cause different phase shifts and gains for each of the combinations of transmit and receive polarizations. This has important implications in the theoretical development presented in the next section. In this paper we will be primarily concerned with calibrating the end-to-end system and will not separate the radar from the SAR processor. Of course, the radar architecture can affect the theoretical formulations.

The simplified diagrams of the systems do not show the calibration signal generator that both systems have. This signal generator injects a tone or synthetic signal into the receiver channel immediately after the antennas, and can be used to radiometrically or amplitude calibrate the different receive channels. The signal generators are not used

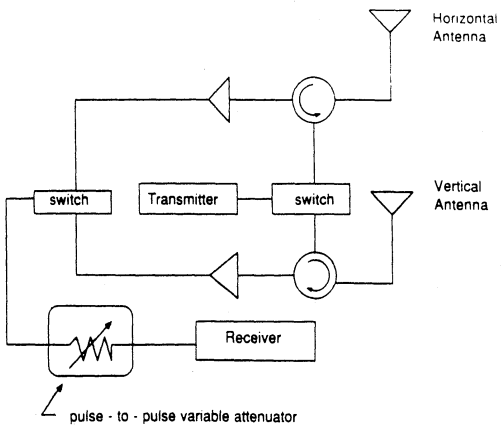

Fig. 2. Simplified diagram of the P-3 SAR system illustrating path lengths through the transmit and receive channels.

in phase calibration at this time. Also, the simplified diagrams do not show any details of how the different carrier frequencies or chirps are generated. For more detailed descriptions of the radars, see [1]–[3].

III. Background Theory

A. Measurement of the Scattering Matrix

The goal of a polarimetric imaging radar is to measure the scattering matrix from an area of the earth's surface. The scattering matrix S relates the incident electric field E_i to the scattered field E_s by

$$\begin{bmatrix} E_{S1} \\ E_{S2} \end{bmatrix} = \frac{e^{jkr}}{r} \begin{bmatrix} S_{11} & S_{12} \\ S_{21} & S_{22} \end{bmatrix} \begin{bmatrix} E_{i1} \\ E_{i2} \end{bmatrix} \tag{1}$$

where subscripts 1 and 2 usually refer to horizontal (H) and vertical (V) polarization, k is the wavenumber, and r is the range. For a reciprocal scattering medium, $S_{12} = S_{21}$ [10].

We define a matrix M, which is composed of the complex value of each channel for each pixel of the uncalibrated polarimetric image. Because of path length differences, gain differences, coupling between channels, and noise, the measured (complex valued) matrix M is not equal to the scattering matrix. Zebker *et al.* [9] have described the DC-8 radar system architecture shown in Fig. 1 and have used the following formula (after [11]) to relate the scattering matrix S to the measured matrix M:

$$M = R^t S T + N$$

$$M = \begin{bmatrix} R_{11} & R_{21} \\ R_{12} & R_{22} \end{bmatrix} \begin{bmatrix} S_{11} & S_{12} \\ S_{21} & S_{22} \end{bmatrix} \begin{bmatrix} T_{11} & T_{12} \\ T_{21} & T_{22} \end{bmatrix} + \begin{bmatrix} N_{11} & N_{12} \\ N_{21} & N_{22} \end{bmatrix} \tag{2}$$

where R and T are the receive and transmit distortion matrices, respectively, superscript t denotes the transpose, and the matrix N represents the noise present in each channel. For an ideal radar system, R and T are both identity matrices multiplied by complex constants. The off-diagonal terms of R and T represent leakage or coupling between channels and ideally would be very small.

The P-3 system collects data for *HH* (horizontal transmit, horizontal receive), *HV* (horizontal transmit, vertical receive), *VH* (vertical transmit, horizontal receive), and *VV* (vertical transmit, vertical receive) individually on successive pulses. The measured matrix M cannot be expressed as in (2) because the variable attenuator setting is changed from pulse to pulse. The phase shift through the attenuator can vary by as much as 10° for different settings of attenuation ranging from 0 to 64 dB. The pulse-to-pulse variable attenuator creates four independent receiver channels. To model these independent gains and phases the R^tST product in (2) would have to have each element multiplied by a complex constant. For the P-3 SAR, we will not separate the effects of the R matrix, the T matrix, and these complex constant factors and only deal with the total phase shifts.

B. The Covariance Matrix of Distributed Targets

For polarimetric clutter or scatter from distributed targets, the scattering statistics can be described by the covariance matrix C [12], which is defined as

$$C = \begin{bmatrix} \langle |S_{11}|^2 \rangle & \langle S_{11}S_{21}^* \rangle & \langle S_{11}S_{22}^* \rangle \\ \langle S_{21}S_{11}^* \rangle & \langle |S_{21}|^2 \rangle & \langle S_{21}S_{22}^* \rangle \\ \langle S_{22}S_{11}^* \rangle & \langle S_{22}S_{21}^* \rangle & \langle |S_{22}|^2 \rangle \end{bmatrix} \quad (3)$$

where the $\langle\ \rangle$'s indicate expected values, the $|\ |$'s indicate absolute value, and * indicates the complex conjugate. The expected covariance matrix for the clutter from distributed targets can be simplified somewhat from the general expression. Under the second-order Born approximation for a layer of randomly positioned particles, the like- and cross-polarized elements of the scattering matrix are completely uncorrelated [12]. This is because the cross-polarized terms come entirely from higher-order scattering (two-bounce or greater), while the like-polarized terms usually come predominately from first-order scattering (single-bounce). For randomly positioned scatterers the higher-order scattering paths are independent of the first-order scattering paths and thus, the cross- and like-polarized terms of the scattering matrix are uncorrelated. The final resultant covariance matrix as a function of the scattering matrix S has the following form:

$$C = \begin{bmatrix} \langle |S_{11}|^2 \rangle & 0 & \langle S_{11}S_{22}^* \rangle \\ 0 & \langle |S_{21}|^2 \rangle & 0 \\ \langle S_{22}S_{11}^* \rangle & 0 & \langle |S_{22}|^2 \rangle \end{bmatrix}. \quad (4)$$

The only phase difference which is critical is that between the *HH* and *VV* channels. This would indicate that a polarimetric radar would only have to be phase calibrated between the *HH* and *VV* channels to collect good data on different types of ground clutter. A trihedral corner reflector would be sufficient to do this phase calibration. Of course, to examine other targets or clutter where cross- and like-polarized scatter are correlated, one would also need to phase calibrate the cross-polarized channels relative to the like-polarized channels.

Ignoring the effects of noise and channel coupling, it has been shown by [9] that

$$\begin{aligned} \arg(M_{11}M_{22}^*) &= \arg(S_{11}S_{22}^*) + \phi_t + \phi_r \\ \arg(M_{12}M_{21}^*) &= \phi_t - \phi_r \end{aligned} \quad (5)$$

where ϕ_t is the phase offset between the H and V transmit channels, and ϕ_r is the phase offset between the H and V receive channels. With this model, polarimetric phase calibration can be carried out by using any scene where the cross-polarized measurements M_{12} and M_{21} are significant with respect to the like-polarized (e.g., $|M_{12}|^2 \geq 10^{-1}|M_{11}|^2$) to estimate $(\phi_t - \phi_r)$. To find the sum of the transmit and receive phase differences, the authors recommend using an area in the image, where $\langle \arg(S_{11}S_{22}^*) \rangle = 0$, given a single-bounce scattering model. Hence $(\phi_t \pm \phi_r)$ are easily calculated, and the measurement matrix M can be phase calibrated. We shall show from our results that this approach is justified in many circumstances, and shall examine further the range of clutter backgrounds over which it can be used.

C. Calibration Using Trihedral Corner Reflectors

The goal of polarimetric calibration is to determine the relative values of the elements of the R and T matrices in (2) to allow the determination of the scattering matrix S from the measured matrix M. Also, the statistics of the elements of the noise matrix N should be determined. The general procedure described by [11] is to deploy targets with known scattering matrices and form enough independent equations to determine the elements of the R and T matrices. For example, consider the scattering matrix associated with a trihedral corner reflector:

$$S_{\text{TRI}} = \begin{bmatrix} 1 & 0 \\ 0 & 1 \end{bmatrix}. \quad (6)$$

Depending upon the radar system, it may be valid to express the radar measurement of the trihedral in terms of the R and T matrices alone. The associated radar measurement neglecting noise is

$$\begin{aligned} M_{\text{TRI}} &= \begin{bmatrix} T_{11}R_{11} + T_{21}R_{21} & T_{12}R_{11} + T_{22}R_{21} \\ T_{11}R_{12} + T_{21}R_{22} & T_{12}R_{12} + T_{22}R_{22} \end{bmatrix} \\ &= T_{22}R_{22}\begin{bmatrix} T_{11}R_{11}/T_{22}R_{22} & \dfrac{T_{12}R_{11}}{T_{22}R_{22}} + \dfrac{R_{21}}{R_{22}} \\ \dfrac{T_{11}R_{12}}{T_{22}R_{22}} + \dfrac{T_{21}}{T_{22}} & 1 \end{bmatrix} \end{aligned} \quad (7)$$

to a good approximation if the off-diagonal terms of the R and T matrices are small compared to the diagonal terms.

For phase calibration, we find that if the off-diagonal

terms of T and R are small, then

$$\arg (M_{11}M_{22}^*)_{\text{TRI}} = \arg (T_{11}R_{11}/T_{22}R_{22}) = \phi_t + \phi_r = \phi_L \quad (8)$$

where $\phi_t = \arg (T_{11}/T_{22})$, $\phi_r = \arg (R_{11}/R_{22})$, and ϕ_L is the total phase difference between the like-polarized channels in the radar. As was pointed out in Section III-A, for the P-3 SAR, ϕ_L cannot be broken down in terms of ϕ_t and ϕ_r without first removing the effect of the variable attenuator. A trihedral could be used to find $(\phi_t + \phi_r)$ or ϕ_L. Additional targets such as dihedrals at a variety of orientations, gridded trihedrals, or Active Radar Calibrators (ARC's) [13] could be used to solve for other unknowns in the R and T matrices. For example, the procedure using dihedrals at a variety of orientations and trihedrals is given in [11]. ARC's could also be used in a similar fashion.

D. Calibration Using Clutter

The fact that clutter has a correlation between the two like-polarized channels and between the two cross-polarized channels can be used as an aid in phase calibration [9]. This promises to be very useful, since calibration targets require careful deployment and some degree of ground support. Also, the phase calibration can change spatially in the image, and many calibration targets would have to be deployed to examine the spatial variation of the phase. As outlined previously, it is not expected that the like- and cross-polarized channels would be correlated with each other. Thus it will not be possible to determine this relative phase shift using in-scene clutter. The method would only allow *HH* to be phase calibrated with respect to *VV*, and likewise for *VH* to be phase calibrated with *HV*. In the JPL data the average *HV* and *VH* phase difference is corrected for, and the *HV* and *VH* channels are averaged together. The average phase difference between *HV* and *VH* is included in the header of the JPL compressed data format. Using the clutter phase statistics, one could partially phase calibrate an image and could also examine how the relative phases shift spatially in the image.

Given a cell of background "clutter" with the following scattering matrix:

$$S = \begin{bmatrix} a & b \\ b & c \end{bmatrix} \qquad a, b, c \neq 0 \quad (9)$$

and neglecting the effects of noise, the associated radar measurement can be expressed in terms of the R and T matrices as follows:

$$M_c = \begin{bmatrix} aT_{11}R_{11} + bT_{11}R_{11} + bT_{21}R_{11} + cT_{21}R_{21} & aT_{12}R_{11} + bT_{22}R_{11} + bT_{12}R_{21} + cT_{22}R_{21} \\ aT_{11}R_{12} + bT_{21}R_{12} + bT_{11}R_{22} + cT_{21}R_{22} & aT_{12}R_{12} + bT_{12}R_{22} + bT_{22}R_{12} + cT_{22}R_{22} \end{bmatrix}. \quad (10)$$

Neglecting channel coupling (i.e., assuming that off-diagonal terms of T and R are negligible) results in

$$M_c = \begin{bmatrix} aT_{11}R_{11} & bT_{22}R_{11} \\ bT_{11}R_{22} & cT_{22}R_{22} \end{bmatrix} \quad (11)$$

and for phase calibration we find that

$$\arg \langle M_{11}M_{22}^* \rangle = \phi_t + \phi_r = \phi_L \quad (12a)$$

if

$$\arg \langle ac^* \rangle = 0$$

expected for a single-bounce terrain, and also,

$$\arg \langle M_{21}M_{12}^* \rangle = \phi_t - \phi_r. \quad (12b)$$

In order for the above expressions to be valid the channel coupling must be negligible. For this to be true, the ratio of cross- to like-polarized backscatter must be much greater than the cross-polarization isolation terms. For example,

$$\frac{|b|^2}{|a|^2} \gg \frac{|T_{12}|^2}{|T_{22}|^2}, \quad \text{etc.} \quad (13)$$

A channel isolation greater than 20 dB is probably sufficient for most clutter. If these conditions apply, then $\langle M_{11}M_{12}^* \rangle$, $\langle M_{11}M_{21}^* \rangle$, $\langle M_{22}M_{12}^* \rangle$, and $\langle M_{22}M_{12}^* \rangle$ should approximately equal zero, since $\langle S_{11}S_{12}^* \rangle$, $\langle S_{11}S_{21}^* \rangle$, $\langle S_{22}S_{12}^* \rangle$, and $\langle S_{22}S_{21}^* \rangle$ should theoretically be zero according to some clutter models [12].

IV. Spatial Variation of Phase Calibration

In Fig. 3 we present some imaging geometry characteristics of a SAR important to in-phase calibration. The antenna may have slightly different phase centers for vertical (V) and horizontal (H) polarization. This difference from H to V is given by the vector $\vec{d}$ and is exaggerated in the illustration. From Fig. 3 it can be seen that one expects the pathlengths H to V and V to H to be the same. Thus phase calibration of the *HV* channel relative to the *VH* channel should be spatially constant in the image. However, this is not the case with the *HH* versus *VV* channel because of the offset $\vec{d}$. The phase variation across the image can be written as follows:

$$\phi_L(R) = \frac{4\pi}{\lambda}\left[\vec{d} \cdot \frac{\vec{R}}{|R|}\right] + \theta_c \quad (14)$$

where ϕ_L is the phase of *VV* relative to *HH*, λ is the radar wavelength, $\vec{d}$ is the offset from H to V antenna phase centers, $\vec{R}$ is the vector from the radar to the pixel of interest, and θ_c is a constant phase offset resulting from different path lengths in the transmitter and receiver for *HH* and *VV*. In general, $\vec{R}$ and $\vec{d}$ will have along-track as well as cross-track components. However, in a strip-map SAR, the along-track components should be negligible. Of course, offsets in the along-track direction that are large can cause registration problems which are a potential source of error. Neglecting any along-track component,

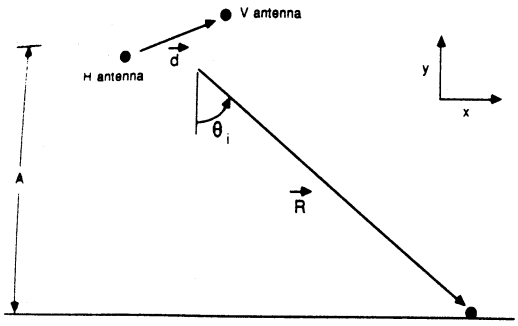

Fig. 3. SAR geometry. Used to solve for the *VV–HH* phase difference as a function of slant range *R*. *V* and *H* antenna separation exaggerated and given by the vector *d*.

$\vec{R}$ can be written in terms of the incidence angle θ_i as follows:

$$\frac{\vec{R}}{|R|} = \sin\theta_i \vec{x} - \cos\theta_i \vec{y} \tag{15}$$

and

$$\theta_i = \cos^{-1}\left[\frac{A}{R}\right] \tag{16}$$

where A is the altitude of the SAR platform above the ground. Using (15) and (16), (14) can be written in the following form:

$$\phi_L = \frac{4\pi}{\lambda}\left[d_x\left[1 - \left[\frac{A}{R}\right]^2\right]^{-1/2} - d_y\left[\frac{A}{r}\right]\right] + \theta_c. \tag{17}$$

Equation (17) expresses the phase offset ϕ_L in terms of five variables: A, R, d_x, d_y, and θ_c. Of these variables, the only known quantities are altitude (A) and slant range (R). The approach taken in analyzing experimental data from the P-3/SAR will be to examine ϕ_L as a function of R, with A set equal to the actual altitude of the SAR. Then this curve will be determined by using a nonlinear least-squares curve-fitting algorithm which can solve for d_x, d_y, and θ_c, resulting in the least-square error. Because of phase wrap-around this solution will not be unique for θ_c, but does indicate if spatial phase variations in the SAR image can be modeled as a simple H and V phase center offset.

More generally, the phase offset caused by displaced antenna phase centers could be written in terms of the transmitter and receiver phase offsets ϕ_t and ϕ_r. In this case the system model for phase error is,

$$\phi_t = \phi_{t0} + \frac{2\pi}{\lambda}\left[\vec{d}_t \cdot \frac{\vec{R}}{|R|}\right] + \phi_{tn} \tag{18}$$

$$\phi_r = \phi_{r0} + \frac{2\pi}{\lambda}\left[\vec{d}_r \cdot \frac{\vec{R}}{|R|}\right] + \phi_{rn} \tag{19}$$

where ϕ_{t0}, ϕ_{r0} are phase differences due to path length differences between receivers, the terms involving d_t and d_r are caused by displacement in the cross-range direction of the effective antenna phase centers on transmit and receive, and ϕ_{tn} and ϕ_{rn} are zero mean phase noise terms.

The terms ϕ_{t0} and ϕ_{r0} can be related to the path length differences Δx_t and Δx_r between transmitters and receivers, via:

$$\phi_{t0} = \frac{2\pi}{\lambda}\Delta x_t \qquad \phi_{r0} = \frac{2\pi}{\lambda}\Delta x_r. \tag{20}$$

From (20), path length differences of the order of 1/36th of a wavelength can cause phase errors on the order of 10°. In practice, it is very difficult to calibrate the entire radar transmit and receive paths to this kind of precision, particularly at the shorter wavelengths, without using ground targets. Hence the necessity of calibrating phase differences between channels by using properties of known targets. Large path-length differences can also cause misregistration between polarization channels depending upon the wavelength and resolution of the system.

Phase noise ϕ_n may be caused by the presence of additive noise in the system, as given in (2), in which case [14]

$$E[\phi_n] = 0 \text{ rad} \tag{21a}$$

and

$$S.D.(\phi_r) = \left[\frac{\text{SNR}^{-1}}{2} + \frac{\text{SNR}^{-2}}{8} + \cdots\right]^{1/2} \text{rad} \tag{21b}$$

where the SNR is the (power) signal-to-noise ratio. According to this model, an SNR of only 12 dB will cause an rms phase error of 10°. Another possible cause of phase noise is the decorrelation between the measured returns due to misregistration between polarization channels. Care must be taken in processing signals from imaging radar polarimeters to ensure that the image channels are in fact registered, to avoid excessive phase noise caused by not comparing returns from exactly the same image cell or pixel on the ground. In practice, a registration accuracy of 0.2 times the resolution is usually sufficient.

Adding or subtracting (18) and (19), we obtain:

$$\phi_t \pm \phi_r = [\phi_{t0} \pm \phi_{r0}] + \frac{2\pi}{\lambda}\left[(\vec{d}_t \pm \vec{d}_r) \cdot \frac{\vec{R}}{|R|}\right] + (\phi_{tn} \pm \phi_{rn}). \tag{22}$$

If phase noise terms in individual receiver and transmitter channels are uncorrelated, then adding or subtracting gives the following results:

$$E[\phi_{tn} \pm \phi_{rn}] = 0 \tag{23a}$$

assuming a $-\pi$ to π range for phase, and

$$S.D.(\phi_{tn} \pm \phi_{rn}) = \left[\text{Var}(\phi_{tn}) + \text{Var}(\phi_{rn})\right]^{1/2}. \tag{23b}$$

Hence the RMS phase error in the relative phase between *HH* and *VV* or between *HV* and *VH* is greater than the RMS phase errors in either the transmit or receive channels individually.

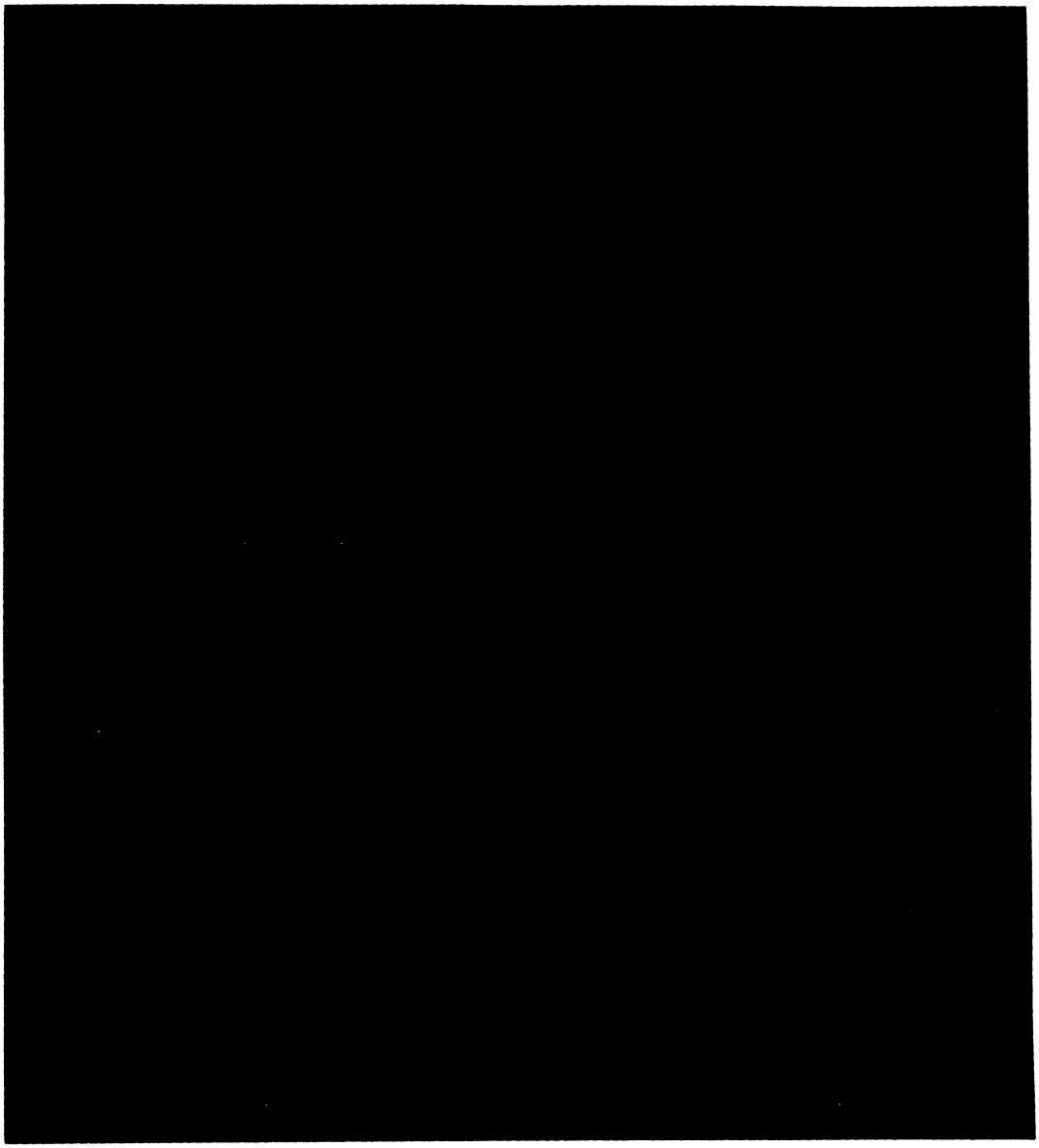

Fig. 4. *X*-band, polarimetric image phase referenced to the *HH* channel. The image is of a forested region in Alaska containing trihedrals and dihedrals.

V. Results

In this section we present results from the initial experiments designed to study the phase characteristics of the NADC/ERIM P-3 and the NASA/JPL DC-8 SAR's. Because of the different architectures for these two polarimetric SAR's (which result in the slightly different calibration approaches), we present these results separately.

A. X-Band Calibration of the P-3/SAR

In Fig. 4 a P-3/SAR *X*-band image from a forested region of approximately 1-km square is shown. This image was initially calibrated using in-scene trihedral and dihedral corner reflectors [11]. This is one approach of many, and now we shall investigate the utility of clutter for phase calibration using this image. The image is composed of four smaller images which (clockwise from the upper left corner) correspond to the *HH*, *VH*, *HV*, and *VV* polarized channels. The intensity of the image corresponds to the amplitude of the data, while the color of the image corresponds to the phase of the data. The color bar at the bottom of the image goes from $-180°$ on the left to $+180°$ on the right. The image has been phase referenced to the *HH* channel.

In Fig. 5, histograms of the relative phase for the forested region are presented. In Fig. 5(a) the histogram of the phase of *VV* versus *HH* is shown, and one can see that it appears to be Gaussian, with a width which is confined in the interval $-\pi$ to π and with a mean of 0. This is fortunate, since a wider distribution of phases would exhibit 2π ambiguities and one could not use the clutter for phase calibration. The phase distribution of *HV* versus *VH* is given in Fig. 5(b). In theory, for an ideal, calibrated, monostatic radar this should be a delta function at 0°. As illustrated in this figure, the *HV* versus *VH* phase is not always 0, but is approximately a Gaussian centered at 0, with a standard deviation much less than that of *VV* versus *HH*. In Fig. 5(c), a histogram of the phase between *VV* and *VH* is shown, which indicates that these two polarizations have a uniformly distributed phase difference and

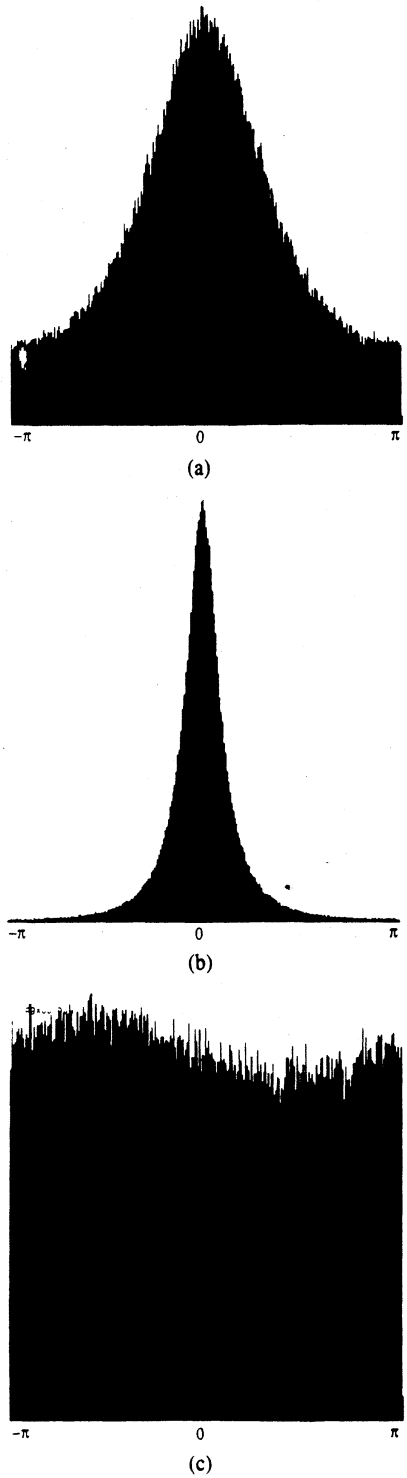

Fig. 5. Histograms of phase differences for X-band tree-clutter data: (a) *VV-HH*, (b) *HV-VH*, and (c) *VV-VH*.

are uncorrelated. The other combinations of like- and cross-polarizations were also examined and seen to be uncorrelated. Fig. 5 indicates that the mean value of the phase difference between *VV* and *HH*, as well as between *VH* and *HV*, is zero for clutter. In uncalibrated data these two mean phase differences would not necessarily be zero, but could be corrected by phase shifting one of the like-polarized channels and one of the cross-polarized channels.

One important assumption in using the clutter to calibrate the *VV* channel with respect to the *HH* channel is that the *VV* and *HH* reflections come predominately from single-bounce scattering and thus tend to be in-phase. Fig. 5(a) is a strong indication that for X-band scattering from trees, this is the case. Note that the standard deviation of the phase is significantly less than 2π. The *VV* and *HH* channels may not always tend to be in-phase. For example, at *L* band the ground-trunk interface may act like a horizontal dihedral and be a significant source of scattering. In this case *VV* and *HH* would be 180° out of phase. For this type of clutter one could not assume an average phase difference of 0° between *VV* and *HH*. An exhaustive study of clutter from different terrains has not yet been performed, but it is hoped that clutter from thick vegetation with random orientation would usually aid in-phase calibration.

The average phase difference as a function of range for the X-band tree data is presented in Figs. 6 and 7. The data has a pixel size of 2.4-m in range, and 1.6-m in azimuth. A subset of the image, which was 4096 pixels in range and 100 pixels in azimuth, was extracted. The average phase difference for a given range was computed by averaging together the phases for 100 azimuth pixels. The *HV-VH* phase is plotted in Fig. 6 and seen to be zero across most of the image, with the exception of some near-range points. The near-range points are in the proximity of the nadir reflection (at range 143) and should be excluded because the pre-nadir response is dominated by noise and the antenna response at these angles is uncertain. The *HV-VH* phase result is anticipated since the average phase of *HV* versus *VH* is not expected to vary across the image. The *HV* versus *VH* was calibrated by using some 45° dihedrals in the image, so that is why it is a constant 0 rather than being some other constant. The reflection from a 45° dihedral is completely cross polarized, and the *HV* and *VH* channels should be corrected so that they are in-phase. In Fig. 7 the average phase of *VV-HH* is plotted as a function of range. This results in a curve which could be fitted to the theoretical curve given by (17) by using a nonlinear least-square curve-fitting algorithm. The results are plotted with a dotted line in Fig. 7. The parameters used in (17) are $A = 2299$ pixels, and $R = 2156$ + range record number, and the fitted parameter values are $d_x = 0.26\lambda$, $d_y = -0.017\lambda$, and $\theta_c = -63.3°$. The fitted value of θ_c is not unique because of phase wrap-around, but it does give the expected variation in phase across the image quite accurately. The spatial variation (in range) of the phase of the image could easily be corrected by multiplying by a spatially varying, complex calibration factor.

This section has illustrated that radar clutter from distributed trees has prove to be useful for in-phase calibration of *VH* relative to *HV*, and *HH* relative to *VV* for the P-3/SAR. Also, this section has demonstrated that the relative phase variation across the P-3/SAR image could be modeled as a simple *H* and *V* phase-center offset. This is indicated by the fact that the least-squares fit worked well. To calibrate the like-polarized channels relative to the cross-polarized channels, a dihedral or ARC would have

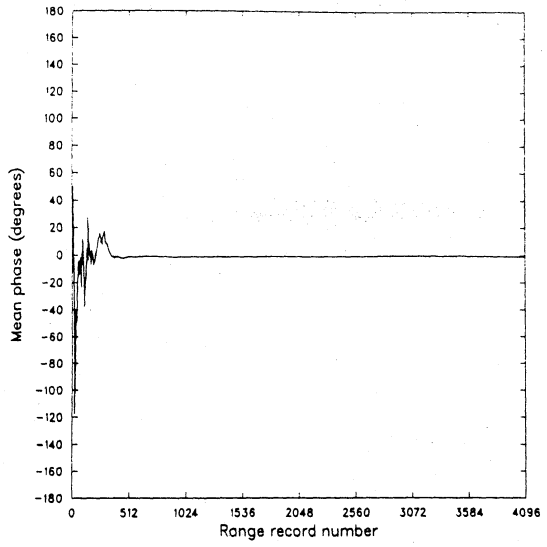

Fig. 6. Average phase differences (*HV-VH*) as a function of the slant range for *X*-band tree-clutter data.

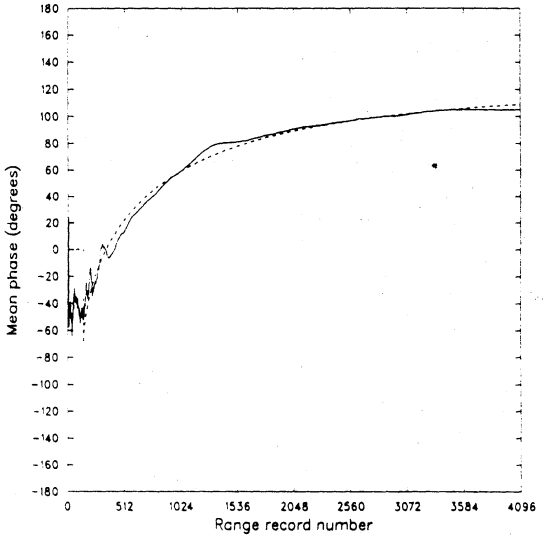

Fig. 7. Average phase difference (*VV-HH*) as a function of the slant range for *X*-band tree-clutter data. The dotted line is a fitted curve assuming that the *H* and *V* antennas have different phase centers.

to be used which had an appropriate scattering matrix [11], [13].

B. C-Band and L-Band Calibration of NASA/JPL SAR

Fig. 8 shows an *L*-band image of the Goldstone Calibration site produced by the NASA/JPL DC-8 Airborne SAR. The image on the left is a color overlap of L_{HH}, L_{VV}, and L_{HV} polarizations, color-coded red, green, and blue, respectively. In the image on the right the grey scale represents total power ($|L_{HH}|^2 + |L_{VV}|^2 + 2|L_{HV}|^2$), while the color indicates the phase difference between the *HH* and *VV* channels. The phase distribution is centered around π and is uniform across the image. This phase distribution has a nonzero mean because it is uncalibrated, but the image can be calibrated. The dark patch near the center of both images is the dry lake bed at Goldstone, California, where an array of corner reflectors and other calibration devices were deployed. The corner reflectors appear as a line of bright points in the image.

Fig. 9 shows a plot of the average *HH/VV* phase difference over the whole swath, calculated by averaging $M_{11}M_{22}^*$ coherently over 1024 points in each range gate, centered in azimuth on the dry lake bed. This measure of the *L*-band *HH/VV* phase difference is uniform across the swath, with a mean value of 158.0° and standard deviation of 4.6°. From this plot we infer that the *H* and *V* antennas have common phase centers (see (22)). The DC-8 and P-3 SAR's do have different-type antennas, so the fact that the DC-8 phase centers are co-located is not surprising. Indeed, this is the ideal.

Figs. 10 and 11 show plots of the phase difference between the *HV* and *HH* channels, and the *HV* and *VH* channels, respectively. The slight phase variation visible in Fig. 11 across the swath could be due to a misregistration between transmit and receive phase centers for the cross-polarized channels, but a more likely cause of the variation across the swath is the contribution of the cross-polarized contamination, which is typically −15 dB down at *L*-band but varies across the swath. The cross-polarized contamination is probably also contributing to the phase plot of arg $\langle M_{21}M_{11}^* \rangle$ in Fig. 10, which varies significantly across the swath. In this case, since we expect the *HV* and *HH* backscatter to be uncorrelated and the phase to be uniformly distributed, we infer that Fig. 10 can be explained by the dominance of the term involving $|a|^2$ in $M_{21}M_{11}^*$. It is this variation of the cross-polarized contamination terms across the swath which is also probably the cause of the phase slope between the *HV* and *VH* channel measurements, visible in Fig. 11. The slope is small, just 0.4°/degree of incidence angle, or 8° across the total swath.

Figs. 12 and 13 show the *HH/VV* and *HV/VH* phase differences for the *C*-band DC-8 SAR image of Goldstone, which was obtained at the same time as the *L*-band image. Both curves are constant across the swath, which suggests that the receive and transmit *H* and *V* antenna phase centers are co-located. Fig. 14 shows a plot of the *HV/HH* phase difference, estimated from arg $\langle M_{21}M_{11}^* \rangle$. The phase difference is fairly uniformly distributed over the first half of the swath. Then the channels appear to become correlated, and the relative phase becomes constant at around 60° for the last half. This is probably due to the fall-off of the cross-polarized backscatter return as the *C* band over the dry lake bed, which, estimated from M_c, is typically −10 dB down from the like-polarized in the first half of the swath where the ground is vegetated versus −30 dB down over the dry lake bed. This is comparable with the level of cross-polarization isolation at the *C* band, which varies between −23 and −30 dB. Thus the fall-off in backscatter over the lake bed will allow the like-polarized returns to dominate the calculation of $M_{21}M_{11}^*$, and (13) is not valid.

Figs. 15 and 16 show the relative phase plots derived from the array of trihedral corner reflectors running across the swath (see Fig. 8) for the *L*- and *C*-bands. The error bars on the plots are derived by assuming that any error on the measurement of phase from

Fig. 8. *L*-band image of the Goldstone calibration site produced by the NASA/JPL DC-8 SAR.

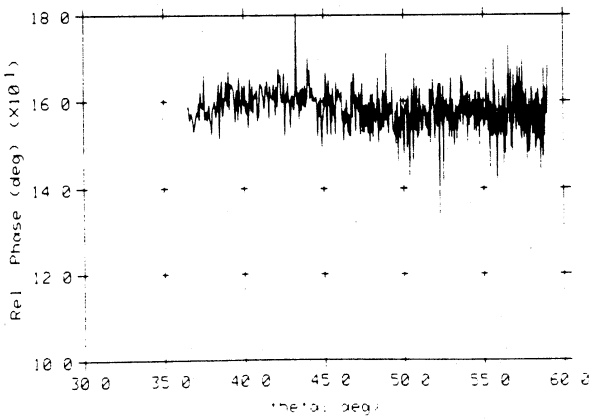

Fig. 9. Plot of the average *HH*/*VV* phase difference over the whole swath for the *L* band. (LHHVV, May 23, 1988, Run 2.)

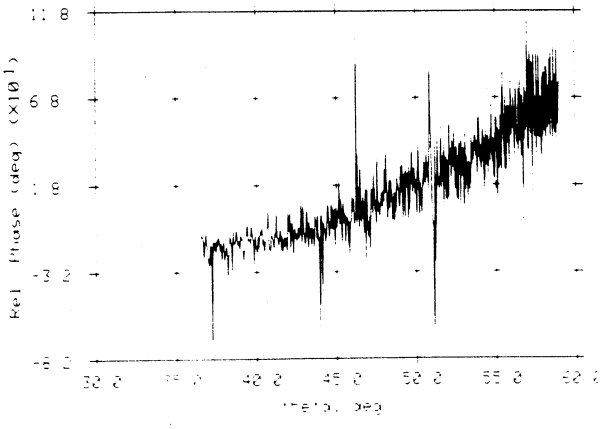

Fig. 10. Plot of the average *HV*/*HH* phase difference over the whole s for the *L* band. (LHVHH, May 23, 1988, Run 2.)

caused by a contribution to the return from the surrounding clutter. The background clutter level was estimated by averaging over a small cell 64 × 64 pixels in extent, located near the reflector array. Worst-case phase errors were assumed, in which the clutter is orthogonal to the point target return in each polarization. It is clear that something other than the clutter background is contributing to the phase estimates. Two other sources of ph error are possible: Phase problems caused by the ra itself, or imperfections in the corner reflector const tion. We suggest the latter cause as the most likely, gi the fairly smooth behavior of the relative phase meas ments derived from the image background.

Results from the corner reflector array and image b

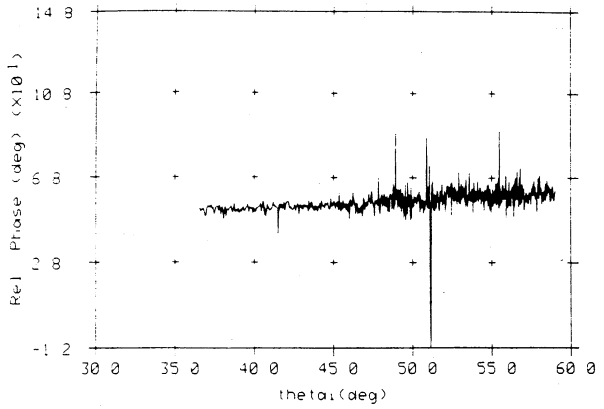

Fig. 11. Plot of the average HV/VH phase difference over the whole swath for the L band. (LHVVH, May 23, 1988, Run 2.)

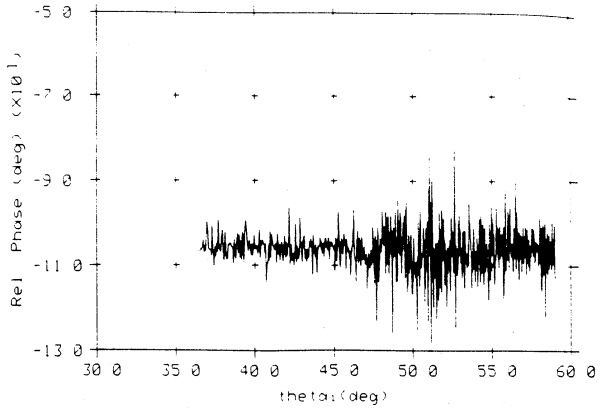

Fig. 13. Plot of the average HV/VH phase difference over the whole swath for the C band. (CHVVH, May 23, 1988, Run 2.)

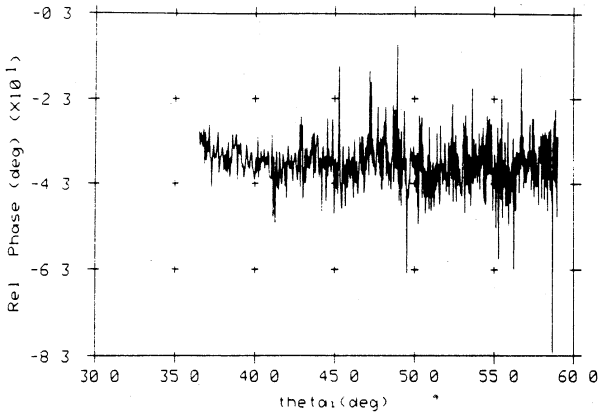

Fig. 12. Plot of the average HH/VV phase difference over the whole swath for the C band. (CHHVV, May 23, 1988, Run 2.)

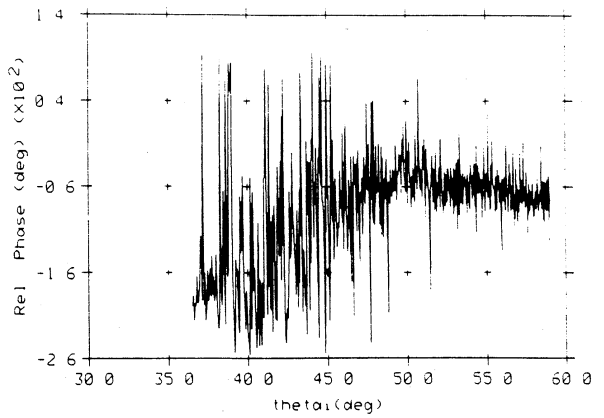

Fig. 14. Plot of the average HV/HH phase difference over the whole swath for the C band. (CHVHH, May 23, 1988, Run 2.)

ground phase measurements are collected together for comparison in Table II. Note the close correspondence between all the corner reflector and background measurements, at both the L- and C-bands. This suggests that either the corner reflector or image background approaches, or combinations thereof, can be used for phase calibration to give similar results. Another point to note from Table II is that none of the HV/HH phase comparisons appear to give a good estimate of the receiver phase difference ϕ_r, as estimated from the HH/VV and HV/VH phase terms, at least for this radar system. We would not expect a good agreement for the corner reflectors, since the cross-polarized measurement is due to the leakage from the like-polarized reflection. Also, the background clutter probably has uncorrelated like- and cross-polarized scatter so that the average phase difference HV/HH is also determined by leakage.

VI. Conclusions

We have examined some of the sources of phase errors in polarimetric SAR systems, using the DC-8 and P-3 SAR systems as examples. The sources of phase error have been examined from a theoretical standpoint by examining the simplified system architectures of both systems. A phase error common to both systems is caused by receiver and transmitter noise and is completely random. This error is small in both systems when the SNR is sufficient. Additional deterministic errors are caused by path length differences in the total transmit to receive channels for the various polarization combinations. For the DC-8 SAR, it could be assumed that the two transmit channels were of a fixed length, and also that the two receive channels were of fixed lengths. For the P-3 SAR only the total path lengths, or sums of the transmit and receive paths, were considered to be constant for the four polarization combinations. Path lengths outside the radar can also cause a phase error if the phase centers of the V and H polarized antennas are offset. This offset can cause a spatially varying phase shift in the image, and the P-3 X-band data was used to illustrate this. Secondly, channel coupling can cause spatially varying phase shifts in measured clutter statistics. This is due to the incidence angle dependence of channel coupling. The NASA/JPL DC-8 SAR C- and L-bands data were used to illustrate some of the effects of channel coupling on the measurement of clutter statistics.

It was demonstrated that methods of calibration using clutter statistics under certain assumptions are quite powerful and that the results agree with the results using calibration reflectors. Assumptions made in this paper were that the scattering was reciprocal ($S_{12} = S_{21}$), that the copolarized components of the scattering were correlated

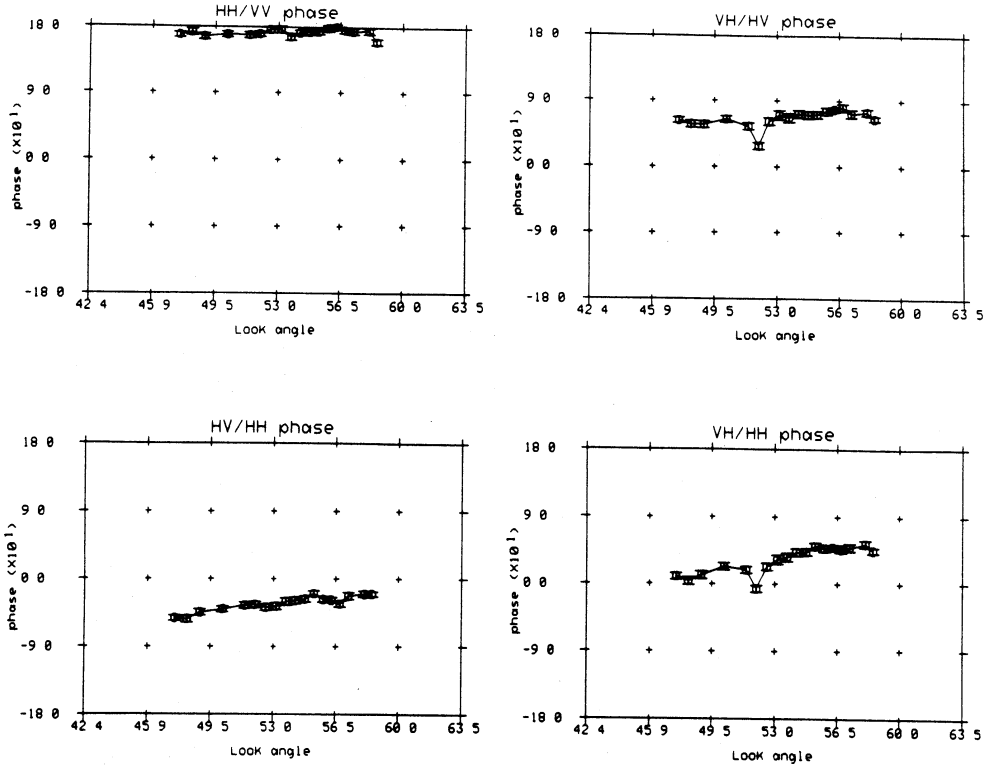

Fig. 15. *L*-band phase plots—derived from trihedral corner reflectors.

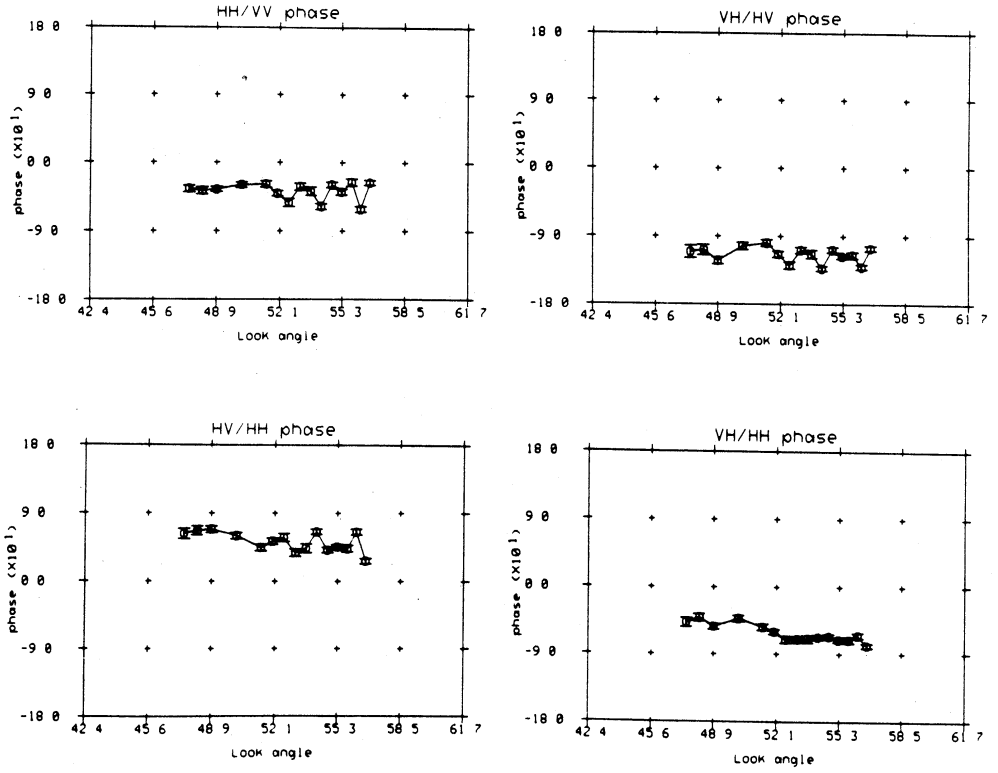

Fig. 16. *C*-band phase plots—derived from trihedral corner reflectors.

($\langle S_{11}S_{22}^* \rangle \neq 0$), that there was significant cross-polarized scattering ($\langle S_{12}S_{12}^* \rangle > 0$), and that the like- and cross-polarized scattering were uncorrelated ($\langle S_{11}S_{12}^* \rangle = 0$). These assumptions are only valid for certain limited types of clutter. So far we have verified the approach for *X*-band scattering from a tree canopy using the P-3 SAR and surface scattering from a dry-lake bed at the *C*- and *L*-bands using the DC-8 SAR. Examples of where the approach isn't valid would be: Scattering from cornstalks at the *L*-band [4], scattering from urban areas, and other similar predominately two-bounce scattering processes. In these cases $\langle S_{11}S_{12}^* \rangle \neq 0$. Also, scenes with low-cross polarized scatter such as ocean scenes would be difficult to use because system leakage could predominate the

TABLE II
COMPARISON OF AVERAGE RELATIVE PHASE (IN DEGREES) ACROSS THE SWATH DERIVED FROM TRIHEDRAL ARRAY AND BACKGROUND CLUTTER FROM GOLDSTONE IMAGE

	HH/VV	HV/VH	HV/HH	ϕ_r **
L-Band				
Corner Reflectors	172.2(± 5.0)*	65.7(±12.0)	32.4(±18.7)	53.3
Background	158.0(± 4.6)	57.5(± 6.2)	22.9(±18.7)	50.3
C-Band				
Corner Reflectors	-38.0(±11.1)	-114.4(±10.2)	-62.14(±11.4)	38.2
Background	-38.4(± 5.9)	-106.3(± 4.8)	-78.8(±59.5)	34.0

* Numbers in brackets are standard deviations taken across the swath.

** Estimates from HH/VV and HV/VH in each row.

cross-polarized scattering and not be negligible. Experimental data also indicates that the pre-nadir and nadir regions in images are not usable.

Results using calibration reflectors appear to be quite consistent with clutter results for both the P-3 and DC-8 systems. One interesting coincidence (we believe) for the DC-8 system is that trihedrals HV/VH phase difference is in agreement with the phase difference calculated by using clutter statistics. This is interesting, since it implies that the channel coupling into the cross-polarized receive channel is in-phase with the actual cross-polarized received signal. This is not in general true and we do not advise using trihedrals to calibrate the HV channel relative to the VH channel.

In this paper the main focus has been on the use of clutter statistics to phase calibrate, as well as on the possible variation of phase calibration with range. Phase calibration using reference reflectors is fairly well understood and has been discussed previously [11], and an example procedure using trihedrals was briefly discussed in Section III-C. A complete procedure to derive all of the elements of the T and R matrices would require at least three different types of reference reflectors, including trihedrals and dihedrals at two orientations [11], or three ARC's in different configurations. The expense and difficulty in deploying many reference targets necessitates the use of clutter statistics as a supplementary tool in phase calibration. With both systems, the deterministic phase errors described in this paper could be removed through proper calibration experiments using clutter and reference reflectors. The calibration procedures for both systems are slightly different because the system architectures are not identical.

ACKNOWLEDGMENT

The research presented in this paper was carried out by both the Environmental Research Institute of Michigan (ERIM) and the Jet Propulsion Laboratory (JPL). The authors would like to thank J. Lydeu and the crew of the P-3/SAR for their efforts in collecting the data used in this study.

REFERENCES

[1] D. N. Held, W. E. Brown, and T. W. Miller, "Preliminary results from the NASA/JPL multifrequency, multipolarization synthetic aperture radar," in *Proc. IEEE Nat. Radar Conf.* (Ann Arbor, MI), Apr. 1988, pp. 7-8.

[2] A. Kozma *et al.*, "Multifrequency-polarimetric SAR for remote sensing," in *Proc. IGARSS '86* (Zurich, Switzerland), Sept. 1986, vol. 1, pp. 715-719.

[3] R. J. Sullivan *et al.*, "Polarimetric $X/L/C$-band SAR," in *Proc. IEEE Nat. Radar Conf.* (Ann Arbor, MI), Apr. 1988, pp. 9-14.

[4] F. T. Ulaby, D. Held, M. C. Dobson, K. C. McDonald, and T. B. A. Senior, "Relating polarization phase difference of SAR signals to scene properties," *IEEE Trans. Geosci. Remote Sensing*, vol. GE-25, pp. 83-92, Jan. 1987.

[5] R. M. Goldstein, H. A. Zebker, and C. L. Werner, "Satellite radar interferometry: Two-dimensional phase unwrapping," *Radio Sci.*, vol. 23, pp. 713-720, July-Aug. 1988.

[6] I. J. LaHaie, A. R. Dias, and G. D. Darling, "Digital processing considerations for extraction of ocean wave image spectra from raw synthetic aperture radar data," *IEEE J. Oceanic Eng.*, vol. OE-9, pp. 114-120, 1984.

[7] R. A. Cordey and J. T. Macklin, "Complex SAR imagery and speckle filtering for ERS-1 wave mode," in *Proc. IGARSS '88* (Edinburgh, UK), Sept. 1988, vol. 1, pp. 387-390.

[8] A. Freeman, J. C. Curlander, P. Dubois, and J. D. Klein, "Shuttle imaging radar—C calibration workshop report," Jet Propulsion Lab., Pasadena, CA, Tech. Rep. 88-003, Nov. 8, 1988.

[9] H. A. Zebker, J. J. van Zyl, and D. N. Held, "Imaging radar polarimetry from wave synthesis," *J. Geophys. Res.*, vol. 92, pp. 683-701, Jan. 1987.

[10] J. A. Kong, *Electromagnetic Wave Theory*. New York: Wiley, 1986.

[11] R. M. Barnes, "Antenna polarization calibration using in-scene reflectors," Lincoln Lab., Lexington, MA, Proj. Rep. TT-65, Sept. 1986.

[12] M. Borgeaud, R. T. Shin, and J. A. Kong, "Theoretical models for polarimetric radar clutter," *J. Electromagn. Waves Appl.*, vol. 1, pp. 73-89, Apr. 1987.

[13] D. R. Brunfeldt and F. T. Ulaby, "Active reflector for radar calibration," *IEEE Trans. Geosci. Remote Sensing*, vol. GE-22, pp. 165-169, Mar. 1984.

[14] R. B. Dybdal and R. H. Ott, "Coherent RF error statistics," *Trans. Microwave Theory Tech.*, vol. MTT-34, pp. 1413-1420, Dec. 1986.

Dan R. Sheen (S'82-M'86) received the B.S. degree (1981) in electrical engineering from Washington State University, Pullman, and the M.S. (1983) and Ph.D. (1987) degrees in electrical engineering from the University of Illinois at Urbana-Champaign.

Currently, he is a Research Engineer in the Radar Science Laboratory at the Environmental Research Institute of Michigan (ERIM), Ann Arbor. Since joining ERIM in 1987, his primary work has been on the calibration and remote-sensing applications of polarimetric synthetic aperture radar. He has participated in numerous airborne data collection experiments and subsequent data analysis activities. During the period from 1981 to 1987 he worked as a Research Assistant in the Ionosphere Radio Laboratory at the University of Illinois at Urbana-Champaign. His research work at the laboratory was in the experimental study and modeling of wave propagation, with application to atmospheric remote sensing problems.

Dr. Sheen is a member of the American Geophysical Union, Phi Kappa Phi, Eta Kappa Nu, and Tau Beta Pi.

Anthony Freeman (M'83) received the B.Sc. (Hons.) degree in mathematics in 1979 and the Ph.D. degree in astrophysics in 1982, both from the University of Manchester Institute of Science and Technology, Manchester, England.

Between 1982 and 1987 he worked at the Marconi Research Centre, Chelmsford, England, on moving target imaging with SAR, aircraft SAR motion compensation, SAR design studies and image quality assessment. Since March 1987 he has been employed by the Jet Propulsion Laboratory, Pasadena, CA, as a radar systems specialist and group leader. His current area of research is in the field of multifrequency, multipolarization SAR calibration.

Dr. Freeman is Chairman of the Committee in Earth Observing Sensor Working Group (CEOS) on SAR Calibration.

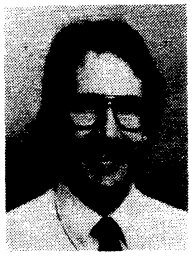

Eric S. Kasischke (A'85-M'88) received the B.S. degree in natural resources in 1974 and the M.S. degree in remote sensing in 1980 from the University of Michigan, Ann Arbor. He is presently a Ph.D. degree candidate at the University of Michigan.

Since 1976 he has worked as a Research Scientist in the Radar Science Laboratory of the Environmental Research Institute of Michigan (ERIM), Ann Arbor. His research activities have concentrated on developing techniques to exploit information collected by imaging radars for both oceanic and terrestrial applications. He has directed numerous airborne data collection experiments and has been involved in the calibration of imaging radars for the past six years.

Mr. Kasischke is a member of Sigma Xi and the American Geophysical Union.

Phase Calibration of Polarimetric Radar Images

DAN R. SHEEN, MEMBER, IEEE, ANTHONY FREEMAN, MEMBER, IEEE, AND
ERIC S. KASISCHKE, MEMBER, IEEE

Reprinted from
IEEE TRANSACTIONS ON GEOSCIENCE AND REMOTE SENSING
Vol. GE-27, No. 6, November 1989

CONNECTING FOREST ECOSYSTEM AND MICROWAVE BACKSCATTER MODELS

Eric S. Kasischke
Radar Science Laboratory
Advanced Concept Division
Environmental Research Institute of Michigan
Ann Arbor, Michigan USA

Norman L. Christensen, Jr.
Department of Botany
Duke University
Durham, North Carolina USA

Accepted for Publication in **International Journal of Remote Sensing**, February 1989.

1.0 INTRODUCTION

The variety of papers presented in this issue is indicative of the substantial research effort underway to evaluate and develop techniques which utilize active microwave remote sensing systems to monitor the earth's forest ecosystems. Hopefully, these efforts, along with similar research programs focusing on visible and infrared remote sensing systems, will lead to a set of algorithms which will constitute the forest ecosystem element of the Earth Observing System (Eos). It is clear that the eventual development of these algorithms will require the close collaboration of forest ecologists, remote sensing modelers and other specialists. The focus of this paper will be on a proposed methodology to connect the forest ecosystem models, which are the desired end product of the Eos process, with the active microwave remote sensing signatures provided by imaging spaceborne synthetic aperture radar (SAR) data. In doing so, it is hoped that a clearer understanding of the rationale behind the development of the theoretical scattering models (see, e.g., Richards et al. 1987; Sun and Simonett 1988; Blanchard **this issue**; Durden et al. **this issue**; Ulaby et al. **this issue**) and the conducting of extensive field measurement programs (see, e.g., Cimino et al. **this issue**; Dobson et al. **this issue**) will evolve.

Methods to utilize the quantitative signatures within a SAR data set as inputs for forest ecosystem models are at a very early stage of development. This relative immaturity stems from two facts: (1) the paucity of calibrated, multifrequency, polarimetric SAR data of forest test sites for use in technique development; and (2) the lack of validated backscatter models which explain the microwave signature from complex forest canopies. The microwave remote sensing community has been without a source of SAR data since 1985, due to the unfortunate demise of the NASA CV-990 aircraft and the JPL SAR, and the decision of the U.S. Navy to re-fabricate the ERIM/CCRS CV-580 SAR System. However, both NASA/JPL and Navy/ERIM have recently finished reconstruction of their airborne SAR systems (Kozma et al. 1986; Sullivan et al. 1988; Held et al. 1988) and data sets are now becoming available to the

forestry/remote sensing community. In addition, significant strides have been made over the past several years in the development of theoretical models of microwave backscatter from forested landscapes (Richards et al. 1987; Sun and Simonett 1988; Ulaby et al. this issue). Thus, the necessary instrumentation and theoretical tools exist for development of techniques necessary to utilize SAR data as inputs into forest ecosystem models. In order to accomplish this goal, however, the proper protocol for linking forest ecosystem and microwave backscatter models must be established.

2.0 REMOTE SENSING/FOREST ECOSYSTEM MODEL STRUCTURE

Figure 1 presents a conceptual flow chart of the relationships between SAR-derived remote sensing signatures and forest ecosystem models. For a given forest stand, there are several dimensions to the radar signature which are available to generate different channels of data to use as inputs into the connecting models, including: (1) radar frequency; (2) the relative phase between the transmitted and received signature (i.e., the polarization of the signature); (3) the radar incidence and azimuth angles; and (4) time. If the forest stand is larger than the resolution cell size of the SAR system, then there will be spatial variability in the radar signature outside of image speckle (caused by spatial variation in stand geometry and physiology), resulting in another dimension to the radar signature, image texture (Kasischke et al. 1987)

The connecting models in Figure 1 represent a set of algorithms which convert the remotely-sensed signatures into parameters used as inputs into the forest ecosystem models. It is important to recognize the connection between the remote sensing signature and the forest ecosystem is being made at the individual tree and forest stand (population) level. Thus, even though higher order forest ecosystem models (e.g., element cycling models, successional models, etc.) may be the desired output, it is through an understanding of the lower order forest ecosystem models that the initial linkages with the remote

sensing signatures will be made (see section 3.0).

The development of connecting models is highly dependent on the microwave backscatter models: these predict the SAR signature as a function of the radar system parameters and the geometry and physiology of the forest canopy being imaged. For a forest ecosystem consisting of a single species of tree, it may be possible to derive an empirically-based model to derive forest parameters from radar imagery (see, e.g., Wu and Sader 1987). However, because of the variations in tree canopy geometry among different tree species, as well as the physiological dynamics of individual trees, such an empirically-derived connecting model may only be applicable for a very narrow range of tree geometries and environmental conditions.

Because of this variability, generalized connecting models can only be developed through the use of a validated set of backscatter models. The proper use of existing tree geometry and tree and population (stand) growth models can provide the information needed for the validation of the backscatter model. This validation process is discussed further in section 4.

The formulation of such connecting models will not be accomplished through a straightforward inversion of the backscatter model. Although exercising of the backscatter model for a variety of tree/stand characteristics may provide the basis for the initial format of the connecting model, the final coefficients of the connecting model will most likely be derived from actual radar data, as is discussed in section 5.

3.0 FOREST ECOSYSTEM MODEL HIERARCHY

A great deal of emphasis has been placed on the potential use of SAR data to predict ecosystem properties of interest (NASA, 1983; National Academy of Sciences, 1985). However, the specific protocols by which such data will be successfully linked to ecosystem models are not explicitly enunciated. In the development of these linkages, it is important to recognize that ecosystem models can be classified in a

hierarchical fashion, ranging from models dealing with the properties of and processes occurring within a single tree to those simulating processes over the entire biosphere (Figure 1). This is by no means a hierarchy of model complexity, rather, these modelling levels differ in the spatial and temporal scales of the inputs and outputs. For programmatic reasons, governmental agencies responsible for the development of satellite remote sensing systems generally discuss ecosystem models at the biosphere level. However, operational linkages between the remote sensing data and the ecosystem models will in most cases be made at the community, population and individual tree levels.

In addition to understanding the forest properties that can be directly measured using remotely sensed data, linkages among the various levels in the ecosystem model hierarchy must also be made in order to use remote sensing data to drive the higher-order models presented in Figure 1. For example, leaf area and soil water characteristics are inputs to simulation models of whole plant photosynthesis and evapotranspiration (Running et al. 1986, Running et al. 1988). Such models predict patterns of net photosynthesis and water use over watershed-size areas and short time intervals in relatively simple ecosystems. Population and stand growth models (e.g. Daniels and Burkhart 1975; Mitchell 1969) are driven by empirically or experimentally determined estimates of growth rate and mortality rate, often in relation to stand density. Changes in composition and structure of groups of species populations can be modelled based on assumptions regarding the component populations and the nature of their interactions (Shugart 1984). The complexity of such models varies in terms of the extent to which they simulate competitive interactions, disturbance cycles, and variations among populations in age structure. Most such models can be initialized based on species population data (e.g., density and size) and parameterized from equations of varying complexity that predict tree establishment, growth, and mortality. Changes in forest tree populations are often major determinants of ecosystem-level processes such as carbon and nitrogen cycling. Thus, simulation models of such processes may be directly connected to

community-level models (e.g. Pastor and Post 1985, 1986, Pastor and Huston 1986). Regional and global scale forest models have been used to predict the impact of forests on very large scale processes such as atmospheric carbon flux (Moore et al. 1981, Houghton et al. 1983).

Such a model classification is, of course, arbitrary, but it focuses our attention on four important facts: (1) remotely-sensed data are most directly relevant to forest properties that are inputs to lower-level (i.e., tree, population, and community) models; (2) the forest characteristics which can be directly estimated from remotely-sensed data are often a small subset of those needed for the forest ecosystem models we wish to parameterize; (3) to successfully utilize remotely-sensed data to drive higher-level models, linkages must be established among models that take advantage of the parameters actually provided by the remote sensing systems via the connecting models; and (4) given the complexity of forest ecosystems, no single remote sensing system (e.g., passive optical or active microwave) will likely be adequate to provide all of the inputs the necessary inputs to forest ecosystem models.

To illustrate the problems posed here, assume that our goal is to estimate carbon flux from a large forested landscape such as the piedmont and coastal plain of the southeastern United States. Given the importance of natural and human-caused disturbance on such landscapes, variations among forest stands in carbon flux are to a large degree related to variations in successional stage. Trajectories of change in potentially directly-sensible forest features such as green leaf area index (GLAI), stem density, biomass or tree size are often non-linear or even multi-modal (see Figure 2). Thus, successional change cannot be inferred from such features individually.

For example, from Figure 2 it is evident that variation in GLAI early in succession is highly correlated with tree growth and forest carbon flux. The ability of optical remote sensing systems to detect variations in GLAI has been clearly demonstrated. However, GLAI peaks early in succession and subsequently is uncorrelated with carbon flux. Although major changes in forest biomass and carbon flux may occur

subsequent to this peak in GLAI, such changes will not be detectable using optical sensors.

However, utilizing population-level models, biomass/density data generated from active microwave remote sensing instruments may be used to infer structure in the middle to old age stands. Such structural information, in conjunction with a firm understanding of the dynamics of the tree populations, can be used to drive community-level models of successional change. These may, in turn, provide the inputs for models of patterns of carbon cycling and carbon flux.

The succession/carbon flux models developed for forests to date require some inputs that we will not likely be able to estimate using remote sensing systems. These include site hydrologic characteristics and biochemical characteristics of the forest floor (see Running et al. 1988). In order to utilize remotely-sensed data to drive carbon forest flux models for an entire landscape, we must be able to infer these characteristics from those data, or supplement our data set utilizing other sources of information (such as geographic information systems).

4.0 BACKSCATTER MODEL DEVELOPMENT

To develop models which can explain microwave scattering from forest canopies, it is necessary to determine what canopy parts are responsible for the backscattering of the microwave energy transmitted by a SAR system. The size, shape, distribution, and dielectric properties of the individual tree constituents (i.e., the leaves, reproductive organs, branches, stems and boles) are primary determinants of the radar signature. To a first approximation, those structures whose dimensions are less than a radar wavelength act primarily as attenuators of microwave energy, those structures whose dimensions are larger than a radar wavelength act as scatterers of microwave energy, and the attenuation/scattering of the structure will be directly proportional to the dielectric constant of the plant material.

The plant material within a forest canopy can be divided into two parts: plant tissue and plant fluid. From measurements at a frequency

of 1.2 GHz (Ulaby et al. 1986; Dobson 1988) it is known that:

$$\epsilon_V = 3.0 - j0$$
$$\epsilon_{WV} = 18.0 - j6$$

and

$$\epsilon_f = 72 - j25$$

where ϵ_V is the dielectric constant of the dry vegetation matter, ϵ_{WV} is the dielectric constant of wet vegetation, and ϵ_f is the dielectric constant of the plant fluid. Thus, the major source of scattering and attenuation from a forest canopy is the plant fluids which are suspended above the ground by the plant tissues. In other words, the radar signature is a function of the distribution of wet aboveground biomass, and it is the size, shape and distribution of the aboveground biomass elements of a tree, and the dielectric properties of these elements which define the primary inputs for the backscatter model. This fact is illustrated in Figure 3, which presents a schematic diagram of the inputs for the Michigan Microwave Canopy Scattering (MIMICS) model (Ulaby et al. **this issue**).

Validation of a microwave backscatter model can be thought of as a two-step process. First, the model needs to be validated for a stationary condition, i.e., the case where there are no temporal variations (such as diurnal changes in tree fluid content due to moisture stress, seasonal variations in plant biomass, etc.) in the forest canopy . This initial validation step is used to study changes in the microwave signature owing to variation in the overall canopy structure. The second step is validation of the backscatter model for canopy dynamics, i.e., temporal variations in canopy biomass and fluid content. To provide the data for validation of the backscatter models for the stationary case, a set of test sites must be identified which vary in aboveground biomass distribution. To study the dynamic case, several of the test sites have to be monitored over a period of time.

If the tree parameters in Figure 3 must be measured individually over an entire growing season, then validation of the backscatter models

using actual forest ecosystems represents a truly formidable task. However, if test sites are selected where the forest ecosystems have been studied and modeled, then existing tree and stand growth models may provide the input parameters needed for exercising and validation of the backscatter models. In the following sections, we will first discuss a prototype forest ecosystem that can be utilized for studying the connections between backscatter and forest ecosystem models. This will be followed by a discussion of how tree and stand growth models for this prototype forest ecosystem can be used in validation of the backscatter model for the stationary condition. Finally, we will discuss how a different set of tree and stand growth models can be used for validation of the backscatter model for the dynamic scene condition.

4.1 OLD-FIELD LOBLOLLY PINE FORESTS

In this paper we will utilize old-field loblolly pine (Pinus taeda L.) forests found in the southeastern United States as a prototype forest ecosystem. Christensen and Kasischke (1987) discuss the important characteristics of the old-field loblolly pine forest ecosystems with respect to microwave remote sensing studies. In summary, loblolly pine stands offer an ideal prototype for use in studies connecting microwave backscatter and forest ecosystem models because: (1) they have been well studied, and numerous tree and stand growth models and forest ecosystem models exist; (2) the pure stands of loblolly pine represent both a simple tree structure and a simple stand structure, which minimizes the complexity in deriving the inputs for the backscatter models; (3) such ecosystems are widespread, offering numerous test sites for use in remote sensing studies; and (4) numerous stands at different stages of the successional sequence exist, providing a wide variety of forest stand densities, tree diameters, and tree heights for evaluation of the backscatter models.

Therefore, tree and stand growth models exist for loblolly pine forests, or can be developed based upon existing data or data which can be readily obtained due to the widespread availability of test sites.

In turn, these test sites can be used to validate the microwave backscatter model for both the static and dynamic scene cases.

4.2 THE STATIONARY CASE

Because different loblolly pine stands found over a regional landscape were established at widely varying times, these different stands represent the successional chronosequence for loblolly pine. Although there are potential pitfalls in assuming differences among stands of varying age are a simple consequence of succession (Pickett 1988), abundant long-term studies in these ecosystems provide confidence in such comparisons (Peet and Christensen 1987). Figure 2 presents the general trend of changes in the major tree characteristics which influence the total aboveground biomass during secondary forest succession for old-field loblolly pine, and hence the radar remote sensing signature. Both axes on this graph represent only relative scales, which vary both as a function of site conditions and initial stocking densities.

Since individual stands established at the same point in time have different site conditions, as well as different initial stocking densities, loblolly pine stands found over a large region typically have considerable variation in the amounts and distribution of aboveground biomass (i.e., in the stem density, height, and diameter, and GLAI etc. within the stand). Thus, a radar data set gathered over a number of these stands offers the diversity in stand biomass and geometry required to validate the backscatter models.

A general list of forest parameters needed to validate such backscatter models is given in Figure 3, and Table 1 lists all the loblolly pine characteristics which are needed to validate a backscatter model such as MIMICS. We can divide the tree characteristics in Table 1 into three general categories: (1) those characteristics that are easily measured from the ground or that are assumed to be fairly constant throughout the stand; (2) those characteristics measured for a specified number of trees within the stand, which form the basis for equations

that are applied to the rest of the trees within the stand; and (3) those characteristics estimated using existing tree/stand growth models.

For the first category, we assume that the characteristics are being sampled sufficiently to provide a statistical description of the characteristic for the entire stand. The second category of tree characteristics represents those which are more difficult to measure directly from the ground or those for which no tree/stand growth models exist. These parameters will have to be estimated using allometric equations that predict parameter values based on more easily measured variables. For example, tree height can be estimated based on tree diameter and stand density. The third category of variables are those for which tree/stand growth models already exist. These models primarily deal with the amount and vertical distribution of biomass within the tree crown (Christensen 1988; Kinerson et al. 1974; Hepp and Bristler 1982; Nehmeth 1971; Peet and Council 1982; Clark and Taras 1976; Labyak and Schumacher 1954) and the shape or taper of the tree bole (Burkhart and Walton 1985; Byrne and Reed 1986).

Loblolly pines exhibit a high degree of self-pruning, with the living branches being limited to the upper portion of the canopy, and the dead branches below this region falling off the tree. As illustrated in Figure 4, the canopy depth for loblolly pine stands follows a predictable trajectory based upon initial stocking density and stand age. The lines in Figure 4 represent different stands with different initial stocking densities. Each stand started out with a high stem density, which decreases with age as stem mortality occurs. As density decreases, canopy depth decreases in a predictable manner. Thus, a model can be developed which predicts crown depth based upon stem density. If the tree height (h) and crown depth (d_c) are known, then it is possible to estimate the crown ratio (C_r) as

$$C_r = [(h - d_c) / h] \times 100. \quad (1)$$

Models exist (Kinerson et al. 1974; Hepp and Bristler 1982; Nehmeth 1971; Peet and Council 1982) which predict total crown weight, total

branch weight and total needle weight as a function of tree diameter and crown ratio. Figure 5 (after Hepp and Bristler 1982) shows the relationship of crown weight, branch weight and needle weight as a function of crown ratio for a fixed tree diameter. Figure 6 illustrates the trend in the proportion of branch weight and needle weight as a function of tree diameter.

It is also important to determine the distribution of the total biomass in the crown. Although some of this information will be provided via direct measurements, some can also be provided from the growth models (Kinerson et al. 1974; Hepp and Bristler 1982), as illustrated in Figure 7.

In summary, models exist or can be readily developed for loblolly pine stands to estimate difficult to measure parameters based upon other characteristics which can be easily obtained. Once a set of these models has been derived, it should be possible to generate an input data set for a large number of different stands for validation of the backscatter model.

4.3 THE DYNAMIC CASE

If the backscatter models are going to be useful for predicting signatures for other geographic regions at different times of the year, then changes in the loblolly pine stand characteristics due to regional (i.e., site) or temporal events must be accounted for. There are subtle physiological variations in tree structure due to genetic responses to climate variations. For example, Zobel and Rhodes (1956) illustrated that the specific gravity for loblolly pine bole wood ranged from 0.358 to 0.486, and the specific gravity for branch wood ranged from 0.328 to 0.692. Thames (1963) showed clear differences in needle structure and composition between pines located in drought-prone regions and those from non-drought areas. These variations need to be expressed in terms of the characteristics used as inputs into the backscatter models in order to determine their effects on the radar signature from the loblolly pine stands.

There are four types of temporal, physiological changes within a loblolly pine forest that may influence the radar signature: (1) diurnal or seasonal variations in the relative water content of the vegetation; (2) variations in total needle biomass; (3) growth of new stems; and (4) growth of reproductive organs. Development of a generalized connecting model requires a backscatter model which can predict change in the microwave signature due to these temporal variations.

Recent experimental work by Dobson et al. (**this issue**) has shown there can be substantial diurnal variation in the radar intensity signature of a single tree stand (3 to 5 dB). The most likely explanation for these observed changes was diurnal variation in the state of the water in the leaves, branches, and boles of the trees in response to moisture stress. Loblolly pine trees are known to have similar diurnal variations in plant moisture (Figure 8, Hodges and Lorio 1971). It may be possible to develop a generalized model which predicts diurnal changes in both relative water content of the needles and water potential within the trunk for loblolly pines based upon meteorological data (i.e., rainfall and temperature). Such models have been developed for other pine species (Running 1984, Running et al. 1988).

Several models have been developed to predict seasonal variations in total needle biomass (Kinerson et al. 1974; Clark and Taras 1976; Labyack and Schumacher 1954). Figure 9 (after Kinerson et al. 1974) depicts seasonal variation in total needle biomass over an entire growing season, while Figure 10 (also after Kinerson et al. 1984) presents the vertical distribution of this biomass as a function of time based on such a model. As can be seen from Figure 9, there is almost two-fold variation in total needle biomass over a single growing season.

New stem growth or branch flushing should have a significant impact on the radar signature. For loblolly pine trees less than 20 years old, new stem height growth averages between 0.5 and 1.2 meters per year, depending on site conditions. For loblolly pine trees between 20 and 50 years old, new stem growth averages between 0.15 to 0.45 meters per year (Gaiser 1950). This growth occurs in 2 to 5 flushes (i.e., growth

spurts) per growing season, depending on site conditions and climatic conditions.

The final temporally-varying growth event which may influence the radar signature from a loblolly pine forest is the growth of the pine cones on the trees. Mature loblolly pine cones are distributed on the end of the pine branches and are up to 9 cm in length. However, these cones take three years for development and maturation, and the number of cones reaching maturity during the third year is highly variable (Dewers and Moehring 1971; Wenger 1957; Grano 1957).

To develop a backscatter model which can adequately account for these temporal variations, it will be necessary to conduct experiments in which radar data are collected over time periods sufficiently long to encompass these events at a sufficient frequency to track the trajectory of change. For example, diurnal measurements will be necessary to monitor moisture stress, whereas measurements will need to be made over entire growing seasons to determine the impact of changes in new stem, cone, or needle biomass on SAR signatures. Once these data have been collected and used to validate the backscatter models, then the models can be exercised over the expected range of conditions (as predicted by the loblolly pine growth models) to determine the influence of such temporal variations on radar signatures. The influence of such temporal changes can then be factored into the connecting models developed for the loblolly pine forest ecosystems.

5.0 DEVELOPMENT OF CONNECTING MODELS

After their validation, a sensitivity analysis can be performed using the backscatter models to determine which forest stand characteristics significantly influence the radar signatures. The results of one such partial sensitivity analysis using the MIMICS model are presented in Figures 11 and 12. These were generated using the characteristics of pure stands of bigtooth aspen (Populus grandidentata) located in the northern portion of the lower peninsula of Michigan (average stand characteristics: tree height: 8 m; density; 1110

stems/acre; dbh: 24 cm; trunk dielectric constant: 15 - j5; leaf area index: 4.7).

Developing a set of algorithms to generate the required inputs for the ecosystem models from the remote sensing signature requires careful consideration of the results of the sensitivity analyses performed using the backscatter model as well as the requirements of ecosystem models. The parametric exercising of the backscatter models should be conducted to consider those forest characteristics which are potential inputs to the ecosystem models of interest. If sensitivity analyses indicate that a variation in a required ecosystem model input results in a discernable trend within the radar signature, then an algorithm to extract that forest characteristic from the radar data can be devised.

The modeling results indicate that VV-polarized channels of the radar are more sensitive to changes in the tree characteristics (Figures 11 and 12). In the absence of any corresponding SAR or radar data to compare with these model results, we cannot make any definitive statement as to the validity of the model. However, if we assume the MIMICS model has been validated, then the results from the VV channel of data can be used in the development of a connecting model between the radar observations and a forest ecosystem model.

In order to explore this connecting model development, let us consider the problem of estimating total aboveground biomass for bigtooth aspen example (see data in Figures 11 and 12). Total aboveground biomass for an individual tree, B_m, can be expressed as

$$B_m = B_t + B_b + B_l \qquad (2)$$

where B_t is the biomass of the tree trunk, B_b is the biomass of the tree branches, and B_l is the biomass of the leaves. The biomass of an individual tree may be related to the biomass of a stand of trees from which a signature is derived. To calculate trunk biomass for an entire stand of trees it may be necessary to derive a biomass term such that

$$B_t = f(\text{density, diameter, height}) \qquad (3)$$

and develop a separate equation for each of the terms in Eq. (3).

The sensitivity analysis using the backscatter model allows determination of which radar channels are most sensitive to each of the parameters in Eqs. (2) and (3). As is illustrated in Figure 12, it appears that variations in the bole density, diameter and height characteristics are best detected in the L-VV and C-VV channels, whereas the X-VV channel is most sensitive to changes in the leaf biomass (which is directly correlated to leaf area index). Based on the shape of the curve (i.e., linear, exponential, quadratic, etc.), an expression which relates the biomass signature of interest to the specific radar channels may then be derived.

Using Figure 12 as an example, a relationship between (L-VV) and tree height, h, might be constructed as

$$h = a + (L\text{-}VV)^b \tag{4}$$

where the terms a and b are determined via least squares regression techniques. In the example in Figure 11, $a \simeq -5$ and $b \simeq 0.9$. However, it should be recognized that the total L-VV signature will vary as a function of other forest characteristics, such as leaf area index and tree density. Therefore, in order to account for these variations, additional terms will have to be added to Eq. (4), and the final version of Eq. (4) may be of the form

$$h = a + (L\text{-}VV)^b + (C\text{-}VV)^c + (X\text{-}VV)^d \tag{5}$$

where the C-VV and X-VV channels were selected because they were sensitive to changes in leaf area index and stem density, respectively, and c and d are coefficients determined by least-squares regression techniques.

Upon completion of the derivation of the initial connecting model based upon the results of the sensitivity analysis, actual radar data from the test sites used to validate the backscatter model can be used

to refine the coefficients of the connecting model. Finally, the precision of the connecting model can be evaluated using additional test sites from the study area. The generality of such models can be measured using test sites at outside of the original area. The end product will be a family of models which utilize specific remotely-sensed signatures to predict forest features relevant to ecological models (or vice versa).

The modeling process described above is sufficient to define the stationary forest characteristics/properties of interest over the landscape of interest. For instance, we may be able to estimate aboveground biomass (standing crop), stand density or GLAI for bigtooth aspen forests. However, if the goal is to measure or predict forest processes such as primary production, carbon flux, evapotranspiration, or nitrogen cycling, additional modeling steps are required, as discussed in section 3. For example, a succession model such as FORET (Shugart 1984) might be used to estimate biomass change from tree size and density data. Many of these process models were not explicitly developed to be driven by the forest data directly provided by remotely sensors. Some models require inputs that are not likely to be obtained by remote sensing. For example, most forest hydrologic models require input of information on soil characteristics. Thus, such models may require extensive modification to make effective use of the data remote sensors provide.

6.0 CONCLUSIONS

We have outlined a procedure to develop a set of algorithms to relate microwave remote sensing signatures to forest ecosystem models. This process is dependent on a validated remote sensing model which describes microwave scattering from a forest canopy. The validation of the backscatter model itself can be greatly facilitated through the use of forest tree/stand growth models to provide inputs for the backscatter model.

In summary, the following steps are followed in the overall

development of a forest ecosystem model which utilizes remote sensing-derived parameters as inputs:

1. Utilizing tree/stand growth models and actual ground-based radar and SAR measurements, develop and validate microwave backscatter models which predict the radar signature as a function of radar system parameters and tree stand characteristics.

2. Parametrically exercise the validated backscatter models to determine which desired forest stand characteristics are most influential on the radar signature.

3. Based on the above sensitivity analysis, identify which forest ecosystem input parameters can potentially be provided from the SAR data set.

4. Develop the connecting models to provide the inputs for the forest ecosystem models.

5. Reconfigure the forest ecosystem models so that they utilize the remote sensing estimates from the connecting models as their primary inputs and identify the sources for the remaining inputs.

7.0 ACKNOWLEDGEMENTS

The methodology presented in this paper was developed under funding provided by the National Aeronautics and Space Administration (NASA) under Grants No. NHEW-1339 to Duke University and Grant Nos.NASW-4360 and NAGW-1101 (under subcontract to the University of Michigan) to the Environmental Research Institute of Michigan. The authors would like to thank M. Craig Dobson of the University of Michigan for providing outputs of the MIMICS model for inclusion in this paper. Many of the ideas presented in this paper were the direct result of concepts which evolved during numerous round-table discussions with a group of scientists loosely organized under the banner of the International Forest Investigation Team or IFIT. The authors would like to acknowledge the contribution of these discussions to this paper. Special thanks go to JoBea Cimino of the Jet Propulsion Laboratory,

8.0 REFERENCES

Blanchard, A., 1989, Identification of Forest Information in Radar Signatures Identified Through Measurements, **Int. J. Remote Sensing** (this issue).

Burkhart, H.E. and S.B. Walton, 1985, Incorporating Crown Ratio into Taper Equations for Loblolly Pine Trees, **Forest Sci., 31**, 478-484.

Byrne, J.C. and D.D. Reed, 1986, Complex Compatible Taper and Volume Estimation Systems for Red and Loblolly Pines, **Forest Sci., 32**, 423-443.

Christensen, N.L., 1988, Analysis of Duke Forest Permanent Plots: Patterns of Production and Mortality of Seedlings and Trees, in **Forest Response Program Annual Meeting - Project Status Reports, Vol. 1**, NCSU Atmospheric Research Program, Raleigh, NC, 85-89.

Christensen, N.L., Jr. and E.S. Kasischke, 1987, The Use of Active Microwave Remote Sensors in Forest Ecology Studies, **Proc. 1987 Inter. Geosci. Remote Sens. Symp.**, Ann Arbor, MI, 457-466.

Cimino, J.B., J. Paris, D. Casey, F. Ahern, N. Christensen, M.C. Dobson, D. Gates, F. Ulaby, J. Weber, R. Hoffer, M. Imhoff, E. Kasischke, A. Milne, J. Richards, A. Sieber, P. Churchill, D. Simonett, C. Slaughter and L. Viereck, 1989, The Effect of Changing Environmental Conditions on Microwave Signatures of Forest Ecosystems, **Int. J. Remote Sensing** (this issue).

Clark, A. III, and M.A. Taras, 1976, Comparison of Aboveground Biomass of Four Major Southern Pines, **Forest Products Journal, 26**, 25-29.

Daniels, R.F. and H.E. Burkhart, 1975, **Simulation of Individual Tree Growth and Stand Development in Managed Loblolly Pine Plantations**, Virginia Polytechnic Institute, Blacksburg, VA.

Dewers, R.S. and D.M. Moehring, 1971, Effect of Soil Water Stress on Initiation of Ovulate Primordia in Loblolly Pine, **Forest Sci., 16**, 219-221.

Dobson, M.C., Diurnal and Seasonal Variation in the Microwave Dielectric Constant of Selected Trees, 1988, **Proc. Int. Geoscience and Remote Sens. Symp.**, Edinburgh, Scotland, 1754.

Dobson, M.C., J.F. Paris, F.W. Ulaby and K. McDonald, Status of Radar Scatterometer Measurements Over Forested Areas, **Int. J. Remote Sensing** (this issue).

Durden, S.L., J.J. van Zyl, and H.H. Zebker, 1989, Polarimetric Radar Forest Signatures, **Int. J. Remote Sensing** (this issue).

Grano, C.X., 1957, Indices to Potential Cone Production of Loblolly Pine, **Jour. Forestry, 55**, 890-891.

Held, D.N., W.E. Brown, and T.W. Miller, 1988, Preliminary Results from the NASA/JPL Multifrequency, Multipolarization SAR, **Proc. 1988 IEEE Radar Conf.**, 7-8.

Hepp, T.E. and G.H. Bristler, 1982, Estimating Crown Biomass in Loblolly Pine Plantations in the Carolina Flatwoods, **Forest Sci., 28**, 115-127.

Hodges, J.D. and P.R. Lorio, Jr., 1971, Comparison of Field Techniques for Measuring Moisture Stress in Large Loblolly Pines, **Forest Sci., 17**, 220-223.

Houghton, R.A., J.E. Hobbie, J.M. Mellilo, B. Moore, III, B.J. Peterson, G.R. Shaver and G.M. Woodwell, 1983, Changes in the Carbon Content of Terrestrial Biota and Soils Between 1860 and 1980: A Net Release of CO_2 to the Atmosphere, **Ecol. Monogr., 53**, 235-262.

Kasischke, E.S., A.L. Maffett and R.W. Larson, 1987, Statistical Modeling of Speckle Distributions on Airborne SAR Imagery, **Proc. 1987 Inter. Geosci. Remote Sens. Symp.**, Ann Arbor, MI, 1357-1362.

Kinerson, R.S., K.O. Higginbotham and R.C. Chapman, 1974, The Dynamics of Foliage Distribution within a Forest Canopy, **J. Appl. Ecol., 11**, 347-353.

Kinerson, R.S., C.W. Ralston, and C.G. Wells, 1977, Carbon Cycling in a Loblolly Pine Plantation. **Oecologia 29**, 1-10.

Kozma, A., A.D. Nichols, R.F. Rawson, S.J. Shackman, C.W. Haney and J.J. Shanne, Jr., 1986, Multifrequency, Multipolarization SAR for Remote Sensing, **Proc. IGARSS '86 Symposium**, Zurich, Switzerland, Ref. ESA SP-254, 715-719.

Labyak, L.F. and F.X. Schumacher, 1954, The Contribution of Its Branches to the Main-Stem Growth of Loblolly Pines, **J. Forestry, 52**, 333-337.

Mitchell, K.J., 1969, Simulation of Growth of Even-Aged Stands of White Spruce, **Yale School of Forestry Bull 75**, 48 p.

Moore, B. R.D. Boone, J.E. Hobbie, R.A. Houghton, J.M. Melillo, B.J. Peterson, G.R. Shaver, C.J. Vorosmarty, and G.M. Woodwell, 1981, A Simple Model for Analysis of the Role of Terrestrial Ecosystems in the Global Carbon Budget, in B. Bolin (ed.), **Carbon Cycle Modeling, Scope 16,** John Wiley and Sons, New York.

NASA, 1983, Strategy for Earth Science Issues, Land-Related Global Habitability Sciences Working Group, **NASA Technical Memorandum 85841**, Washington, D.C., 112 p.

National Academy of Sciences, 1985, **A Strategy for Earth Science from Space in the 1980'2 and 1990's - Part II: Atmosphere and interactions with Solid Earth, Oceans and Biota,** National Academy Press, Washington, D.C., 194 p.

Nehmeth, J.C., 1971, Dry-Matter Production in Young Loblolly (Pinus Taeda L. and Slash (Pinus Elliottii Englm.) Plantations, Ph.D. Dissertation, North Carolina State University, 75 p.

Pastor, J. and M. Huston, 1986, Predicting Ecosystem Properties from Physical Data: A Case Study of Nested Moisture-Climatic Gradients Along the Appalachian Chain, in **Coupling of Ecological Studies with Remote Sensing; Potentials at Four Biosphere Reserves in the United States,** ed. by M.I. Myer and D.A. Crossley, Jr., 82-95, U.S. Department of State Publication 9504.

Pastor, J. and W.M. Post, 1985, Development of a Linked Forest Productivity-Soil Process Model, ORNL/TM-9519, Oak Ridge National Laboratory, Oak Ridge, TN.

Pastor, J. and W.M. Post, 1986, Influence of Climate, Soil Moisture, and Succession on Forest Carbon and Nitrogen Cycles, **Biogeochem., 2,** 3-27.

Peet, R.K. and N.C. Christensen, 1987, Competition and Tree Death, **Bioscience, 37,** 586-595.

Peet, R.K. and O.P. Council, 1982, Rates of Biomass Accumulation in North Carolina Piedmont Forests, unpublished report to the North Carolina Energy Institute.

Pickett, S.T.A., 1988, Space-for-Time Substitution as an Alternative to Long-Term Studies, **Proc. Cary Conference II** (in press).

Richards, J.A., G-Q. Sun and D.S. Simonett, 1987, L-band Radar Backscatter Modeling of Forest Stands, **IEEE Trans. Geosci. Remote Sens., 25,** 487-498.

Running, S.W., 1984, Documentation and Preliminary Validation of H2OTRANS and DAYTRANS, Two Models for Predicting Transpiration and Water Stress in Western Coniferous Forests, **U.S.D.A. For. Serv. Res. Pap. RM-252.**

Running, S.W., D.L. Peterson, M.A. Spanner, and K.B. Teuber, 1986, Remote Sensing of Coniferous Forest Leaf Area, **Ecol., 67,** 273-276.

Running, S.W., R.R. Nemani, D.L. Peterson, L.E. Band, D.F. Potts, L.L. Pierce and M.A. Spanner, 1988, Mapping Regional Forest Evapotranspiration and Photosynthesis by Coupling Satellite Data with Ecosystem Simulation, **Ecology** (in press).

Shugart. H.H., 1984, **A Theory of Forest Dynamics: The Ecological Implications Forest Succession Models,** Springer-Verlag, New York, 278 p.

Sullivan R., A. Nichols, R. Rawson, C. Haney, F. Darreff, and J. Schanne, Jr., Polarimetric X/L/C-band SAR, 1988, **Proc. 1988 IEEE Radar Conf.,** 9-14.

Sun, G-Q. and D.S. Simonett, 1988, Simulation of L-band HH Microwave Backscattering from Coniferous Forest Stands: A Comparison with SIR-B Data, **Photogrammetric Eng. and Remote Sensing, 54,** 1195-1201.

Thames, J.L., 1963, Needle Variation in Loblolly Pine from Four Different Geographic Seed Sources, **Ecology, 44,** 168-169.

Ulaby, F.T., R.K. Moore and A.K. Fung, 1986, **Microwave Remote Sensing, Active and Passive-Volume III: From Theory to Application,** Artech House, Inc., Dedham, MA, 1097 pp.

Ulaby, F.T, K. Sarabandi, K. McDonald, M. Whitt, and M.C. Dobson, Modeling Microwave/Tree Interactions Paper, **Int. J. Remote Sensing,** this issue.

Wenger, K.F., 1957, Annual Variation in the Seed Crops of Loblolly Pine, **Jour. Forestry, 55,** 567-569.

Wu, S-T. and S.A. Sader, Multipolarization SAR Data for Surface Feature Delineation and Forest Vegetation Characterization, **IEEE Trans. Geosci. Remote Sens., GE-25,** 67-76, 1987.

Zobel, B.J. and R.R. Rhodes, 1957, Specific Gravity Indices for Use in Breeding Loblolly Pine Trees, **Forest Sci., 3,** 281-285.

TABLE 1
LOBLOLLY PINE CHARACTERISTICS REQUIRED FOR
INPUTS INTO MICROWAVE BACKSCATTER MODEL*

TREE CHARACTERISTIC	SOURCE
Average tree diameter (dbh)	Measured directly
Average tree density/acre (d_t)	measured directly
Average tree height (h)	Measured directly and allometric equations
Dielectric constants of bole, branches and needles	measured directly
Litter depth and surface roughness	measured directly
Litter dielectric properties	measured directly
Average height to first branch whorl (h_b)	Christensen 1988. Measured directly on selected sites, allometric equations
Crown ratio (C)	Allometric equations, or h_b/h
Main stem taper ratio (t_r)	Burkhart and Walton 1985 Byrne and Reed 1986
Total crown weight (TWT)	Kinerson et al. 1974 Hepp and Bristler 1982
Total branch weight (BWT)	Hepp and Bristler 1982 Nehmeth 1971 Peet and Council 1982
Total needle weight (NWT)	Kinerson et al. 1974 Clark and Taras 1976 Labyak and Schumacher 1954 relationships further established with direct measurements

*Variables which will be measured directly are indicated. References indicate sources of allometric equations to predict a given variable.

TABLE 1
LOBLOLLY PINE CHARACTERISTICS REQUIRED FOR
INPUTS INTO MICROWAVE BACKSCATTER MODEL (Concluded)*

TREE CHARACTERISTIC	SOURCE
Average aboveground tree biomass (B_m)	Nehmeth 1971 Peet and Council 1982 Clark and Taras 1976
Total number of branch whorls (BW)	relationships established with direct measurements
Stems/branch whorl (S_{bi})	relationships established with direct measurements
Average horizontal branch angle/whorl (θ_i)	relationships established with direct measurements
Average distance between branch whorls (d_i)	relationships established with direct measurements

*Variables which will be measured directly are indicated. References indicate sources of allometric equations to predict a given variable.

LIST OF FIGURES

Figure 11. Total HH-polarized canopy backscatter estimated by MIMICS for a bigtooth aspen stand at X, C and L-bands as a function of tree height, diameter, stem density and leaf area index (LAI).

Figure 12. Total VV-polarized canopy backscatter estimated by MIMICS for a bigtooth aspen stand at X, C and L-bands as a function of tree height, diameter, stem density and leaf area index.

88-21826R1

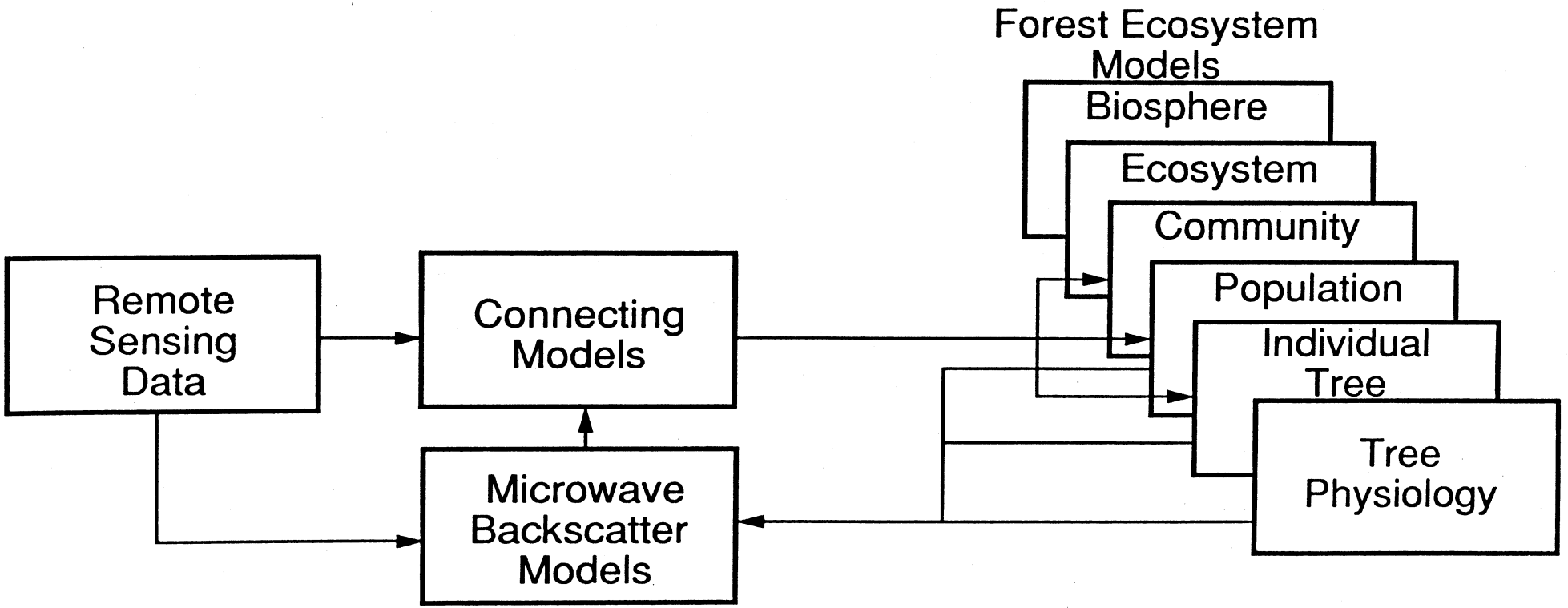

Figure 3

88-1172

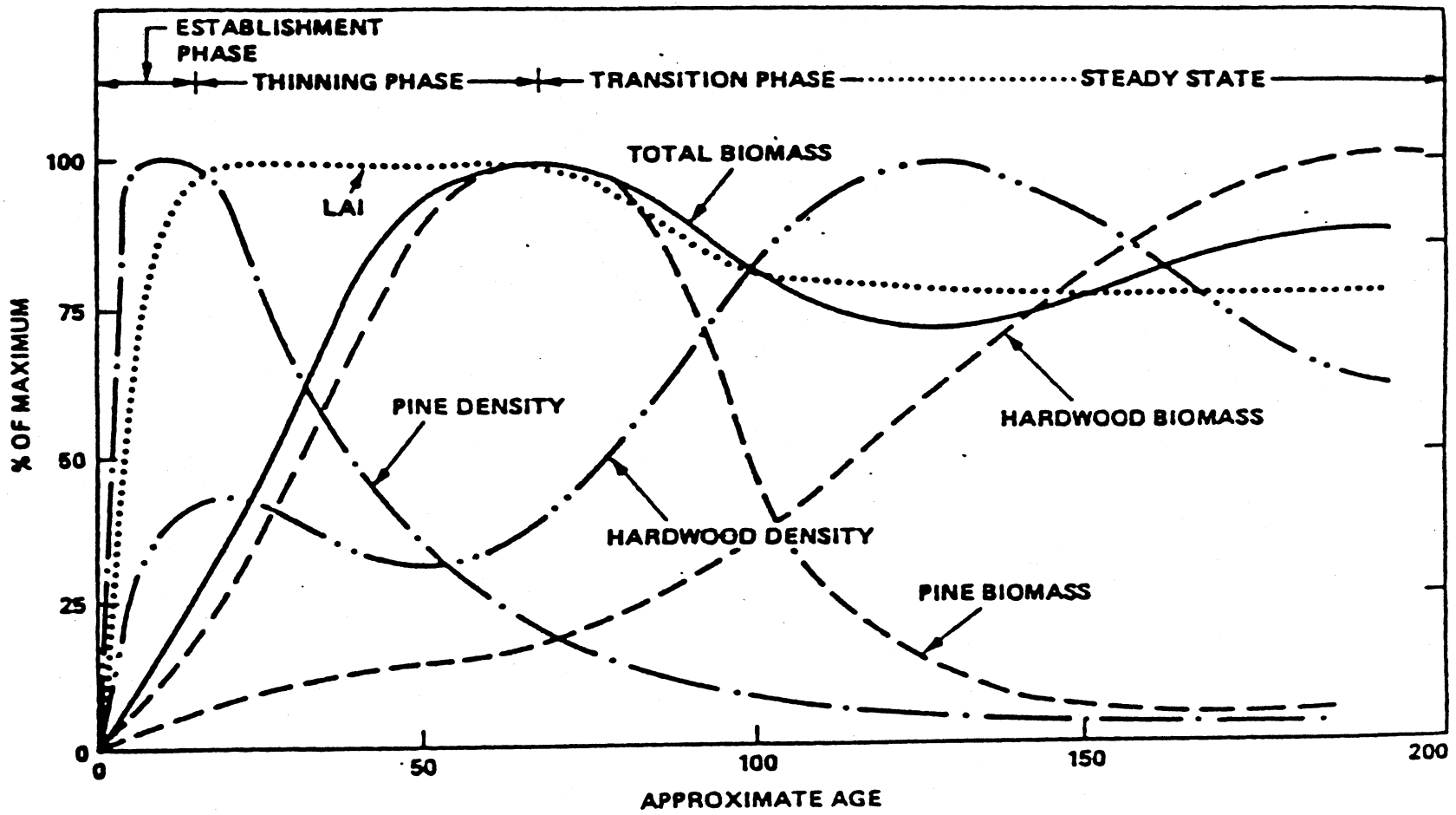

Figure 2

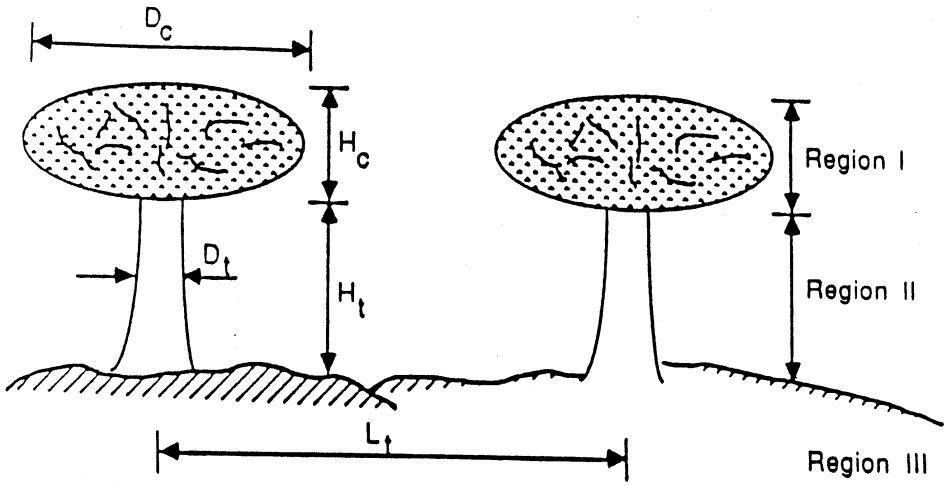

GEOMETRICAL PARAMETERS

I. Crown Region: H_c, foliage height
D_c, foliage diameter
Branches and Needles: $f_c(l,d,\theta,\phi)$; cylinder PDF
l = cyl length, d = cyl diameter,
(θ,ϕ) = cyl orientation
Leaves: $f_d(t,d,\theta,\phi)$; disc PDF
t = disc thickness, d = disc diameter,
(θ,ϕ) = disc orientation

II. Trunk Region: H_t, trunk height
D_t, trunk diameter
R_t, trunk surface roughness
L_t, spacing between trunks

III. Ground Region: S, surface rms height
l_s, surface correlation length

DIELECTRIC PARAMETERS

ε of leaves
ε of branches
ε of trunks
ε of ground

Figure 3

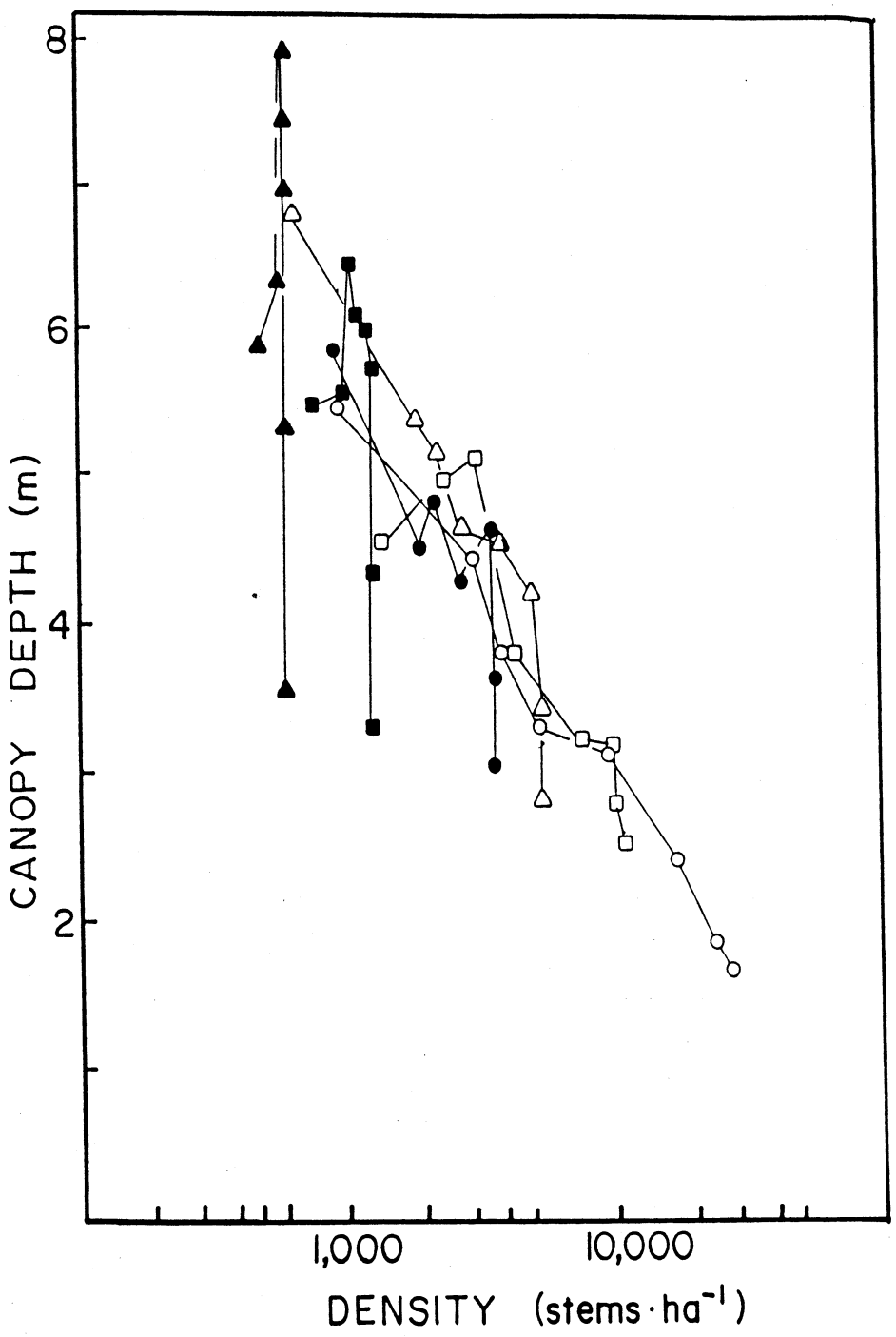

Figure 4

88-11770

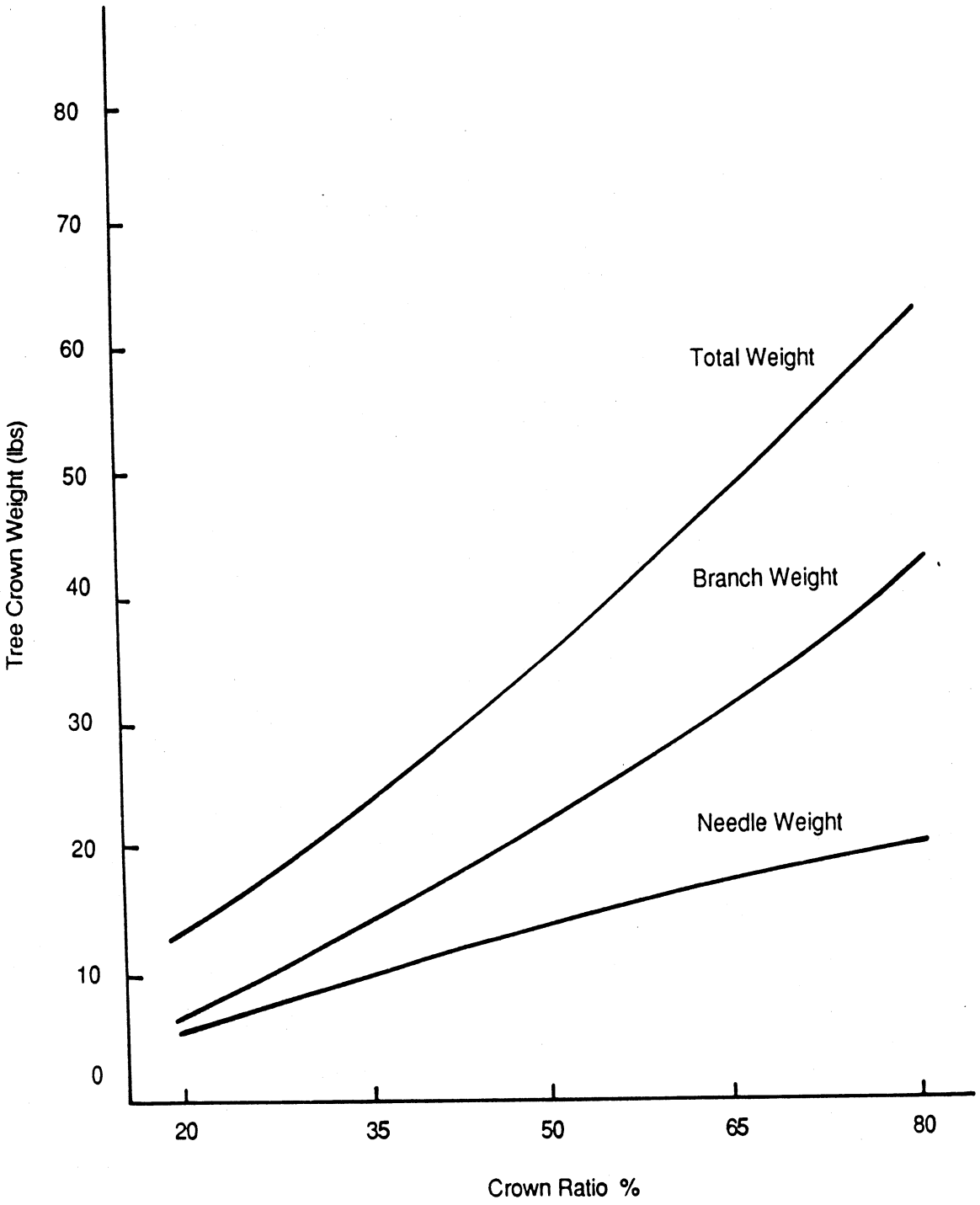

Figure 5

88-1171

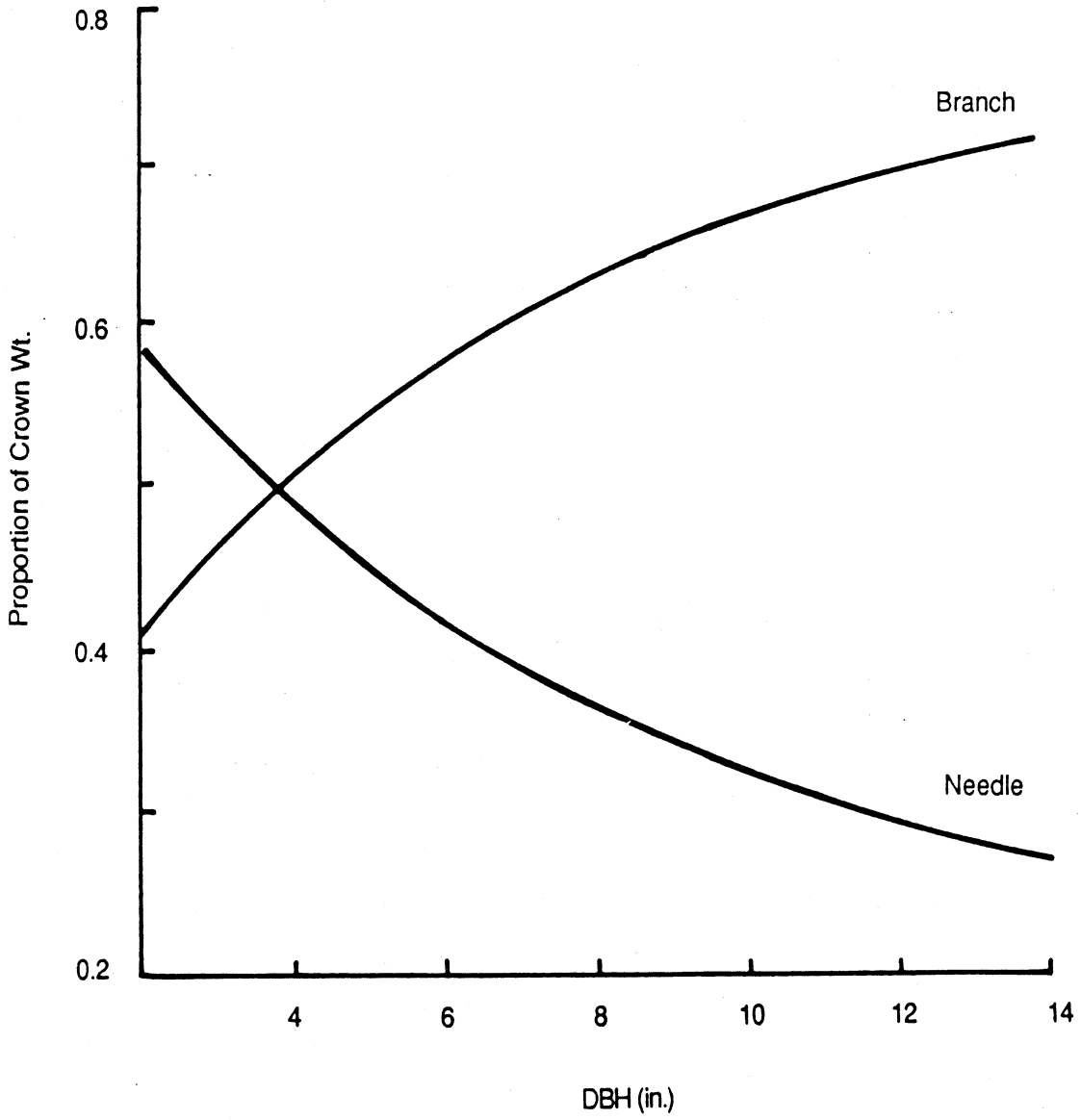

Figure 6

88-1177

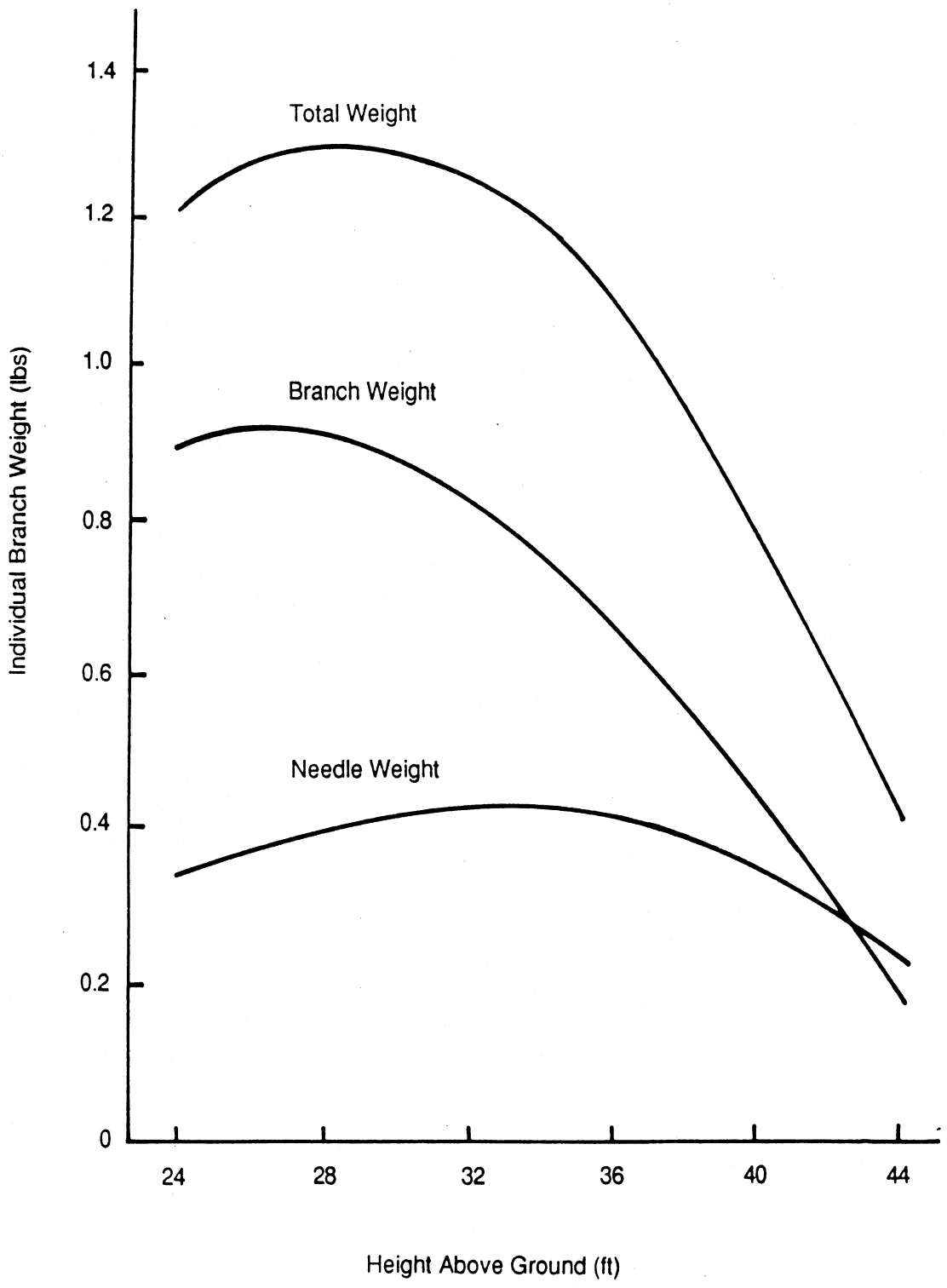

Figure 7

88-11074

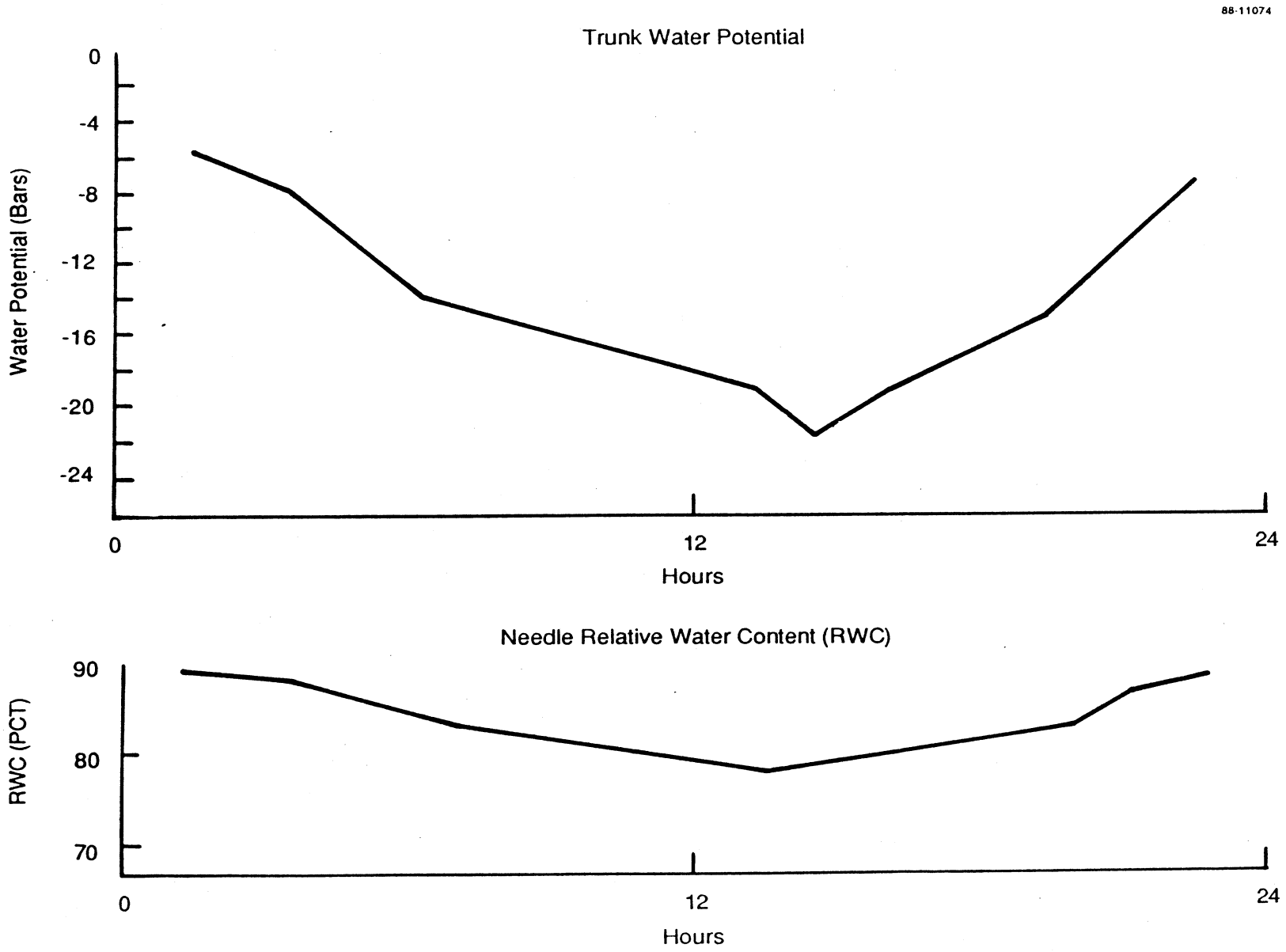

Fig 8

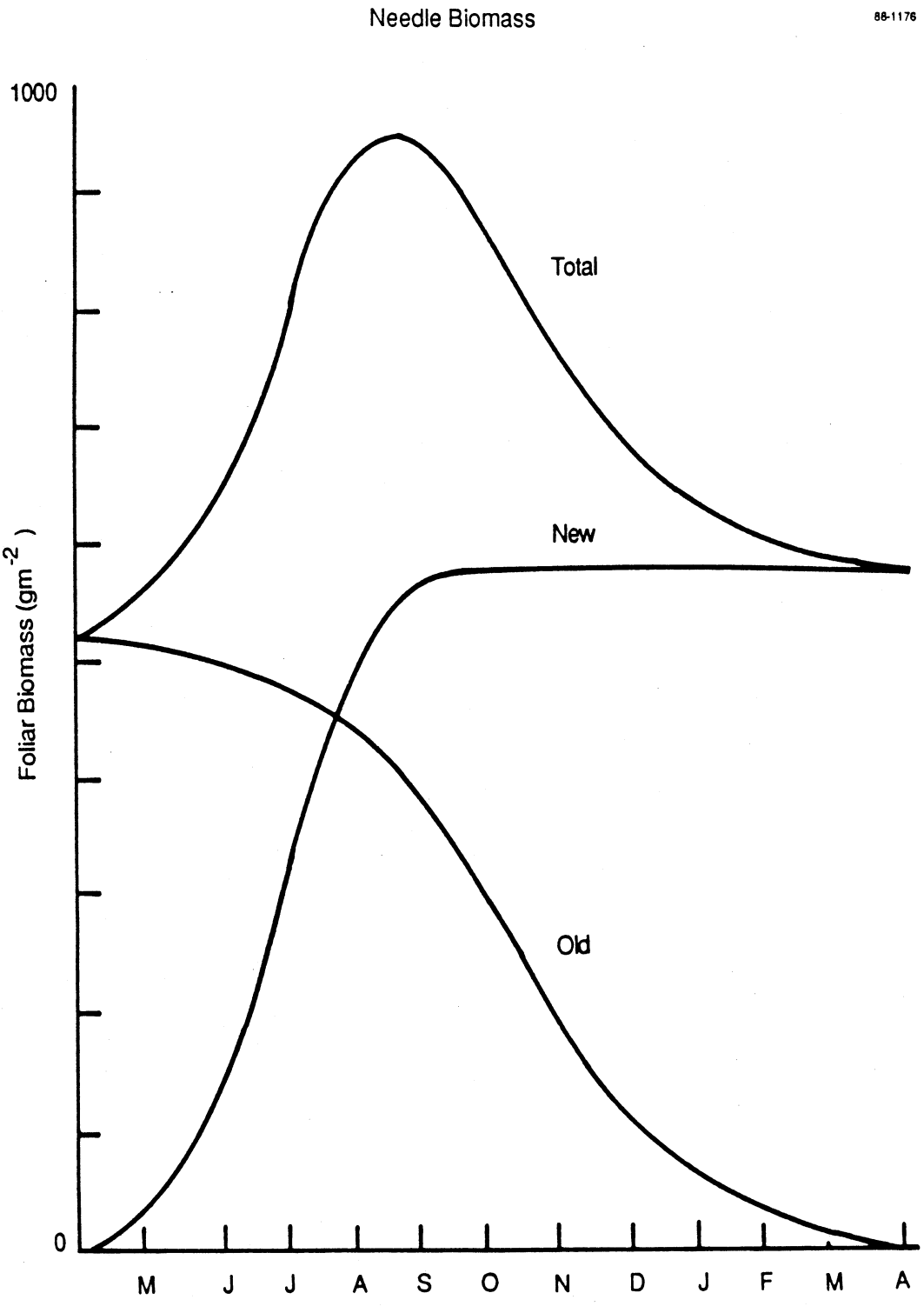
Needle Biomass
86-1176
1000
0
Foliar Biomass (gm-2)
Total
New
Old
M
J
J
A
S
O
N
D
J
F
M
A

Figure 9

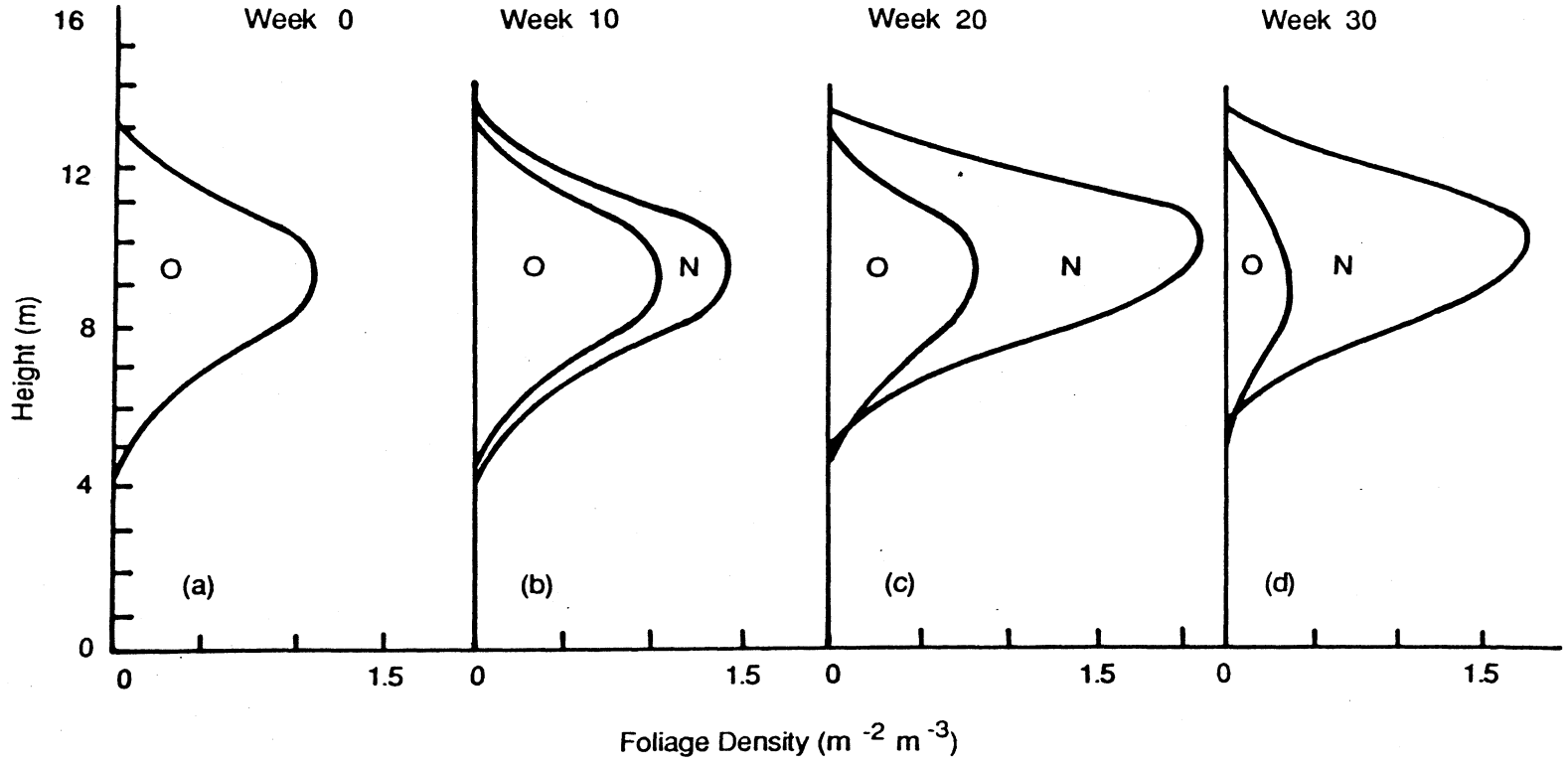

88-111755

Figure 10

TOTAL CANOPY BACKSCATTER
HH – Polarization

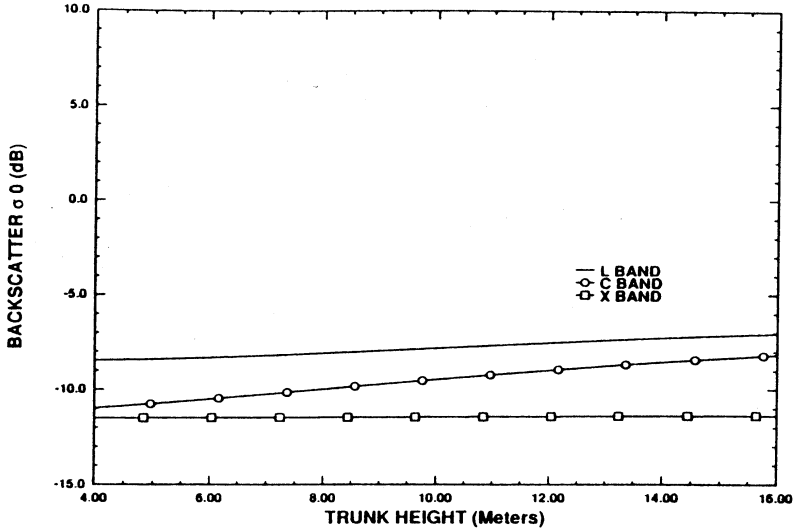

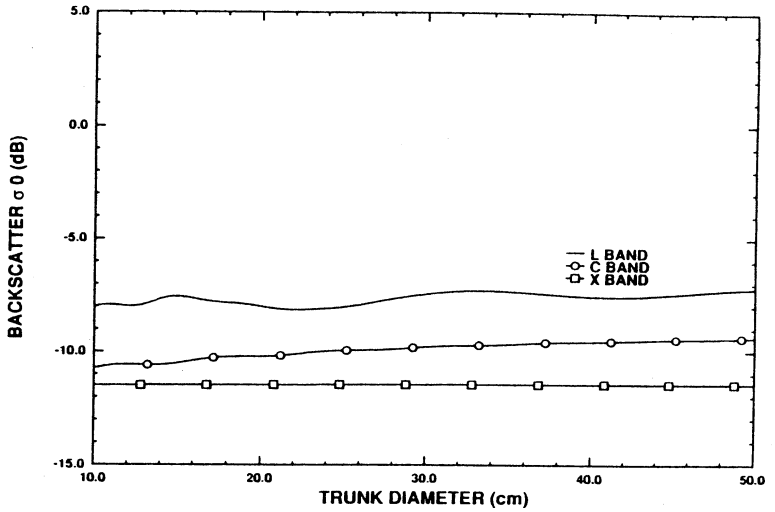

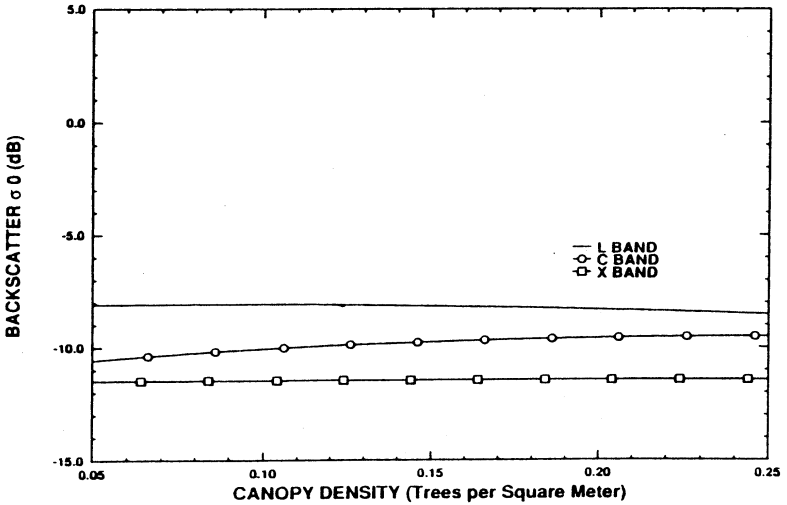

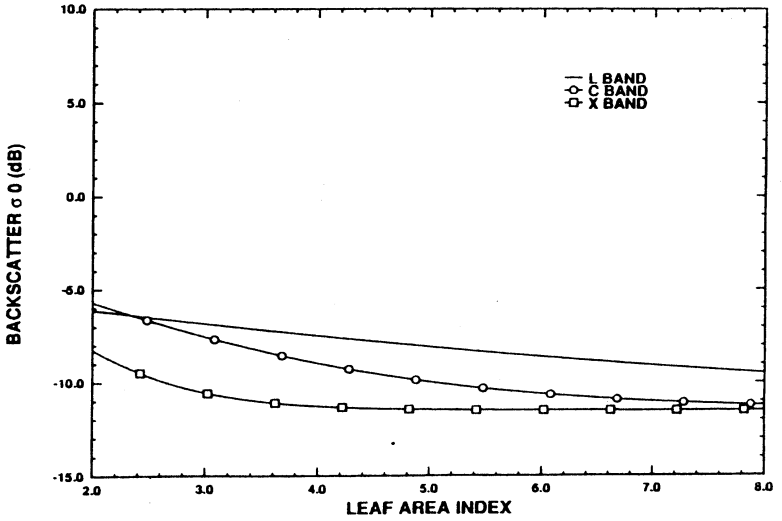

11 May 91

TOTAL CANOPY BACKSCATTER
VV – Polarization

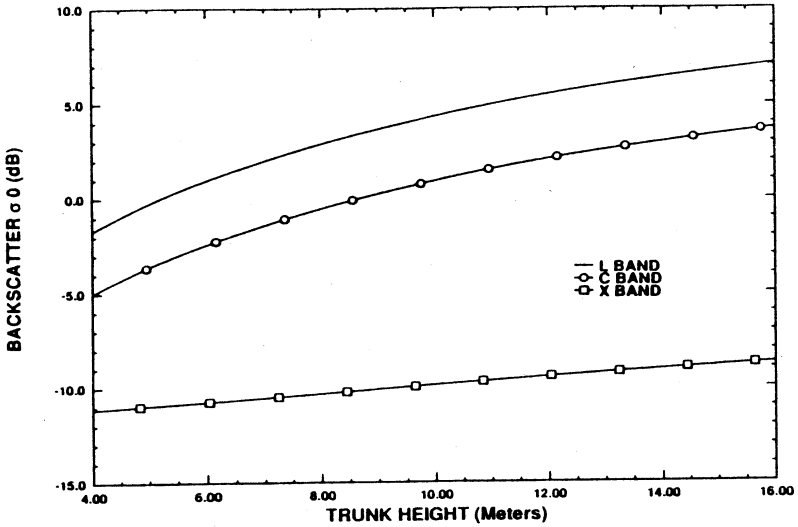

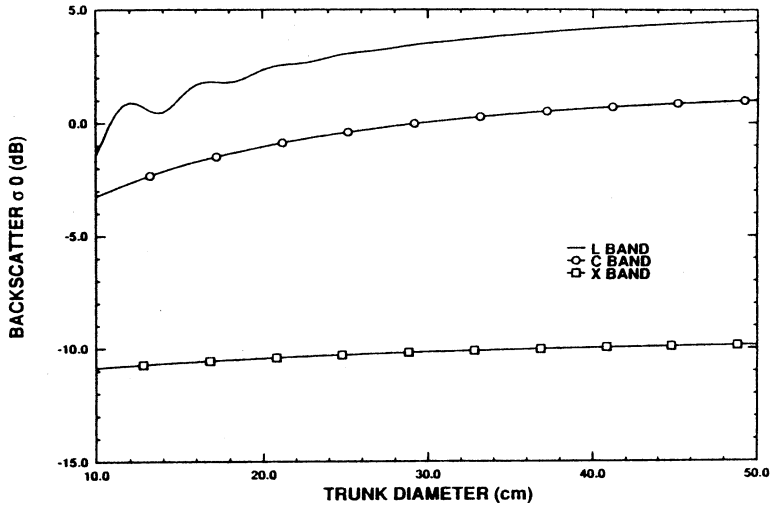

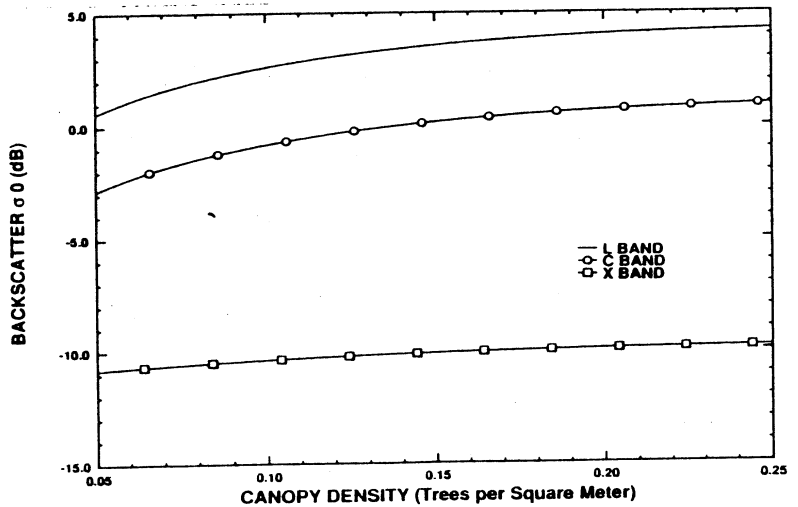

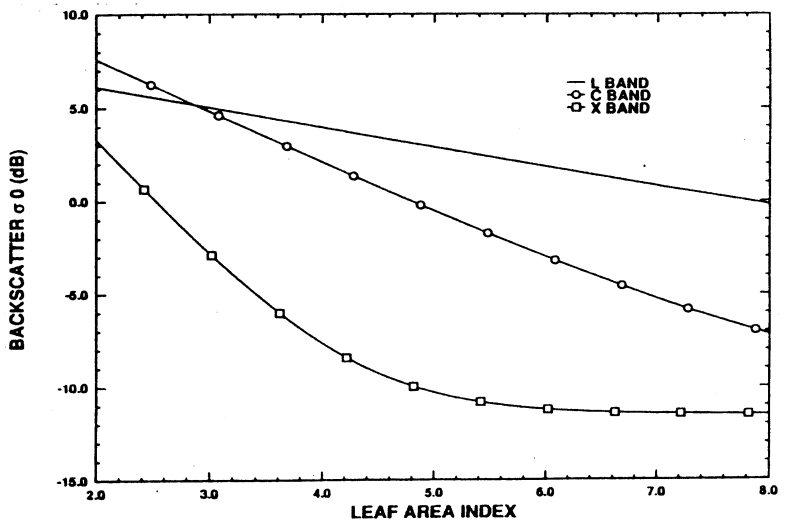

Figure 12

6.0 George Washington University Progress Report

A progress report has not been forthcoming from George Washington University.